

Electrohydrodynamic Atomization in the Simple-Jet Mode

Out-scaling and Application

Proefschrift

Ter verkrijging van de graad van doctor
aan de Technische Universiteit Delft
op gezag van de Rector Magnificus,
prof. ir. K. C. A. M. Luyben,
voorzitter van het College voor Promoties
in het openbaar te verdedigen op
maandag 11 februari 2013 om 15:00 uur.

door

Luewton Lemos Felício AGOSTINHO

Master in Civil Engineering
Universidade Federal do Ceará, Brazil

geboren te
São Luis, Maranhão, Brazil

Dit proefschrift is goedgekeurd door de promotoren:

Prof. dr. ir. M.C.M. van Loosdrecht

Prof. dr. ir. J. C. M. Marijnissen

Samenstelling Promotiecommissie

Rector Magnificus

Prof. dr. ir. M. C. M. van Loosdrecht

Prof. dr. ir. J. C. M. Marijnissen

Prof. dr. A. Schmidt-Ott

Prof. dr. J. Rossel-Llompart

Prof. dr. M. Kennedy

Dr. ir. S. Metz

Dr. ir. C. U. Yurteri

Technische Universiteit Delft, voorzitter

Technische Universiteit Delft, promotor

University of Florida, promotor

Technische Universiteit Delft

Catalan Ins. Res. Adv. Studies, Spanje

UNESCO - IHE

Wetsus

British American Tobacco, UK

Electrohydrodynamic Atomization in the Simple-Jet Mode. Out-scaling and Application

Luewton Lemos Felício Agostinho, 2013

ISBN: 978-90-6464-635-5

Cover design by Luewton L. F. Agostinho and Siebren Brouwer

Illustration by Caio N. A. Agostinho

PhD Thesis Delft University of Technology, Delft, The Netherlands.

Summary

Electrohydrodynamic Atomization, often called electrospraying, is a way to disintegrate a liquid into droplets by exposing it to a strong electric field. Although William Gilbert has reported about the deformation of a liquid meniscus under the influence of an electric field already more than four centuries ago, the interest about electrostatic spraying of a liquid increased just a few decades from now.

Among other advantages these systems can create droplets much smaller than the nozzle diameter with a narrow size distribution. The droplets are also electrically charged and can be manipulated to collide with specific surfaces (electrostatic coating) or with oppositely charged particles (bipolar coagulation).

For a given liquid and setup, different combinations of the electric potential and flow rate can create different spraying modes. The most studied mode is the cone-jet mode due to its capability to produce droplets smaller than the nozzle diameter with a narrow size distribution. The characteristics and particularities of the different modes have been extensively studied and can be found in the literature.

In this thesis we have explored another mode, the simple-jet mode. Compared to the cone-jet mode the simple-jet mode is much less explored. A possible reason for that is the fact that the droplet size in the latter is many times bigger than in the former mode for the same nozzle diameter. Nevertheless, because this mode operates at flow rates much higher than the cone-jet mode it is an interesting option for atomization methods which require high throughputs, e.g. water treatment and agricultural processes.

We have studied the characteristics of this mode to present its operational window and how the application of an electric field changes the droplet size and influences the droplets dispersion.

Additionally we designed a multinozzle device for electrospraying in the simple-jet mode. We show that the device proposed can operate in this mode and that the characteristics of each individual nozzle are similar regarding flow per

nozzle and produced droplet diameter. An insulation layer was applied between the nozzle tip and the counter electrode to allow its operation under high humidity levels without current leakages. The proposed configuration works for the simple-jet mode (the mode which presents the highest flow rate per nozzle in EHDA), therefore it offers very high throughput with a low number of nozzles per unit area.

By coupling the device to a single step evaporator we have shown that the application of an electric potential increase the evaporation of the electro sprayed droplets inside a closed chamber by 40%.

Lastly, we showed that positive electro sprays in the intermittent cone-jet mode can produce negatively charged droplets and explained their origin.

The presented research evidences the necessity of exploring other electrohydrodynamic atomization modes (besides the cone-jet mode) and shows that the simple-jet mode might be a good option for systems which require a relatively high throughput. It also demonstrates that electrohydrodynamic atomization might be a good atomization method for systems like thermal desalination and other distillation processes.

Samenvatting

Electrohydrodynamic Atomization, ook wel *electrospraying* genoemd, is een methode om vloeistof te vernevelen door blootstelling aan een sterk elektrisch veld. Hoewel *William Gilbert* meer dan vier eeuwen geleden heeft gerapporteerd over de vervorming van een vloeistof meniscus onder invloed van een elektrisch veld, is het onderwerp in de afgelopen tientallen jaren meer in de belangstelling gekomen.

Naast andere voordelen kunnen deze systemen druppels creëren die veel kleiner zijn dan de diameter van de gebruikte spuitmond en die een nauwe grootteverdeling hebben. De druppels zijn ook elektrisch geladen en kunnen gemanipuleerd worden om te botsen met specifieke oppervlakken (elektrostatische coatingen) of met tegengestelde geladen deeltjes (bipolaire coagulatie).

Voor een bepaalde vloeistof en opstelling creëren verschillende combinaties van de elektrische potentiaal en debiet verschillende *spray modes*. The meest bestudeerde mode is de *cone-jet mode* vanwege zijn vermogen om druppels te produceren die kleiner zijn dan de diameter van de spuitmond en met een nauwe grootteverdeling. De karakteristieken en bijzonderheden van de verschillende *modes* zijn uitgebreid bestudeerd en kunnen in de literatuur gevonden worden.

In dit proefschrift hebben we een andere *mode* onderzocht, de *simple-jet mode*. Vergeleken bij de *cone-jet mode* wordt de *simple-jet mode* veel minder onderzocht. Een mogelijke reden daarvoor is het feit dat de druppelgrootte voor dezelfde spuitmond diameter in de laatstgenoemde vele malen groter is dan in de eerstgenoemde. Desalniettemin, omdat deze *mode* bij hoge debieten werkt is het een interessante optie voor atomisatie methoden die hoge doorvoer nodig hebben, bijvoorbeeld waterbehandeling en landbouwprocessen.

We hebben de karakteristieken van deze *mode* bestudeerd om de

operationele grenzen te laten zien en hoe de toepassing van een elektrisch veld de druppelgrootte verandert en de dispersie van druppels beïnvloedt.

Daarnaast hebben we een *multinozzle* apparaat ontworpen voor *electrospraying* in de *simple-jet mode*. We laten zien dat het voorgestelde apparaat in deze *mode* kan werken en dat de karakteristieken van elke individuele spuitmond gelijk zijn wat betreft de stroom per spuitmond en geproduceerde druppeldiameter. Een isolatielaag werd toegepast tussen het uiteinde van de spuitmond en de tegen elektrode om het te laten werken onder hoge luchtvochtigheid zonder lekkages van stroom. De voorgestelde configuratie werkt met de *mode* die het hoogste debiet per spuitmond in EHDA laat zien en daarom biedt de erg hoge doorvoer bij een klein aantal spuitmonden per oppervlakte.

Door het apparaat te koppelen aan een enkeltraps verdamper hebben we laten zien dat de toepassing van een elektrisch potentiaal de verdamping van *electrosprayed* druppels in een gesloten kamer met 40% kan vergroten.

Tenslotte toonden we aan dat positieve electrosprays in de *intermittent cone-jet mode* negatief geladen druppels kunnen produceren en legden we hun oorsprong uit.

Het gepresenteerde onderzoek bewijst de noodzaak van het bestuderen van andere *electrohydrodynamic atomization modes* dan het *cone-jet mode* en laat zien dat de *simple-jet mode* een goede optie zou kunnen zijn voor systemen die een relatief hoge doorvoer nodig hebben. Het laat ook zien dat *electrohydrodynamic atomization* een goede atomisatie methode zou kunnen zijn voor systemen als thermische ontzouting en andere destillatieprocessen.

Table of Contents

<i>Summary</i>	3
<i>Samenvatting</i>	5
<i>List of Figures</i>	11
<i>List of Tables</i>	17
<i>Desalination</i>	21
1. Water.....	22
2. Desalination, a historical overview.....	22
3. Desalination Technologies.....	25
Reverse Osmosis (RO).....	26
Multi Effect Distillation (MED).....	26
Multi Stage Flash Distillation (MSF).....	27
Membrane Distillation (MD).....	28
4. Performance Indices.....	28
5. Energy Consumption	31
6. Environmental Impacts.....	33
7. References	35
<i>Electrohydrodynamic Atomization</i>	39
1. Liquid Atomization.....	40
2. Atomization Mechanisms	42
3. Electrohydrodynamic Atomization	43
4. Electrospraying Modes.....	43
5. References	47
<i>The simple-jet mode</i>	51
1. Introduction.....	52
2. Phenomenology	53

3. Materials and Methods	56
3.1 Materials	56
3.2 Nondimensional numbers.....	58
3.3 Experimental method	61
4. Results and Discussion	61
4.1 The operational window of the simple-jet mode	61
4.2 The influence of liquid electric conductivity on the spray diagram	64
4.3 Jet and droplets characteristics	66
5. Conclusions	71
6. References	72
Appendix 3A	75
Nozzle/ringup, nozzle/ringdown or nozzle/plate?	75
<i>Monodisperse sprays</i>	81
1. Introduction.....	82
2. Materials and Method.....	83
3. Results and Discussion	85
4. Conclusions	90
5. References	91
Appendix 4A	93
Droplets position and velocity.....	93
<i>Process out-scaling</i>	99
1. Introduction.....	100
2. Materials and Method.....	102
3. Results and Discussions.....	104
3.1 Breakup length and droplet size and size distribution.....	104
3.2 – Droplet dispersion.....	107
3.3 – Effect of the insulation layer	108
4. Conclusions	110
6. References	111
<i>Single-effect evaporator</i>	113

1. Introduction.....	114
2. Experimental method.....	116
3. Results and discussion.....	119
4. Conclusions	125
6. References	126
<i>Bouncing droplets and clouds.....</i>	<i>129</i>
1. Introduction.....	130
2. Experimental	133
2.1 Electrospray configuration	133
2.2 Optical system.....	134
3. Results and Discussion	135
3.1 Electrospray characteristics, droplet charge and velocity.....	135
3.2 Droplet charge calculation	140
3.3 Droplet charge and trajectory.....	141
3.4 Droplet interaction with the liquid meniscus	143
3.5 Comments on each category.....	147
4. Conclusions	153
7. References	155
Appendix 7A.....	157
Calculation of a single droplet charge	157
<i>General conclusions and outlook.....</i>	<i>163</i>
<i>Appendix 8.....</i>	<i>167</i>
<i>Nozzles.....</i>	<i>167</i>
<i>Acknowledgments.....</i>	<i>171</i>
<i>Curriculum Vitae.....</i>	<i>173</i>
<i>List of Publications and Prize</i>	<i>175</i>

List of Figures

Figure 1.1 – Della Porta distillation apparatus published in <i>Maggiae Naturallis</i> (1558).	23
Figure 1.2 - Classification of different desalination technologies.	25
Figure 2.1 – Droplet formation mechanisms in the dripping regime (a), dripping faucet regime (b) and in the jetting regime (c).	41
Figure 2.2 – Electrospray modes as a function of the applied potential and flow rate for a given nozzle/counter electrode geometry and their relation with the droplet formation regimes. Adapted from the diagram presented by Geerse ²⁶	45
Figure 3.1 - Different hydrodynamic and electrohydrodynamic droplet formation mechanisms: (a) Dripping regime, uncharged jet; (b) Transition regime, uncharged jet; (c) Jetting regime, uncharged jet; (d) Simple-jet mode with varicose breakup, charged jet.; e) Simple-jet mode with whipping breakup, charged jet.....	54
Figure 3.2 – Effect of the electric field on the charged droplets in the simple-jet mode (spray envelope). For all the pictures the liquid used is deionized water pumped through the nozzle at 420 mL·h ⁻¹ . The indicated potentials were applied on the ring (not shown in the picture) with the nozzle grounded.....	55
Figure 3.3 – Electrospray and optical system scheme.	57
Figure 3.4 - Representation of the nozzle-ring set-up and images of the spray. 3.4a - Close view of the jet breakup with water (L1) at -6kV and 360mL·h ⁻¹ and representation of the nozzle-ring setup with the defined axis and some variables. 3.4b - Snapshot of the jet with the dispersed droplets and a small part of the metallic nozzle. 3.4c - Superimposed image showing the spray envelope, the break-up length (h_b) and the envelope angle (θ).....	58
Figure 3.5 - Diagram representing the operational window of the simple-jet mode in relation to the electric Bond number (B) and the liquid Weber number (We) for deionized water. The control parameters related to B (applied potential) and We (flow) are represented on the right and upper axis, respectively.....	62

Figure 3.6 - Sequences according to the sets a), b) and c) defined in Fig. 3.5...	63
Figure 3.7 - Whipping line and dispersion line from linear fits of experiments with water and sodium chloride aqueous solutions with different concentrations (17, 20, 35 and 70 g·L ⁻¹) for different values of <i>We</i> and <i>B</i> . The insertion shows the electric conductivity of the solutions for the different concentrations respectively.....	65
Figure 3.8 - Normalized electric current against <i>B</i> for three different flows (<i>We</i> = 5.3, <i>We</i> = 6.3, <i>We</i> = 13.4) for NaCl solution (35 g·L ⁻¹). The dotted lines connecting the symbols are to guide the eyes.....	66
Figure 3.9 (a and b) - Jet nondimensional radius (<i>r_j</i> (2a ⁻¹)) against the electric Bond number at <i>z a</i> ⁻¹ = 9.4 for different values of the liquid Weber number and electric Bond number (3.9a) and for a constant electric Bond number and different values of <i>We</i> (3.9b) for liquid L2. Each data point represents the average of three or more different measurements with the error bar representing the minimum and maximum measured values.	67
Figures 3.10 (a and b) - Normalized diameter of the primary (3.10a) and satellite (3.10b) droplets generated for different values of the liquid Weber (in figure 3.10b <i>We</i> = 11.4) number and electric Bond number for deionized water and a solution of water and sodium chloride (35 g·L ⁻¹). Error bars are data standard error.....	68
Figure 3.11: Superposed images of the droplets for <i>We</i> = 5.2 and <i>B</i> = 0 (a), <i>B</i> = 280 (b) and <i>B</i> = 500 (c) and for <i>B</i> = 500 with <i>We</i> = 5.2 (d), <i>We</i> = 7.5 (e) and <i>We</i> = 10.3 (f). Both experiments were performed with deionized water (L1).	69
Figure 3A.1 - 2D model geometries of the studied symmetric configurations. .	76
Figure 3A.2 - Surface plot (electric field) and contour plot (electric potential) plots of the configurations. The color scale applies only to the surface plot.....	77
Figure 3A.3 - Electric potential (a, b and c), axial component of the electric (d, e and f) field and radial component of the electric field (g, h and e) for each configuration. Nozzle/plate plots are figures 3A.3a, 3A.3d and 3A.3g. Nozzle/ringdown are the plots shown in figures 3A.3b, 3A.3e and 3A.3h. Nozzle/ringup are the plots represented in figures 3A.3c, 3A.3f and 3A.3i.....	78
Figure 3A.4 - Radial (3A4.a) and axial (3A4.b) component of the electric field for the three configurations 1mm beneath the nozzle tip.	79
Figure 4.1 – Electrospray and optical system scheme.	85

Figure 4.2(a-d) - Particle size distribution of the droplet diameters for deionized water at $We = 3.3$ (4.2a) and 13.4 (4.2b) and NaCl aqueous solution at $We = 3.3$ (4.2c) and $We = 13.4$ (4.2d) for different potentials.....	86
Figure 4.3 - Sprays at different potential and Weber number for Dwater and NaCl.	88
Figure 4.4 - Relative Standard Deviation (RSD) of the analyzed distributions for NaCl _{aq} (4.4a) and Dwater (4.4b) for different values of We and Φ	89
Figure 4A.1 - Axis directions and origin.....	93
Figure 4A.2 – Droplets Ferrets diameters in a single nozzle electrospray.....	95
Figure 4A.3 - Droplets velocities.	96
Figure 4A.4 - Droplets Reynolds numbers.....	97
Figure 5.1 - Multinozzle configuration. (1) Gas column, (2) liquid column, (3) metallic nozzles, (4) counter electrodes (rings), (5) protective layer (insulation), (6) multinozzle array, (7) 3D view of the glass heating jacket and the multinozzle body without the insulative layer. The break-up length is represented by L and the distance between two nozzles (18mm) by B.	103
Figure 5.2 – Breakup length (L) in each nozzle at different flow rates ($300 \text{ mL}\cdot\text{h}^{-1}\cdot\text{nozzle}^{-1}$, $360 \text{ mL}\cdot\text{h}^{-1}\cdot\text{nozzle}^{-1}$ and $420 \text{ mL}\cdot\text{h}^{-1}\cdot\text{nozzle}^{-1}$) for 0 (5.2a) and 3 kV (5.2b). Error bars represent the standard error of each measurement.	105
Figure 5.3 – Droplet average diameter in each nozzle at different flow rates ($300 \text{ mL}\cdot\text{h}^{-1}\cdot\text{nozzle}^{-1}$, $360 \text{ mL}\cdot\text{h}^{-1}\cdot\text{nozzle}^{-1}$ and $420 \text{ mL}\cdot\text{h}^{-1}\cdot\text{nozzle}^{-1}$) for 0 (5.3a) and 3 kV (5.3b). Error bars represent the standard error of each measurement.	106
Figure 5.4 – Relative standard deviation of the generated droplets in each nozzle at different flow rates ($300 \text{ mL}\cdot\text{h}^{-1}\cdot\text{nozzle}^{-1}$, $360 \text{ mL}\cdot\text{h}^{-1}\cdot\text{nozzle}^{-1}$ and $420 \text{ mL}\cdot\text{h}^{-1}\cdot\text{nozzle}^{-1}$) for 0 (5.4a) and 3 kV (5.4b). Error bars are calculated error based on the distributions.	106
Figure 5.5 – Overview of the multinozzle spray. The flow was stabilized at $300 \text{ mL}\cdot\text{h}^{-1}\cdot\text{nozzle}^{-1}$ and the potential was increased from 0 (5.5a) to 7.5 kV (5.5f) in steps of 1.5 kV.....	108
Figure 5.6 – Plot of electric current and liquid influent temperature against time.	109

Figure 6.1 - Complete multi-nozzle EHD atomizer coupled with single-effect evaporator with chamber A and B (not in scale). Thermal baths for pre-heating oil and for the jacket are not shown in the diagram..... 116

Figure 6.2 - Schematic diagram of chamber A (not in scale). The chamber is made out of glass and polypropylene (PP). The specified parts are: Gas column (1), salt solution (2), nozzles (3), cooper rings (4), insulation layer (5). The nozzles and rings are organized in a circular pattern (6)³². 117

Figure 6.3 - Online measurements of the brine conductivity (solid line) and inlet conductivity (small dashed line) for different potentials (long dashed line) and two different flow rates. In this experiments T1 = 80°C, T2 = 25°C and dry air counter flow 75 L·min⁻¹ 120

Figure 6.4 - Relative evaporation at different potentials (0 to 4kV) for different flow rates (240, 300, 360 and 420 mL·h⁻¹·nozzle⁻¹). Spray temperature (T1) was fixed at ~80°C, dry air was inject in a counter flow at 45 L·min⁻¹ and reactor jacket temperature was kept at 25°C (T2). Each data point represents the average of the two measurements with the error bar representing the minimum and maximum measured values. 121

Figure 6.5 – Influence of different flow rates of the injected dry air with the liquid pre-heated to 80°C (6.5a) and influence of the different spray initial temperature (6.5b) on the spray relative evaporation. Both experiments were done for 360 mL·h⁻¹·nozzle⁻¹. The experiments presented in figure 5b were done for a constant air flow rate of 75 L·min⁻¹. Each data point represents the average of the two measurements with the error bar representing the minimum and maximum measured values..... 122

Figure 7.1 - Electrospray and optical system scheme. 134

Figure 7.2 - Category C1 (complete coalescence) – a droplet returns to the cone after being formed from a liquid ligament. The diameter of the returning droplet is ~ 80 μm, time frame between images is ~45 μs, applied potential is - 5.67 kV on the counter electrode and used flow rate is 1 mL·h⁻¹. 135

Figure 7.3a (left) and 7.3b (right) - Magnification of frames 15 and 16 of Fig. 7.2 showing the polarisation of the aqueous ligament which subsequently forms differently charged droplets. 138

Figure 7.4 - Cone tip position, droplet axial coordinate against droplet velocity from frame 18 to 29 and coordinate system (returning droplet represented in Fig. 7.2).....	139
Figure 7.5(a, b, c, and d) - Droplet velocities and axial position calculated from a sequence of frames and theoretically calculated correspondences for the same sequences. Fig. 7.5a and 7.5b show the best fit found for a theoretical droplet charged with ~ 0.46 pC; Fig. 7.5c and 7.5d show the best fit found for a theoretical droplet charged with ~ 0.12 pC. The used potential for both situations was 6 kV with $1 \text{ mL}\cdot\text{h}^{-1}$ and 2 cm nozzle to plate distance.	141
Figure 7.6 - Estimated droplet charges and respective percentage to Rayleigh Limit for different diameters.	142
Figure 7.7 - Estimated droplet surface charge density for different diameters.	143
Figure 7.8 - Bouncing with “partial coalescence” or C2 – a droplet collides with the meniscus with mass exchange. The droplet diameter before collision with the meniscus is $\sim 70 \mu\text{m}$ and after is $\sim 40 \mu\text{m}$, time frame between images is $\sim 50\mu\text{s}$, applied potential is 5.0 kV on the nozzle and the flow rate is $1 \text{ mL}\cdot\text{h}^{-1}$.	144
Figure 7.9 - Non-coalescent bouncing. Nozzle to plate configuration with 6 kV applied on the nozzle. Plate grounded and placed 4 cm below the nozzle. Dashed lines are arbitrarily placed to guide the eyes. Droplet’s diameter is $\sim 30 \mu\text{m}$ and the time frame between images is $40 \mu\text{s}$	145
Figure 7.10 - Axial coordinate of the uppermost formed droplet represented in Fig. 7.9 against frame number. The chosen origin for the coordinate system is the same as in Fig. 7.4.....	146
Figure 7.11 - Six examples of returning droplets assuming asymmetric tear-shapes immediately before contacting the meniscus (this is not a sequence).	147
Figure 7.12 (a, b, c, d) - 7.12a and 7.12b - Droplets velocity against time in categories C1 and C2 for sprays of $0.5 \text{ mL}\cdot\text{h}^{-1}$ and $2 \text{ mL}\cdot\text{h}^{-1}$ respectively. Figures 7.12c and 7.12d, droplets momentum against time in categories C1 and C2 for the same sprays. Both sequences were recorded with 40.000 fps, which represents a time frame of $25 \mu\text{s}$ between two images. The flow and potential applied on the sprays represented in figures 7.12a and 7.12c are respectively $0.5 \text{ mL}\cdot\text{h}^{-1}$ and 6 kV and on the sprays in figures 7.12b and 7.12d are $2 \text{ mL}\cdot\text{h}^{-1}$ and 5.5 kV.....	148

Figure 7.13 - Diameters of category C1 and C2 droplets for the sprays analysed in Fig. 7.11	150
Figure 7.14 - Average retention time for droplets of category C1, C2 and C3 for three different flow rates ($0.5 \text{ mL}\cdot\text{h}^{-1}$, $1 \text{ mL}\cdot\text{h}^{-1}$ and $2 \text{ mL}\cdot\text{h}^{-1}$) compared with the average oscillation time of the liquid meniscus.....	152
Figure 7.15 - Electric current against time synchronized with the spray movie. The spray flow was $1\text{mL}\cdot\text{h}^{-1}$ with -5 kV applied on the counter electrode. Time frame between two images is $27 \mu\text{s}$. The meniscus shape is represented by the images of some frames and the respective electric current signal for each frame is presented in the plot.	153
Figure 7A.1 - Axis direction and origin.	157
Figure 8A.1 - Nozzle with heat exchange for evaporation experiments.	167
Figure 8A.2 - Multinozzle design with internal heat exchange.	168
Figure 8A.3 – Multinozzle with heat exchange and insulation layer.	169
Figure 8A.4 – Electrospray inventory.	170

List of Tables

Table 1.1: Recovery ratio (%) of different desalination technologies by different authors.	30
Table 1.2: Energy consumption for different desalination processes.	32
Table 3.1: Viscosity, density, relative permittivity, conductivity and surface tension (liquid-air interface) of the liquids.....	56
Table 3.2: Break up length (h_B) and normalized breakup length (L) for different values of We and B with deionized waster (L1).....	71
Table 4.1: Viscosity, density, relative permittivity, conductivity and surface tension (liquid-air interface) of the liquids.....	84
Table 5.1. Physical properties of the liquid.	102
Table 6.1: Physical properties of NaCl with concentration of 35g/l.....	118

To my family....

Chapter 1

Desalination



Sailors producing fresh water from distillation of sea water
(Alexander of Aphrodisias, AD 200)

1. Water

Water is essential for many different activities and processes. It is used for growing food; for household water uses, including drinking, cooking, and sanitation; as a critical input into industry; for tourism cultural, religious and spiritual purposes; and for its role in sustaining the earth's ecosystems¹. As for its importance many efforts have been put into the production of water at sufficient quality and enough quantity to supply the human needs.

National, regional, and seasonal water scarcities pose severe challenges for governments, international development and environmental communities. But the challenges of growing water scarcity are heightened by the increasing costs of finding new water resources, degradation of soil in irrigated areas, depletion of groundwater, water pollution and degradation of water-related ecosystems and wasteful use of already developed water supplies often encouraged by the subsidies and distorted incentives that influence its use¹.

As a consequence some opportunities for the investigation and implementation of nontraditional technologies, such as desalination, have arisen. This technology is included among the most advisable solutions to solve the growing water scarcity because it uses the biggest source of water on our planet, the oceans. However, it contributes nowadays to only about 0.2 percent of the global water withdrawals, and perhaps one percent of drinking water^{2,3}.

2. Desalination, a historical overview

Still considered as a *nontraditional* process desalination was already mentioned by Aristotle (384-322) in his book *Metrology*^{4,5} as follows:

“...Salt water when it turns into vapour becomes sweet, and the vapour does not form salt water when it condenses again. This I know by experiment...”

In the same book, Aristotle also makes reference to a *membrane* desalination process, when he says:

“...There is more evidence to prove that saltiness [of the sea] is due to the admixture of some substance, besides that which we have adduced. Make a vessel of wax and put it in the sea, fastening its mouth in such a way as to prevent any water getting in. Then the water that percolates through the wax sides of the vessel is sweet, the earthy stuff, the admixture of which makes the water salt, being separated off as it were by a filter...”

Yet, until the Renaissance, there were no functional methods about desalination processes published or patented ⁵. The first book which mentions desalination in details is probably *Magiae Naturallis* (1558) written by Giovanni Batista Della Porta (1535-1615)⁶. In the first edition of his book he mentions three desalination systems ⁶, in the second edition, issued in 1589, there is a complete chapter dedicated to distillation wherein Della Porta mentions seven different desalination methods ⁷ and presents different sketches which an example is shown in figure 1.1.



Figure 1.1 – Della Porta distillation apparatus published in *Magiae Naturallis* (1558).

The understanding about the process developed and the first American patent claiming solar distillation was granted to Wheeler and Evans in 1870 ⁸.

Two years later, in 1872, the first large scale solar distillation plant was built in Las Salinas, Chile by the Swedish engineer Carlos Wilson with a production capacity of 22.3 m³ of fresh water per day⁹. After that a further boost occurred during the Second Great War, to provide fresh water to the troops in North Africa, Pacific Ocean Islands and other isolated places^{5,10}.

After this the investments on the technology progressively increased causing the United States to approve the implementation of an Office of Saline Water (OSW)⁵ which supported the installation of different thermal desalination plants in the country¹¹⁻¹⁴. This triggered the implementation of other thermal desalination plants in different parts of the world, e.g. Caribbean Islands¹⁵, Coober-Pedy, Australia¹⁶ and USSR^{17,18}.

Thermal desalination has dominated the market till the introduction of polyamide membranes in the 1980s³. Up to this time the application of membrane system to desalinate water was possible but very inefficient and restricted to low salinity water sources, e.g. brackish. The newly developed membranes enabled the process to happen at lower pressure and could reduce seawater salinity to potable standards in a single-pass process³; Seawater Reverse Osmosis (SWRO) was then introduced to the market.

The subsequent advances in material science made membrane technologies more competitive and an interesting option for desalination. Nowadays the process accounts for more than 50% of the global desalination capacity¹⁹. Thermal desalination is, however, still a better option when thermal energy is available, e.g. next to power plants and oil refineries, due to its robustness and large production rates. Additionally, a more modern trend are the hybrid processes, i.e. thermal-membrane based desalination, like the recently developed Membrane Distillation systems²⁰⁻²⁴.

The global desalination capacity in 2006 was estimated to be 44.1 million m³ per day (IDA 2008) with an average growth of 12% per year over the past five years. The projected capacity for 2010 was 64 million m³ per day and 98 million m³ per day for 2015²⁵. As the global capacity increases concerns are addressed about environmental impacts, energy demand, usage of chemical agents and possible treatment for the brine stream.

3. Desalination Technologies

Desalination describes any process designed to remove salts from water. Different processes can be devised for that purpose but all of them are based on the principle that such separation works against the entropy of the system, thus it requires some kind of energy. The first desalination units were based on evaporation, e.g. thermal energy; nowadays the separation can also be achieved by using mechanical, electrical and chemical energy. Moreover the processes can also be divided by the used separation mechanism, i.e. membrane and non-membrane based processes, and by the separation priority, i.e. water from salts and salt from water. Figure 1.2 shows some recent technologies and their classification.

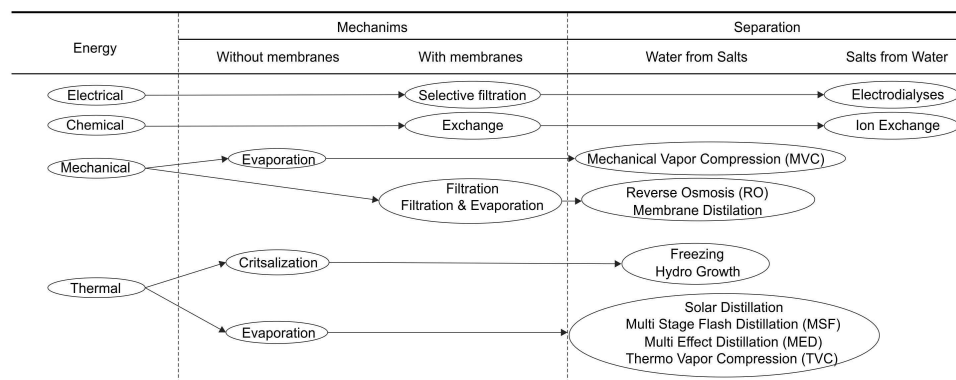


Figure 1.2 - Classification of different desalination technologies.

The process converts the influent into two streams: a fresh water product stream containing a low concentration of dissolved salts and a concentrated effluent stream called “brine”.

Three technologies are responsible nowadays for 93% of the worldwide capacity; Reverse Osmosis (RO), Multistage Flash Distillation (MSF) and Multi Effect Distillation (MED)². After the implementation of membrane based processes the economical feasibility of thermal processes has been re-evaluated and some optimization studies arose, e.g. integration with renewable energy sources^{3, 5, 16, 24}.

The most mentioned bottlenecks of the technology are nowadays the

transportation costs to reach non-costal areas, capital and energy costs and the environmental damages from generated wastes ¹.

The following sections briefly mention the most important desalination technologies.

Reverse Osmosis (RO)

Seawater can be filtrated if the natural osmotic process is reverted. Such reversion requires an energy input into the system. If the pressure on the solution with the highest salt concentration exceeds the natural osmotic pressure, the direction of flow is reversed and water flows from the concentrated solution to the diluted solution. In water desalination, the feed side (concentrated solution) is operated under pressure levels higher than on the permeate side (diluted solution) ²⁶. The technology is the one which has grown fastest over the past 10 years. Modern Sea water reverse osmosis (SWRO) plants have a production capacity per unity of $2 \cdot 10^4 \text{ m}^3 \cdot \text{day}^{-1}$ and an energy consumption ratio of 2.5 – 7 kWh per cubic meter of fresh water produced ²⁷.

Multi Effect Distillation (MED)

Multi Effect Distillation (MED) is a thermal based process. It works basically as an array of thermal distillers, i.e. effects or stages. Each thermal distiller is composed of two elements: the evaporator and the condenser. The evaporator is the element where the thermal energy is transferred from the motive steam towards the feed. The feed is sprayed onto the outer surface of the evaporator tubes in a thin film to increase the contact area promoting evaporation. The produced vapour is forced through a demister into the condenser. Once it gets in contact with the tube stack in the condenser it condenses and both the latent heat and the sensible heat are transferred to preheat the feed. MED takes place in a series of vessels kept at decreasing

pressure/temperature levels. The combination of different effects as an array is a way to increase the efficiency of the process. To avoid scaling on the tube bundle the external temperature is kept below 80°C which keeps the evaporation level in each stage around 10%. The thermal energy stored in the vapour is recovered from one stage to the next. This vapour condenses at the inside walls of the tubes, providing heat to evaporate a portion of the seawater feed to this stage effect. This continues for several stages as long as the temperature drop can still be efficiently used to evaporate the preheated feed. The vapour generated in the last stage condenses in the condenser to preheat the feed. The condensed vapour from the tube bundle (distillate) streams into the distillate reservoir, while non-condensed vapour will be reused in the next tube bundle driven by the pressure gradient. The non-evaporated feed from the first stage (brine) is drained into the second stage. As the brine flows from the first to the second stage (maintained at lower pressure), it flashes off, thereby generating additional vapour. Typically, an MED plant contains 8 to 16 stages. They are generally built in units which can produce $2 \cdot 10^3$ to $3 \cdot 10^4$ $\text{m}^3 \cdot \text{day}^{-1}$.

Multi Stage Flash Distillation (MSF)

In the Multi Stage Flash (MSF) process, seawater is heated in a vessel called the *brine heater*. The heated seawater is pumped into another vessel, i.e. a stage, where the ambient pressure is lowered, causing it to immediately boil (flashing effect). The sudden introduction of the heated water into the chamber causes it to boil rapidly, flashing into steam. Generally, only a small percentage of this water is converted into steam, depending on the pressure maintained in this stage, since the phase shift decreases the liquid's temperature. In this case evaporation will occur from the bulk fluid rather than at a hot heat exchange surface, therefore it reveals fewer scaling problems. The vapour generated by flashing is converted into fresh water by being condensed on the surface of tubes (heat exchangers) that run through each stage. The tubes are cooled by the incoming feed water going to the brine heater. This, in turn, warms up the feed so that the amount of thermal energy needed in the brine heater is reduced. MSF

plants offer the largest potential for fresh water production. They are widely used where extreme seawater conditions are a problem for membrane processes (i.e. Gulf Countries). The process is highly efficient if it can be coupled to sources of waste heat. Moreover, new potential applications of MSF technology have arisen in recent years following several studies on coupling nuclear power plants to thermal desalination. In this kind of plant, the huge amount of waste heat meets the heat demand of an MSF unit, and fresh water can be produced at low costs with excellent robustness and reliability. Typically, an MSF plant contains 15 up to 25 stages. The typical production rate of such plants ranges from about 4,000 to 60,000 m³·day⁻¹.

Membrane Distillation (MD)

Membrane distillation is a non-isothermal membrane process in which the driving force is the partial pressure gradient across a membrane that is porous, not wetted by the process liquids, does not alter the vapour/liquid equilibrium of the involved species, does not permit condensation to occur inside its pores and is maintained in direct contact with the hot feed liquid solution to be treated. A typical MD unit is Memstill[®]. The modules used in this system are a flat plate type. The design capacities of the waste heat-driven units are 80 and 50 m³·day⁻¹. The process expect to decrease desalination costs to below 0.5 US\$.m⁻³ using low grade waste steam or heat at around 87° C as a driving force.

4. Performance Indices

Mostly the performance indices used to compare desalination processes are based on the concentration of the outputs. If considered that the effluents of all processes are composed by a highly concentrated stream (brine) and a less concentrated stream (distillate) its overall mass balance can be represented as

$$\dot{m}_i = \dot{m}_d + \dot{m}_b, \quad (1.1)$$

where \dot{m}_i is the mass flow rate [$\text{kg}\cdot\text{s}^{-1}$] of the influent, \dot{m}_d is the mass flow rate [$\text{kg}\cdot\text{s}^{-1}$] of the distillate and \dot{m}_b is the mass flow rate [$\text{kg}\cdot\text{s}^{-1}$] of the brine. If the same balance is applied regarding the salt concentration in each stream, one can write

$$\dot{m}_i \cdot \omega_i = \dot{m}_d \cdot \omega_d + \dot{m}_b \cdot \omega_b, \quad (1.2)$$

where ω_i is the salt concentration [$\text{kg}\cdot\text{kg}^{-1}$] of the influent, ω_d is the salt concentration [$\text{kg}\cdot\text{kg}^{-1}$] of the distillate and ω_b is the salt concentration [$\text{kg}\cdot\text{kg}^{-1}$] of the brine. The ratio between the salt concentration of the brine and the salt concentration of the influent is known as the *Concentration Factor* (C_f) and can be written as

$$C_f = \frac{\omega_b}{\omega_{sw}}. \quad (1.3)$$

The concentration factor is a well known performance index to compare different technologies. Another important index is the Recovery Rate (RR). It is basically the ratio between the mass flow rate of the distillate and the mass flow rate of the influent, and it can be written as

$$RR = \frac{\dot{m}_d}{\dot{m}_i}. \quad (1.4)$$

Equations (1.2), (1.3) and (1.4) can be combined if a relation between the concentration factor and the recovery rate is needed,

$$Cf = \frac{1}{1 - RR}. \quad (1.5)$$

A relation between the influent characteristics, the concentration factor and the distillate production capacity of the system can be obtained by combining equations (1.2) and (1.3). This relation is normally used to predict the production capacity of a known system,

$$\dot{m}_d = \dot{m}_i \left(1 - \frac{1}{Cf} \right). \quad (1.6)$$

From equation (1.6) we can say that the bigger the concentration factor for a certain mass flow of the influent, the more distillate will be produced. Nevertheless, there is a trade off concerning the process efficiency and the concentration factor because a higher Cf increases the possibility of scaling inside the system and decreases the thermal conductivity of the liquid. Normal and recovery ratios for some desalination technologies are presented in table 1.

Table 1.1: Recovery ratio (%) of different desalination technologies by different authors.

Author	RR(%)		
	MSF	MED	SWRO
Kawajhi [29]	30-5	na	35
Corrado [31]	30-50	40-50	35-45
DLR [30]	25-10	23-33	20-50
Cipolina [3]	na	na	15-37
Spiegler [28]	na	na	40

5. Energy Consumption

The theoretical minimum amount of energy required to separate salt from seawater is $0.7 \text{ kWh}\cdot\text{m}^{-3}$ ²⁸ which, when compared to the current numbers^{3, 27-32} reflects the inefficiency of the current processes. When compared to traditional water treatment processes, e.g. sand filtration and groundwater intakes, desalination is also very energy demanding. An evaluation done by the Energy Center of Wisconsin (ECW) in 2000³³ showed that the energetic cost to produce one cubic meter of drinking water from a groundwater intake was only 0.47 kWh. The same cost for a surface reservoir intake was 0.33 kWh. Both values are below the theoretical minimum amount of energy needed to separate dissolved salts from seawater and much lower than the average consumption of desalination processes. Recently *Ophir and Lokiec*³⁴ presented an evaluation of MED processes and have shown that its economics are superior to other desalination processes. The authors reported that efficient MED processes can be as energy intensive as $1.2 \text{ kWh}\cdot\text{m}^{-3}$ of fresh water produced for a plant of 5 effects at a production ratio of $2\cdot 10^4 \text{ m}^3\cdot\text{day}^{-1}$.

However, some points have to be mentioned if the energy consumption of different technologies is compared. Firstly, the most efficient process is not always the most cost effective design if the price of energy is low. Secondly, the energy requirements for thermal processes (MSF, MED, and MSF) are not related to the salt concentration, while the energy requirements for membrane processes are highly dependent on this factor.

For this reason, the efficiency indexes for RO are normally provided differently for the treatment of seawater than for the treatment of lower salt concentration water^{26, 27, 31}. Thirdly, thermal energy obtained from waste heat sources is normally not considered in such calculations.

Table 1.2: Energy consumption for different desalination processes.

Technology (stand alone)	Average Consumption (kW/m ³)	Reference
Minimum	0.7	Spiegler [28]
RO	6 - 8	Malaeb [27]
	4 - 8	Mezher [33]
	2.9 - 3.7	Anderson [32]
	6 - 8	Khawaji [29]
	5	Bouguettaia [34]
	4.2	Cipollina [3]
	3 - 5	DLR [30]
	3.4 - 4.5	Somariva [31]
MSF	3.5 - 5	Mezher [35]
	69 - 83*	Mezher [33]
	4	Anderson [32]
	4	Khawaji [29]
	13	Bouguettaia [34]
	17	Cipollina [3]
	3.5	DLR [30]
	4 - 5	Somariva [31]
MED	1.5	Mezher [33]
	41 - 61*	Mezher [33]
	1.8	Khawaji [29]
	13	Bouguettaia [34]
	6.1	Cipollina [3]
	1.5	DLR [30]
	1.0 - 1.5	Somariva [31]

* Including energy consumption for heat production

The values presented in table 1.2 depend on a number of factors including differences in the size and configuration of the units, technological advances and the quality of the feed stream to be treated. Despite of these factors, it can be inferred that none of the listed processes perform well when compared to the theoretical minimum value if considered the total energy consumption.

The energy consumption of MSF, the most used thermal process, is still about 5 up to 100 times the theoretical minimum. When compared to these technologies RO is remarkably efficient. Some well adjusted systems consume as low as 4 kW·h·m⁻³.

Finally, it is important to consider that the average energy consumption of

RO systems is always about the consumption of electrical energy whereas thermal based processes use heat directly (or fuel). If it is taken into account that the conversion of fuel into electrical energy is only about 35% efficient, RO ratios are 3 times higher than the reported values¹⁹.

6. Environmental Impacts

Many aspects can be mentioned concerning the environmental impact of desalination processes and the recent advances taken to reduce it. The most mentioned impact is certainly the emission of CO₂ generated by the burning of fossil fuels in thermal processes. The intake of feed water can damage ecosystems on the seabed and organisms can get caught in the intake filters³⁵. Pre-treatment leaves its traces in the brine. In the case of thermal desalination the discharge has a higher temperature than the feed water³⁰. Coagulants and other chemicals used to prevent bio fouling, scaling and foaming are found in the outtake³⁶. Due to corrosion heavy metals end up in the discharge as well³⁶. According to Latteman and Thomas³⁵, despite many similarities of their environmental impacts, desalination plants have several differences when compared to conventional drinking water treatment plants:

- (i) they use approximately twice more source water to produce the same amount of fresh water,
- (ii) they generate discharge of elevated salinity which typically has one-and-a-half to two times higher total dissolved solids concentration than the source seawater and
- (iii) they use eight to ten times more energy to generate the same volume of fresh water.

Solutions to the above mentioned environmental issues have been proposed and studied³⁷. Renewable energy is suggested as a possible replacement for the fossil fuels. New intake systems have been developed to avoid that marine life will get entangled in the filters. Commercial reuse of the brine is an alternative to decrease the environmental impacts caused by its discharge and it

(furthermore) lowers the unit costs of freshwater^{30, 35-37}. Land filling can be used to the brine. Alternative chemicals for pre-treatment with lower toxic impact on the environment have been investigated³⁸. Backwash water from filters and cleaning water from installations can be treated before discharge³⁹. The concentration of heavy metals in the discharge can be reduced to acceptable levels if the brine is diluted with other waste streams before discharging³⁹ which also helps to decrease the impacts due to the high temperatures of the brine. A careful selection of the plant location (intake and outtake mostly) is a very important factor to decrease the impacts⁴⁰. In addition to all of this a constant monitoring of benthic organisms and underwater flora must be performed in order to observe and control the magnitude of the actual impact^{41, 42}.

7. References

1. Rosegrant, M.W., X. Cai, and S.A. Cline, *World water and food to 2025*. 2002: International Food Policy Research Institute (IFPRI).
2. IDA, I.D.A., *Worldwide Desalination Plants Inventory*. 2006.
3. Andrea Cipollina, G.M., Lucio Rizzuti, *Sewater Desalination*. 01 ed. Vol. 01. 2009, Palermo: Springer. 306.
4. Aristotle, *Meteorological*. Vol. 1. 1962, Cambridge, MA: Harvard University Press. 127.
5. E, D., *Historic background of desalination and renewable energies*. Solar Energy, 2003. **75**(5): p. 357-366.
6. Della Porta, G.B., *Magiae Naturallis Sirve de Miraculis Rerum Naturalum Libri IV*. 1st ed. 1558, Paris, Rouen.
7. Della Porta, G.B., *Magiae Naturallis Libri XX*. 2nd ed. Vol. 19th. 1589, Napoli.
8. Wheller, N.W. and W.W. Evans, *Evaporating and distilling with solar heat*, U.S.p. office, Editor. 1870.
9. Harding, J. *Apparatus for solar distillation*. in *Proceeding of the Institution of Civil Engineers*. 1883. London.
10. Leusbrock, I., *Removal of inorganic compounds via supercritical water: Fundamental and Applications*. 2011, Rijksuniversiteit Groningen: Groningen. p. 232.
11. Loef, G.O.G., *Demineralization of saline water with solar energy*. 1954, OSW.
12. Loef, G.O.G., *Solar distillation of seawater in the Virgin islands*. 1955, OSW. p. 80.
13. Loef, G.O.G., *Solar distillation pilot plant. Design modification in deep-basin still*. 1958, OSW.
14. Loef, G.O.G. *Design and cost factors of large basin-type solar stills*. in *Symposium on Saline Water Conversion*. 1957.
15. Talbert, S.G., G.O.G. Loef, and G.A. Eibling, *Manual on solar desalination of saline water*. . 1970, Columbus: Battelle Memorial Institute.
16. Cooper, P.I., *Solar distillation, Solar energy progress in Australia and New Zealand*. 1969. p. 45.
17. Baum, V.A. and R. Bairamov, *Heat and mass transfer processes in solar stills of hotbox type*. Solar Energy, 1964. **8**(3): p. 78-82.
18. Baum, V.A. and R. Bairamov, *Prospects of solar stills in Turkmenia*. Solar Energy, 1966. **10**(1): p. 38-40.

19. Miller, J.M., *Review of Water Resources and Desalination Technologies*. 2003: Albuquerque, NM.
20. Lawson, K.W. and D.R. Lloyd, *Membrane distillation*. *Journal of Membrane Science*, 1997. **124**(1): p. 1-25.
21. Khayet, M., *Membrane distillation 'Advanced Membrane Technology and Applications'*. 2nd ed. 2008, New York: John Wiley & Sons.
22. Chang, H.A., G.B. Wang, Y.H. Chen, C.C. Li, and C.L. Chang, *Modeling and optimization of a solar driven membrane distillation desalination system*. *Renewable Energy*, 2010. **35**(12): p. 2714-2722.
23. Mannella, G.A., V. Brucato, and V. La Carrubba, *Water Fluxes in Polymeric Membranes for Desalination via Membrane Distillation*, in *5th International Conference on Times of Polymers Top and Composites*, A. Damore, D. Acierno, and L. Grassia, Editors. 2010, Amer Inst Physics: Melville. p. 243-245.
24. Vega-Beltran, J.C., L. Garcia-Rodriguez, I. Martin-Mateos, and J. Blanco-Galvez, *Solar membrane distillation: theoretical assessment of multi-stage concept*. *Desalination and Water Treatment*, 2010. **18**(1-3): p. 133-138.
25. Oki, T. and S. Kanae, *Global Hydrological Cycles and World Water Resources*. *Science*, 2006. **313**(5790): p. 1068-1072.
26. Fritzmann, C., J. Löwenberg, T. Wintgens, and T. Melin, *State-of-the-art of reverse osmosis desalination*. *Desalination*, 2007. **216**(1-3): p. 1-76.
27. Malaeb, L. and G.M. Ayoub, *Reverse osmosis technology for water treatment: State of the art review*. *Desalination*, 2011. **267**(1): p. 1-8.
28. Spiegler, K.S. and Y.M. El-Sayed, *A Desalination Primer*. 1 ed. Vol. 1. 1994, Santa Maria Imbaro, Italy: Balaban desalination Publications. 216.
29. Khawaji, A.D., I.K. Kutubkhanah, and J.-M. Wie, *Advances in seawater desalination technologies*. *Desalination*, 2008. **221**(1-3): p. 47-69.
30. DLR, *Concentrating Solar Power for Seawater Desalination*. 2007, German Aerospace Center (DLR), Institute of Technical Thermodynamics: Stuttgart, Germany. p. 65.
31. Somariva, C., *Thermal Desalination*. 2010: Genoa.
32. Anderson, M.A., A.L. Cudero, and J. Palma, *Capacitive deionization as an electrochemical means of saving energy and delivering clean water. Comparison to present desalination practices: Will it compete?* *Electrochimica Acta*, 2010. **55**(12): p. 3845-3856.
33. Mezher, T., H. Fath, Z. Abbas, and A. Khaled, *Techno-economic assessment and environmental impacts of desalination technologies*. *Desalination*, 2011. **266**(1-3): p. 263-273.

34. Bouguettaia, H., S. Babay, D. Bechki, S. Boughali, B. Bouchekima, and H. Mahcena, *Potential use of small-scale desalination units in remote arid localities*. *Annales des Sciences et Technologie*, 2010. **2**.
35. Elliott, T., B. Zeier, and I. Xagorarakis, *Energy use at Wisconsin's drinking water facilities*. 2003, Energy Center of Wisconsin: Wisconsin. p. 89.
36. Ophir, A. and F. Lokiec, *Advanced MED process for most economical sea water desalination*. *Desalination*, 2005. **182**(1–3): p. 187-198.
37. Lattemann, S. and T. Höpner, *Environmental impact and impact assessment of seawater desalination*. *Desalination*, 2008. **220**(1–3): p. 1-15.
38. Roberts, D.A., E.L. Johnston, and N.A. Knott, *Impacts of desalination plant discharges on the marine environment: A critical review of published studies*. *Water Research*, 2010. **44**(18): p. 5117-5128.
39. Meneses, M., J.C. Pasqualino, R. Céspedes-Sánchez, and F. Castells, *Alternatives for Reducing the Environmental Impact of the Main Residue From a Desalination Plant*. *Journal of Industrial Ecology*, 2010. **14**(3): p. 512-527.
40. Pearce, G., *SWRO pre-treatment: Markets and experience*. *Filtration & Separation*, 2010. **47**(4): p. 30-33.
41. Kim, D.H., *A review of desalting process techniques and economic analysis of the recovery of salts from retentates*. *Desalination*, 2011. **270**(1–3): p. 1-8.
42. Hodges, B.R., J.E. Furnans, and P.S. Kulis, *Thin-Layer Gravity Current with Implications for Desalination Brine Disposal*. *Journal of Hydraulic Engineering*, 2011. **137**(3): p. 356-371.
43. Marín-Guirao, L., J.M. Sandoval-Gil, J.M. Ruíz, and J.L. Sánchez-Lizaso, *Photosynthesis, growth and survival of the Mediterranean seagrass *Posidonia oceanica* in response to simulated salinity increases in a laboratory mesocosm system*. *Estuarine, Coastal and Shelf Science*, 2011. **92**(2): p. 286-296.

Chapter 2

Electrohydrodynamic Atomization



Pictures by Luewton L F Agostinho

1. Liquid Atomization

Atomization is defined as the disintegration of a liquid into small droplets¹⁻⁵. The resulted suspension of fine droplets and/or solid particles (dispersed phase) in a surrounding gas (continuous phase) is termed *spray* or *aerosol*¹⁻⁵.

The formation of liquid droplets is a phenomenon which has intrigued scientists for many centuries. Reports about this phenomenon can be seen in the literature already from the 15th century in the book *The Codex Leicester* by *Leonardo da Vinci*⁶. In this work *Leonardo da Vinci* noted correctly that the detachment of a droplet falling from a tap is governed by the condition that gravity eventually overcomes the cohesive forces (surface tension)^{3, 6}. Yet, the critical role of surface tension in the breakup of a liquid jet was only recognized many years later by Plateau, in 1849. He mentioned that a cylindrical jet, when affected by surface tension forces, is unstable regarding surface perturbations whose wave length are bigger than the jet's circumference. Some years later Rayleigh addressed the same problem dynamically and showed that the breakup of an inviscid liquid jet is controlled by the fastest growing wavelength⁷. According to him, the wavelength of this wave (λ_{opt}) can be calculated as

$$\lambda_{opt} = 2\sqrt{2} \cdot \pi \cdot r_j \quad (2.1)$$

and it governs the droplet size as

$$\frac{4}{3} \cdot \pi \cdot r_d^3 = \lambda_{opt} \cdot \pi \cdot r_j^2, \quad (2.2)$$

with r_d being the droplet radius and r_j the jet radius^{2, 3, 5, 8}. When comparing the two equations Rayleigh came to his famous relation $r_d = 1.89 \cdot r_j$ and defined that the size of a droplet formed from the breakup of a liquid jet, for a given liquid, depends only on the system dimensions⁷.

Rayleigh's study comprises a specific case in liquid atomization known as droplet formation mechanism in the *jetting regime*. If the liquid is slowly pumped through the nozzle, it forms a pendant droplet which grows in a quasi-static balance between gravitational and surface tension forces finally detaching from the liquid meniscus^{9,10}. The droplet formation mechanism in this case is known as *dripping regime*. The transition between dripping and jetting is also reported and it is known as the *dripping faucet regime*⁹⁻¹¹. Figure 2.1 shows images of the three mentioned regimes for the same nozzle geometry.

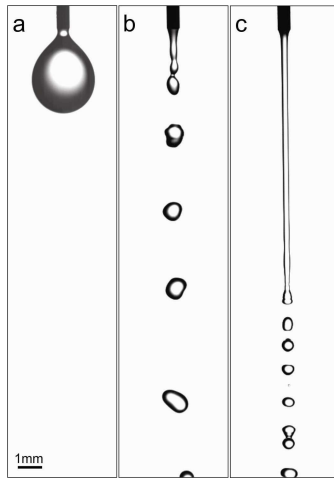


Figure 2.1 – Droplet formation mechanisms in the dripping regime (a), dripping faucet regime (b) and in the jetting regime (c).

For flow rates above the required to form the jetting regime, the relative velocity between the liquid and the surrounding air can not be neglected. Aerodynamic effects accelerate the breakup process and a shortening of the length from the nozzle exit to the droplet pinch-off is observed⁸. This regime is known as the *wind-induced regime*.

Quantitatively, the transition between the regimes depends basically on the kinetic energy of the liquid but it is also influenced by the nozzle geometry and the liquid properties, e.g. viscosity, density and surface tension. Hoeve *et al*⁸

mentioned that the lower critical velocity for jet formation in capillary flows can be expressed in terms of the liquid Weber number (We),

$$We = \frac{\rho_l \cdot r \cdot v^2}{\gamma} > 4, \quad (2.3)$$

where ρ_l is the liquid density, r is the nozzle internal radius, v is the liquid velocity and γ is the liquid surface tension. The transition between jetting and wind-induced regime happens when the inertia force of the surrounding air reaches a significant fraction of the surface tension force, so that the gas Weber number in equals

$$We_g = We \cdot \frac{\rho_g}{\rho_l} > 0.2, \quad (2.4)$$

where ρ_g is the density of the gas. These values are however only applicable for nozzles with small inner diameters, e.g. capillary nozzles, for large values the presented limits are different. A diagram showing the limits mentioned for water with different nozzle diameters is presented by the same authors ⁸.

For the conditions of the experiments performed in this thesis it was found that the dripping regime occurs at $We < 2.5$, the transition at $2.5 \leq We < 4$; and at $We \geq 4$ the jetting regime takes place. The wind-induced regime does not lie within the scope of this work.

2. Atomization Mechanisms

The disintegration of a liquid into droplets can be achieved by many different means: aerodynamically, mechanically, ultrasonically, electrostatically, etc. For example a liquid jet or sheet can be atomized by shear stress when exposed to a high-velocity gas, using the mechanical energy provided by a vibrating or rotating device, or using an electric field ^{1, 2, 4, 5}. Typical applications of these processes include spray drying, spray pyrolysis, spray freeze, drug delivery, pesticide dispersion and fire suppression. Good reviews about atomization and sprays can be found in the books of Lefebvre ², Nasser ⁵ and Liu ¹. Good reviews about droplet formation mechanisms and the breakup of liquid sheets and jets can be found in

the book of Lin ⁴ and in the review written by Eggers and Villermaux ³.

3. Electrohydrodynamic Atomization

Electrohydrodynamic atomization (EHDA), or shortly electrospraying, is an atomization process which implements electric stresses into the liquid breakup process. These stresses are inserted by creating a strong electric field in the breakup region. The method is known from its capability of controlling the diameter of the generated droplets which is provided by adjusting parameters like the properties of the solution, the nozzle geometry, the electric field characteristics and the flow rate. Among many other applications electrospraying is used for drug delivery ¹², in greenhouses ¹³ and for controlled deposition ¹⁴.

In EHDA the electric field is created by establishing an electric potential difference (Φ) between the nozzle and a counter electrode placed at a certain distance from the nozzle's tip. Various nozzle/counter electrode configurations can be used. The most known one is the nozzle/plate configuration in which the counter electrode is a metallic plate placed below the nozzle tip ¹⁴. Alternatively, configurations like double cylinders ¹⁵ and nozzle/ring ¹³ have also been successfully applied. In all the mentioned configurations the field is defined by the applied voltage, electric permittivity of the continuous phase, the chosen geometry and the interaction with other charged surfaces ¹⁶.

In most cases the liquid is pumped through the capillary at a constant rate using a precision pump, but other authors have omitted the pump and used hydrostatic pressure ^{14,17}. In this thesis the experiments were mostly performed using a ring to plate configuration and the liquid was pumped through the nozzle(s) using a precision pump.

4. Electrospraying Modes

The electric forces implemented in EHDA changes the force balance on the liquid surface and consequently the droplet formation mechanism. If the ratio between the surface tension stress and the electric stress in the liquid surface and the kinetic energy of the liquid coming out of the nozzle are carefully selected, the

classical spherical shape of the pendant droplet on the nozzle output can be changed into a conical shape, i.e. the so called Taylor Cone¹⁸. From the tip of this cone a jet emerges and breaks up into droplets. This specific droplet formation mechanism in EHDA is known as the *cone-jet mode*. For a given liquid and nozzle/counter electrode configuration different electrospray modes can be formed by changing the electric potential and the flow rate.

The first author who reported different modes in electrospray was probably Zeleny¹⁹. After him, various experimental studies revealed the existence of several electrospray modes²⁰⁻²⁵. Cloupeau and Prunet-Foch²² classified them using the spraying geometry. Their classification was further extended by Grace and Marijnissen²⁴. Few years later Jaworek and Krupa²³ suggested a classification based on characteristic time constants and on the spray current. More recently Verdoold²⁵ presented an alternative classification based on the spray current and on some characteristic numbers.

The use of diagrams to represent the different modes is very common. Some examples are the schematic diagrams presented by Geerse²⁶ and Grace and Marijnissen²⁴ and the illustrated diagrams presented by Stachewicz²⁷ and Valvo²⁸. In figure 2.2 we present a diagram (adapted from Geerse²⁶), in which we changed the window where the simple-jet mode appears. It should be noted that not for all liquids each mode can occur^{24,27}.

If we start in the dripping regime region (light grey region) it shows that for low values of the electric potential the first electrospray mode observed is the dripping mode. This mode is very similar to what is seen in the uncharged situation, i.e. droplets much bigger than the nozzle diameter detaching at very low frequencies, with the difference that electrophoretic forces induce surface charge creating a charged droplet. The frequency of dripping increases with increasing applied voltage and the diameter of the droplets decreases²¹. At lower flow rates (ϕ) the microdripping mode may occur. In this mode the droplets produced have diameter smaller than the nozzle inner diameter. For higher values of the applied potential the spindle mode or the intermittent cone-jet mode occur. Both modes constitute sprays where big and small droplets are formed alternately. In the spindle mode small droplets are formed from a jet which appears in the tip of a liquid ligament extended from the meniscus. This ligament eventually breaks up

into larger and satellite droplets. In the intermittent cone-jet mode spraying in the cone-jet mode is followed by the ejection of larger droplets²⁷.

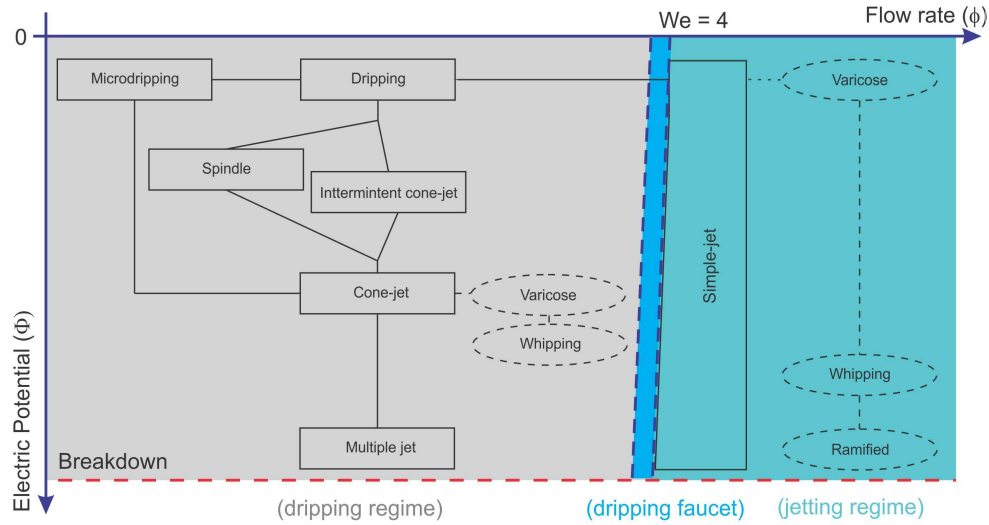


Figure 2.2 – Electro-spray modes as a function of the applied potential and flow rate for a given nozzle/counter electrode geometry and their relation with the droplet formation regimes. Adapted from the diagram presented by Geerse²⁶.

By further increasing the potential difference a stable cone-jet mode appears. In this mode the round meniscus take the shape of a Taylor cone from which a jet emerges breaking up into fine droplets due to Plateau-Rayleigh instabilities, i.e. varicose breakup. Inside the same cone-jet window, if the potential is increased, the varicose breakup is influenced by kink instabilities, i.e. whipping breakup²⁹. For even higher potentials more cone-jets appear and the multi-jet mode is formed.

In the transition and jetting regime region (blue and green regions, respectively) the simple-jet mode can appear. The diagram shows that the limits to reach these two regions in electrohydrodynamic atomization are shifted towards lower flows at higher potential differences because the axial component of the electric field accelerates the liquid. Therefore the window where it is possible to form the simple-jet mode is also extended.

Agostinho *et al*³⁰ defined the simple-jet mode as the mode in which the breakup happens from an electrified jet but at flow rates in the order of the transition and/or the jetting regime. At low electric potentials the differences between this mode and the breakup of an uncharged jet are not easily noticeable. As reported in the literature, the implementation of the electrical stresses decreases the jet radius causing a consequent decrease of the fast growing wavelength and an increase of its growth ratio^{19,31}. The differences become more pronounced at higher potentials. Similarly to what happens in the cone-jet mode, the influences of a stronger field on the liquid surface creates off-axis instabilities. These instabilities grow and make the jet whip during the breakup. We call this mechanism *simple-jet mode with whipping breakup*²⁹. At even higher potentials, for the same flow rate, the electric stresses can overcome surface tension. In this case the surface of the jet is transformed and small jets would appear along the jet surface^{32, 33}. This is called the *simple-jet mode with ramified breakup*. In our experiments we could not see this kind of breakup.

In this thesis most of the experiments were done in the *simple-jet mode with varicose breakup*. Therefore, a more detailed analysis about this mode and its intrinsic characteristics is presented in chapter three.

5. References

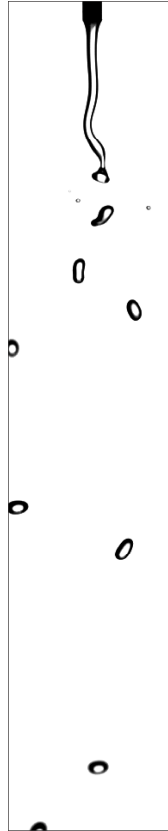
1. Liu, H., *Science and Engineering of Droplets*. Vol. 01. 1981, New York: William Andrew.
2. Lefebvre, A.H., *Atomization and Sprays*, ed. T. Francis. 1989, New York.
3. Eggers, J. and E. Villermaux, *Physics of liquid jets*. Reports on Progress in Physics, 2008. **71**(3): p. 036601.
4. Lin, S.P., *Breakup of Liquid Sheets and Jets*, ed. C. Press. 2010.
5. Ashgriz, N., *Handbook of Atomization and Sprays*. Vol. 01. 2011, New York, NY: Springer. 927.
6. Vinci, L.d., *The Codex Leicester*. 1452-519, Sidney, Australia: Powerhouse publishin.
7. Rayleigh, L., *On the Capillary Phenomena of Jets*. Proceedings of the Royal Society of London, 1879. **29**: p. 71-97.
8. Hoeve, W.v., S. Gekele, J.H. Snoeijer, M. Versluis, M.P. Brenner, and D. Lohse, *Breakup of diminutive Rayleigh jets*. Physics of Fluids, 2010. **22**(12): p. 122003.
9. Ambravaneswaran, B., S.D. Phillips, and O.A. Basaran, *Theoretical Analysis of a Dripping Faucet*. Physical Review Letters, 2000. **85**(25): p. 5332-5335.
10. Ambravaneswaran, B., H.J. Subramani, S.D. Phillips, and O.A. Basaran, *Dripping-Jetting Transitions in a Dripping Faucet*. Physical Review Letters, 2004. **93**(3): p. 034501.
11. Clanet, C. and J.C. Lasheras, *Transition from dripping to jetting*. Journal of Fluid Mechanics, 1999. **383**: p. 307-326.
12. Tang, K. and A. Gomez, *Generation by electrospray of monodisperse water droplets for targeted drug delivery by inhalation*. Journal of Aerosol Science, 1994. **25**(6): p. 1237-1249.
13. Geerse, K.B., J.C.M. Marijnissen, A. Kerssies, M. van der Staaij, and B. Scarlett, *The application of electrohydrodynamic atomization in greenhouses*. Journal of Aerosol Science, 1999. **30**(Supplement 1): p. S553-S554.
14. Stachewicz, U., C.U. Yurteri, J. Frits Dijkman, and J.C.M. Marijnissen, *Single event electrospraying of water*. Journal of Aerosol Science, 2010. **41**(10): p. 963-973.
15. Gundabala, V.R., N. Vilanova, and A. Fernandez-Nieves, *Current-Voltage Characteristics of Electrospray Processes in Microfluidics*. Physical Review Letters, 2010. **105**.
16. Hartman, R.P.A., D.J. Brunner, D.M.A. Camelot, J.C.M. Marijnissen, and B. Scarlett, *Electrohydrodynamic atomization in the cone-jet mode*. Physical

- modeling of the liquid cone and jet*. Journal of Aerosol Science, 1999. **30**(7): p. 823-849.
17. Stachewicz, U., J.F. Dijksman, D. Burdinski, C.U. Yurteri, and J.C.M. Marijnissen, *Relaxation Times in Single Event Electro spraying Controlled by Nozzle Front Surface Modification*. Langmuir, 2009. **25**(4): p. 2540-2549.
 18. Taylor, G., *Electrically Driven Jets*. Proceedings of the Royal Society of London. A. Mathematical and Physical Sciences, 1969. **313**(1515): p. 453-475.
 19. Zeleny, J., *Instability of Electrified Liquid Surfaces*. Physical Review, 1917. **10**(1): p. 1.
 20. Cloupeau, M. and B. Prunet-Foch, *Electrostatic spraying of liquids in cone-jet mode*. Journal of Electrostatics, 1989. **22**(2): p. 135-159.
 21. Cloupeau, M. and B. Prunet-Foch, *Electrostatic spraying of liquids: Main functioning modes*. Journal of Electrostatics, 1990. **25**(2): p. 165-184.
 22. Cloupeau, M. and B. Prunet-Foch, *Electrohydrodynamic spraying functioning modes: a critical review*. Journal of Aerosol Science, 1994. **25**(6): p. 1021-1036.
 23. Jaworek, A. and A. Krupa, *Classification of the modes of EHD spraying*. Journal of Aerosol Science, 1999. **30**(7): p. 975.
 24. Grace, J.M. and J.C.M. Marijnissen, *A review of liquid atomization by electrical means*. Journal of Aerosol Science, 1994. **25**(6): p. 1005-1019.
 25. Verdoold, S., *Electrohydrodynamic Atomization: Unipolar and bipolar characterization and modeling*, in *Applied Sciences*. 2012, Delft University of Technology: Delft. p. 277.
 26. Geerse, K.B., *Applications of Electro spray: from People to Plants*. 2003, Delft University of Technology: Delft.
 27. Stachewicz, U., *Analysis of Electro spraying as an On-demand Deposition Method*, in *Applied Sciences*. 2010, Delft University of Technology: Delft. p. 103.
 28. Valvo, M., *Electrospray assisted synthesis methods of nanostructured materials for Li-ion batteries*. 2010, Delft University of Technology: Delft.
 29. Hartman, R.P.A., D.J. Brunner, D.M.A. Camelot, J.C.M. Marijnissen, and B. Scarlett, *Jet break-up in electrohydrodynamic atomization in the cone-jet mode*. Journal of Aerosol Science, 2000. **31**(1): p. 65-95.
 30. Agostinho, L.L.F., C.U. Yurteri, E. Fuchs, and J.C.M. Marijnissen, *Monodisperse Water Microdroplets Generated by Electrohydrodynamic Atomization in the Simple-Jet mode*. Applied Physics Letters, 2011: p. 9.
 31. Collins, R.T., M.T. Harris, and O.A. Basaran, *Breakup of electrified jets*. Journal of Fluid Mechanics, 2007. **588**: p. 75-129.

32. Hartman, R., *Electrohydrodynamic Atomization in the Cone-Jet Mode*. 1998, Delft University of Technology: Delft. p. 178.

Chapter 3

*The simple-jet mode*¹



Picture by Siebren Brouwer

¹ This chapter is based on the publication:
Agostinho, L.L.F., G. Taminga, C.U. Yurteri S. Brouwer, E. C. Fuchs and J.C.M. Marijnissen,
Morphology of Water Electrospays in the simple-jet mode. Physics Review E, 86, 066317
(2012).

1. Introduction

Atomization is the general name for the process of disintegrating a liquid into air-borne droplets ¹. This process is mainly classified by the type of energy used to breakup the liquid. The mostly known types are: the pressure atomizers, the rotary atomizers, the ultrasonic atomizers and the electrohydrodynamic atomizers. Good reviews about atomization processes and droplet formation can be found in the books of Lefebvre ¹ and Lin ².

Looking at the droplet size, only few of the above mentioned atomization techniques are able to provide droplets in the micro and nanometer range, Electrohydrodynamic Atomization (EHDA), or electrospraying, is one of them. The process basically consists of breaking up a liquid with the implementation of an electrical field ³.

For a given liquid and setup, different combinations of the electric potential and flow rate create different spraying modes. The most studied mode is the *cone-jet mode* due to its capability to produce droplets smaller than the nozzle diameter with a narrow size distribution. The characteristics and particularities of the different modes have been extensively studied and can be found in the literature ⁴⁻⁸.

The mode on which we report here, the simple-jet mode, operates at higher flow rates than the cone-jet mode. Due to the higher inertia of the liquid in the simple-jet mode the electric field is only able to create a minor decrease in the jet diameter but still charged droplets are produced. Only few authors mentioned about it. According to Cloupeau & Prunet-Foch ⁵ and Agostinho et al ⁹ it appears when, in the presence of an electric field, the flow rate through the nozzle is sufficiently high to form a permanent jet on its output. Grace and Marijnissen ⁸ have classified it as a continuous mode (no pulsation of the liquid meniscus) which appears at the same potential level as the cone-jet mode when the flow rate is increased to form a jet.

When compared to the cone-jet mode the simple-jet mode is much less explored. A possible reason for that is the fact that the droplet size in the latter is

many times bigger than in the normal mode for the same nozzle diameter. Nevertheless, because this mode operates at high flow rates it is an interesting option for atomization methods which require high throughputs, e.g. water treatment and agricultural processes.

To the knowledge of the authors, there is no complete description of the simple-jet mode available in the literature so far. In this work our aim is to characterize this mode for inviscid liquids in relation to two control parameters, flow rate and electric field.

2. Phenomenology

In the absence of an electric field, the droplet formation mechanisms (DFM) in atomization processes through nozzles are mainly dependent on the flow rate and on the nozzle geometry. For capillary nozzles, i.e. inner diameters in the sub-millimeter range, the DFM can be divided into *dripping regime* (low flows) and *jetting regime* (high flows)¹⁰⁻¹². The differences between them can be seen in Fig. 1. In the dripping regime droplets much bigger than the nozzle inner diameter detach directly from the nozzle tip at low frequencies (Fig. 1a). In the jetting regime the droplets breakup from a liquid jet at higher frequencies and have diameter in the same order of magnitude as the nozzle inner diameter (Fig. 1c). Two classical studies about the formation of droplets in the jetting regime, i.e. breakup of liquid jets, were presented by Plateau¹³ and Lord Rayleigh¹⁴.

The transition between the dripping and the jetting regimes is also reported and it is known as the *transition regime* or the *dripping faucet regime* (DF)^{10,12}. The liquid's kinetic energy in this case is below the minimum required to form a stable jet (as seen in the jetting regime) leading to the formation of a very small jet from which the droplets breakup (figure 2.1b). Clanet and Lasheras¹² mentioned that, whereas the jet length inside the *transition regime* is rather small, once inside the *jetting regime* it is normally more than 10 times bigger than the nozzle inner diameter. We will use this value to differentiate the two regimes.

In the presence of an electric field the mechanisms responsible for the formation of the droplets depend not only on the flow rate and nozzle geometry

but also on the characteristics of this field. They result in different breakup modes which happen at flow rates comparable with the dripping regime, e.g. microdripping mode, intermittent cone-jet mode and cone-jet mode, and comparable with the jetting and transition regimes, e.g. the simple-jet mode. Despite the big difference in the flow rates used for the cone-jet mode and for the simple-jet mode, both produce droplets from the breakup of a liquid jet. However, in the cone-jet mode the jet emerges from the tip of the *Taylor Cone*¹⁵, and in the simple-jet mode directly from the nozzle tip.

At low electric field strengths there are not many differences between the simple-jet mode and the breakup of an uncharged jet (Figs. 1c and 1d). The formation of droplets under such conditions is referred to as *varicose breakup*. Many models have been developed to explain the breakup of uncharged jets including the formation of primary and satellite droplets^{2, 16-22}. For charged jets, it is a common agreement that the implementation of the electrical stresses decreases the jet radius leading to a shorter jet length (Fig. 1d)²³⁻²⁵.

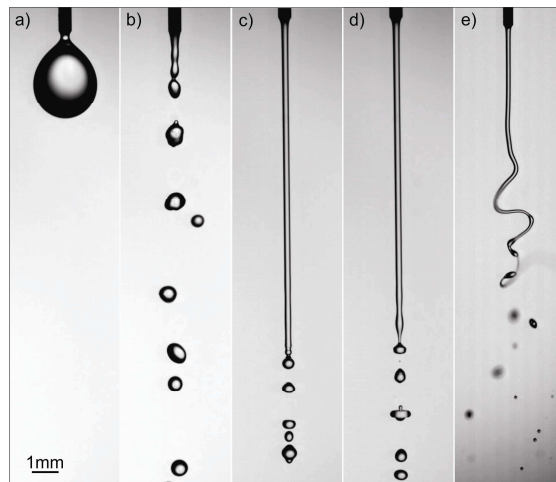


Figure 3.1 - Different hydrodynamic and electrohydrodynamic droplet formation mechanisms: (a) Dripping regime, uncharged jet; (b) Transition regime, uncharged jet; (c) Jetting regime, uncharged jet; (d) Simple-jet mode with varicose breakup, charged jet.; e) Simple-jet mode with whipping breakup, charged jet.

For higher potentials the differences are more pronounced (Fig. 3.1e). In that case the influence of the electric field creates off-axis instabilities on the jet which grow making it whip while breaking up into droplets. This breakup mechanism is known (from studies with the cone-jet mode) as *whipping* break-up²³. We will therefore refer to it as *simple-jet mode with whipping break-up*.

Another important difference when comparing the breakup of uncharged jets and the simple-jet mode is the dispersion of the droplets. In charged jets this effect is caused by Coulombic repulsion and by the action of the electric field on the charged droplets whereas for uncharged jets is almost imperceptible. Figure 3.2 shows the dispersion of the charged droplets in the simple-jet mode for a constant flow ($420 \text{ mL}\cdot\text{h}^{-1}$) and different values of the electric potential (different Electric Field strength). The relation between droplet dispersion, the flow rate and the electric potential will be further explored in this paper.

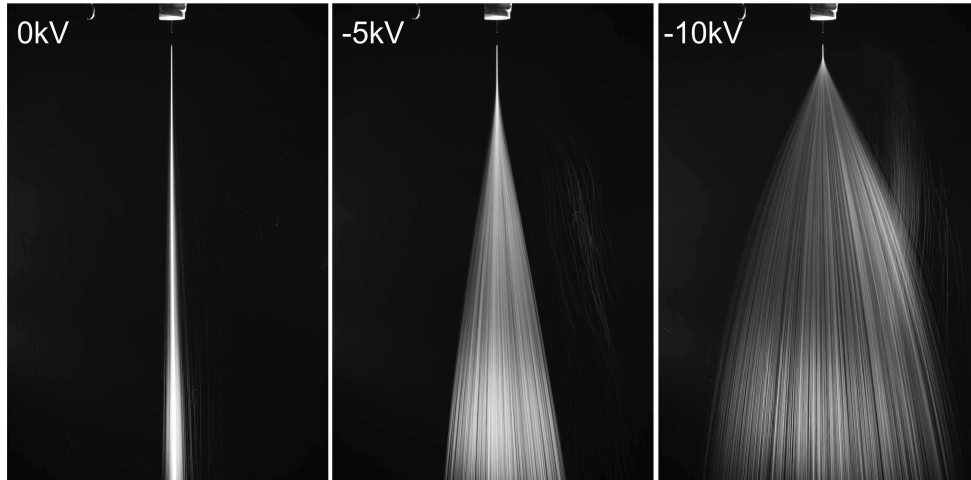


Figure 3.2 – Effect of the electric field on the charged droplets in the simple-jet mode (spray envelope). For all the pictures the liquid used is deionized water pumped through the nozzle at $420 \text{ mL}\cdot\text{h}^{-1}$. The indicated potentials were applied on the ring (not shown in the picture) with the nozzle grounded.

3. Materials and Methods

3.1 Materials

The electrospray was studied using a nozzle to ring configuration. A blunt ended, polished, stainless steel needle (FED Inc.) was used as nozzle (gauge number 22, 250 μm ID and 510 μm OD, uncoated) and a cooper ring (ID = 50mm and OD = 80mm) was used as counter electrode. A pump type SIMDOS[®] Model: FEM 1.10 KT.18S was used to force the liquid through the nozzle at a constant flow rate (Q). The liquids used in the experiments were deionized water (~ 18 M Ω ·cm, Millipore system), and a solution of deionized water and NaCl (99% Sigma Tech) with a concentration of 35 g·L⁻¹ (except when mentioned otherwise). From here on, especially in the plotted graphics, the deionized water is referred to as liquid L1; and the NaCl solution as liquid L2. Viscosity, density, relative permittivity, conductivity and surface tension (liquid-air interface) of the liquids are given in Tab. 1.

Table 3.1: Viscosity, density, relative permittivity, conductivity and surface tension (liquid-air interface) of the liquids

Liquid	μ [N.s.m ⁻²]	ρ [kg.m ⁻³]	ϵ_r	K [S.m ⁻¹]	γ [N.m ⁻¹]
L1 (Dwater)	$1.00 \cdot 10^{-3}$	$1.00 \cdot 10^3$	$8.01 \cdot 10^1$	$1.20 \cdot 10^{-3}$	$7.19 \cdot 10^{-2}$
L2 (NaCl aq.)	$9.21 \cdot 10^{-4}$	$1.05 \cdot 10^3$	$7.35 \cdot 10^1$	4.50	$7.3 \cdot 10^{-2}$

High voltage was applied with a FUG HCP 35-35000 DC high voltage power supply. In all experiments the counter electrode was set on a negative potential whereas the nozzle was grounded to avoid that high voltage would be transferred to the liquid. The distance between nozzle and ring was kept constant with the ring placed 1.7 cm above the nozzle tip as done by Geerse²⁶. A multi-meter (Fluke 8846A 6.5 digit precision multimeter) connected in series between the nozzle and the ground (not shown in the picture) was used to measure the electric current through the liquid jet.

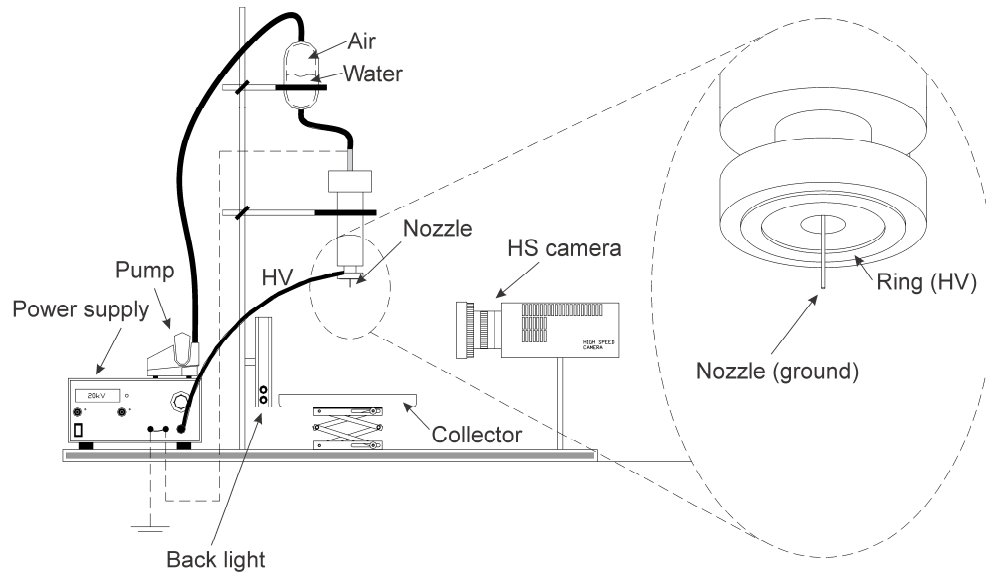


Figure 3.3 – Electro spray and optical system scheme.

Images of the breakup process and of the spray can be seen in Fig. 4. Fig 4a is a close view of the jet breakup and a simplified scheme of the nozzle-ring configuration. An air column was implemented between the pump and the nozzle input (Fig. 3) to decrease the influence of the oscillations coming from the pump on the breakup length (h_B). Fig. 4b is a snapshot of the spray on a smaller scale. Fig. 4c shows h_B and the spray obtained with the superposition of 500 images recorded at 2000 frames per second (fps). Fig. 4c also shows the dispersion angle (θ). Because the spray is quite symmetrical, the dispersion angle is defined as the angle measured between the line connecting the most external point of the spray and the breakup point and the z axis.

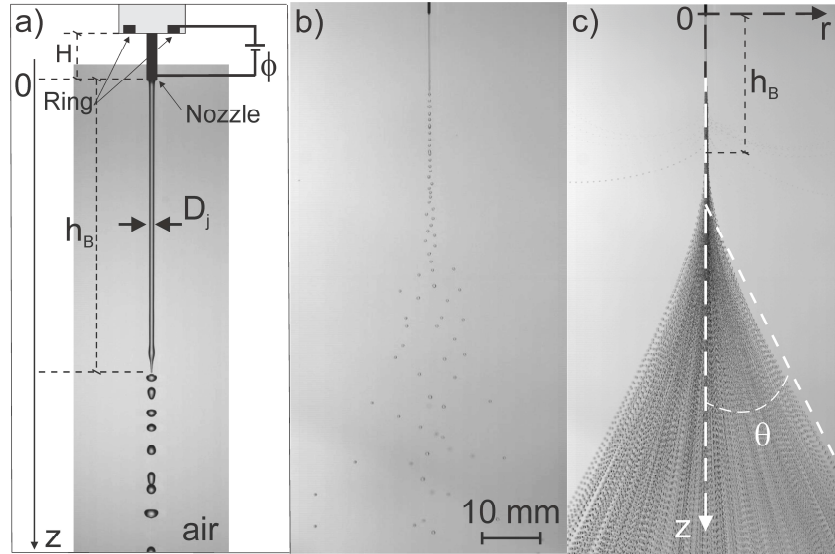


Figure 3.4 - Representation of the nozzle-ring set-up and images of the spray. 3.4a - Close view of the jet breakup with water (L1) at -6kV and $360\text{mL}\cdot\text{h}^{-1}$ and representation of the nozzle-ring setup with the defined axis and some variables. 3.4b - Snapshot of the jet with the dispersed droplets and a small part of the metallic nozzle. 3.4c - Superimposed image showing the spray envelope, the break-up length (h_B) and the envelope angle (θ).

3.2 Nondimensional numbers

To classify and characterize the spray we applied a methodology similar to that presented by Riboux *et al*²⁵ based on dimensionless numbers and on high speed imaging. The nondimensional numbers are used to correlate the parameters (control, physical and geometric parameters) and to facilitate the fitting between them and the characteristics of the spray.

The physical parameters in our case are the physical properties of the liquid: viscosity (μ), surface tension (γ), electrical conductivity (K), permittivity (ϵ) and density (ρ). The geometric parameters are the inner radius of the capillary (a) and the nozzle-ring distance (H). Both were kept constant for the experiments. The control parameters are the applied flow rate (Q) and the potential difference

between the nozzle and the ring (Φ). When combined, they can be represented as nondimensional numbers as follows:

The liquid flow rate will be represented by the liquid Weber number,

$$We = \frac{\rho_l \cdot r_j \cdot v^2}{\gamma} \quad (3.1)$$

and the gas Weber number,

$$We_g = \frac{\rho_g}{\rho_l} \cdot We \quad (3.2)$$

With r_j being the radius of the unperturbed jet, v the liquid velocity, ρ_l the liquid density and ρ_g the density of the surrounding gas. To decrease the influences created by wetting of the nozzle outer diameter, we checked at which axial position the jet radius equals the nozzle inner radius. This was found to happen at a minimum $z \cdot a^{-1} \cong 8$ (for the lower flows). Therefore we measured r_j only after this point.

In our case the two mentioned Weber numbers will be used to define whether the droplet formation mechanism is happening in the dripping regime, in the transition regime or in the jetting regime. For uncharged jets these limits were found to be $We < 1$ for the dripping regime, $1 < We < 4$ for the transition regime and $We > 4$ for the jetting regime. In all cases $We_g < 0.02$ (inertia forces of the surrounding gas can be neglected when compared to the liquid surface tension). The boundaries between the regimes for charged jets will be discussed with more details in the next section. These values are in accordance to what is found in the literature^{12, 21, 27, 28}. For the conditions of our experiments the operational intervals of these two numbers were:

$$We < 21 \text{ (} Q < 600 \text{ mL}\cdot\text{h}^{-1}\text{)} \quad (3.3)$$

$$0.006 < We_g < 0.02 \quad (3.4)$$

The electric potential will be represented by the electrical Bond number,

$$B = \frac{\varepsilon \cdot \Phi^2}{\gamma \cdot a} \quad (3.5)$$

And the nozzle to ring distance is represented by the geometrical length ratio

$$G = \frac{H}{a} \quad (3.6)$$

These last two numbers combined represent the electric field intensity. As the geometric length ratio is constant for all experiments ($G = 68$), the field intensity will be related directly with the value of B . For the conditions of the experiments the operational interval of B is:

$$0 < B < 1070 \text{ (} 0 \text{ kV} < \Phi < 11 \text{ kV)} \quad (3.7)$$

The minimum value of the electric potential was 0 kV (uncharged situation) and the maximum was 11 kV (the breakdown limit of the surrounding gas for the chosen set-up).

3.3 Experimental method

To characterize the simple-jet mode we firstly defined the operational window of the spray, i.e. the regions with a certain spray behavior as a function of the electric Bond number and the Weber number. Such diagrams have been presented by other authors in similar studies^{25, 29, 30}.

To create it we ran the spray at different flow rates ($We = 1.3 - 21$) and varied the potential until the point where the spray changed from the varicose into the whipping breakup. The experiments used to make the diagram were performed with deionized water.

Subsequently, the spray was characterized according to its electric current, generated droplet diameter (d), droplet charge (q), breakup length (h_b) and envelope angle (θ).

4. Results and Discussion

4.1 The operational window of the simple-jet mode

Figure 3.5 is a diagram which shows the operational window of the simple-jet mode based on the experimental conditions. Most experiments were done for $We > 4$. Some experiments were done for $We < 4$ (dark grey region). We performed experiments in this region to check whether the simple-jet mode could be imposed inside the transition regime for higher potentials as suggested by Cloupeau and Prunet-Foch⁶.

The value of B (for a given We) which makes the spray change from varicose into whipping breakup is represented by the closed circles in the diagram. As seen, these values increase for an increasing We . They start with $B = 609$ ($\Phi = 8.3$ kV) at $We = 4$ and go up to $B = 1070$ ($\Phi = 11$ kV) for $We = 17$. After this last point the transition values could not be defined because they were above the breakdown point of the surrounding atmosphere (spark region).

The minimum values of B necessary to initiate droplet dispersion were

determined by analyzing images of the spray taken with long exposure time from a long distance (5m from the spray axis). B minimum was taken as the value which provided a dispersion angle at least 10% bigger than found for $B = 0$. This value was arbitrarily taken to assure that the mentioned dispersion was caused by the electric field since some dispersion was also observed in the uncharged situation. These values are depicted in the diagram by the open circles.

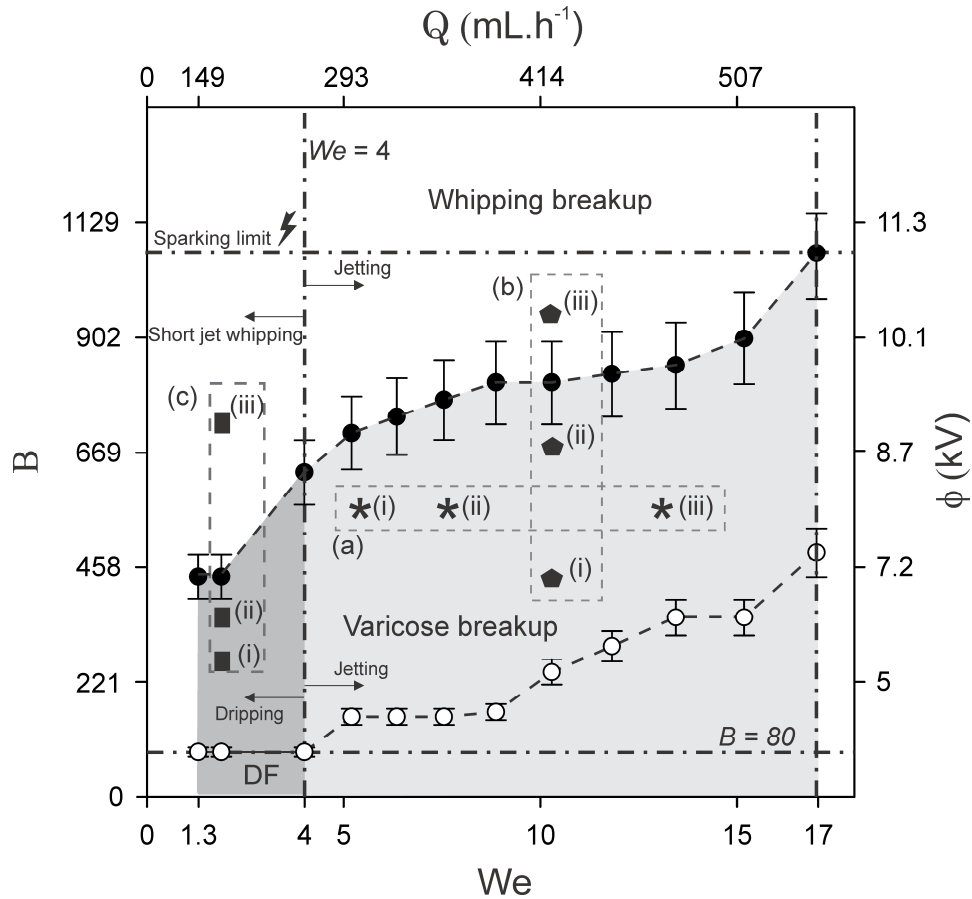


Figure 3.5 - Diagram representing the operational window of the simple-jet mode in relation to the electric Bond number (B) and the liquid Weber number (We) for deionized water. The control parameters related to B (applied potential) and We (flow) are represented on the right and upper axis, respectively.

Some additional sets of experiments were done to exemplify the influence of the control variables on the spray. These sets are enclosed inside dashed rectangles and marked as sets (a), (b) and (c). Exemplary images of the spray for each one of them are shown in Fig. 3.6.

Set (a) was done for $B = 566$ ($\Phi = 8$ kV) while We was varied between 5.2 ($Q = 300$ mL.h⁻¹) and 13.4 ($Q = 480$ mL.h⁻¹). The effect of increasing We can be seen by the increase of the breakup length and by the reduction of the envelope angle (Fig. 3.6, sequence a).

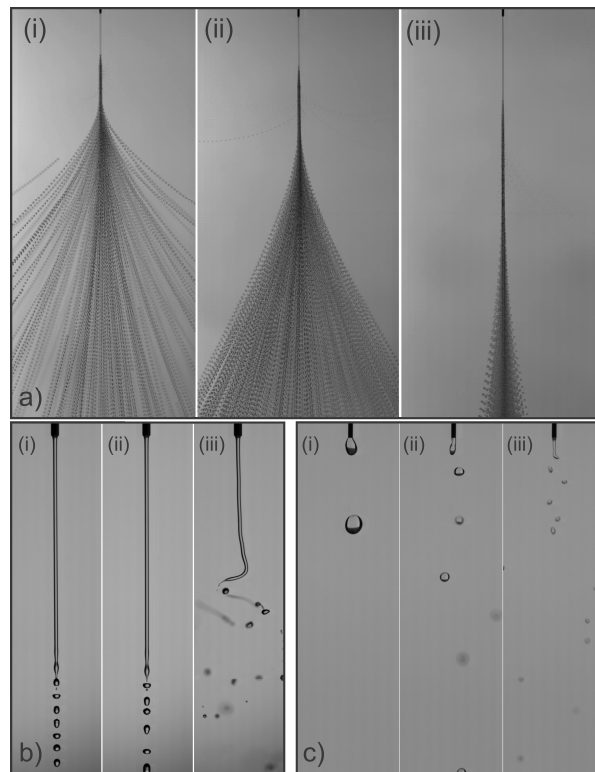


Figure 3.6 - Sequences according to the sets a), b) and c) defined in Fig. 3.5.

The next set (b) was done for a constant We (10.3) while B was varied between 433 ($\Phi = 7$ kV) and 975 ($\Phi = 10.5$ kV). This set shows the transition

between the varicose breakup and the whipping breakup which happens at $B \sim 798$ ($\Phi = 9.5$ kV). The characteristic whipping shape of the jet can be seen in figure 3.6b (iii). We have seen that, for the same flow rate, the breakup length during whipping breakup is shorter than for varicose breakup (see figure 3.6b). However further investigations on the whipping itself have to be conducted to better explain the shortening of the jet under such conditions.

In the last set (c) we investigated a possible shift from the transition regime into the jetting regime caused only by an increase of B . For that the flow was adjusted for the transition regime region ($We = 1.89$) while B varied from 239 ($\Phi = 5.2$ kV) to 685 ($\Phi = 8.8$ kV). The acceleration of the liquid provided by the axial component of the electric field causes an elongation of the jet and the formation of smaller droplets as seen in figure 3.6c(ii). However, this elongation did not create a jet longer than 20-a, even not after reaching the whipping breakup (Fig. 3.6c(iii)). The breakup as seen in figure 3.6c(iii) will be referred to as *short-jet whipping breakup*. Other experiments were done for different values of We , $1.3 \leq We \leq 3.7$, and a similar behavior was observed. These last results allowed us to define a region where the short-jet whipping is most probably occurring. This region is shown in figure 3.5.

4.2 The influence of liquid electric conductivity on the spray diagram

In the cone-jet mode it is known that the electric conductivity of the liquid plays an important role. To investigate whether this would affect the whipping and the dispersion limits in the simple-jet mode we performed experiments with deionized water and solutions of sodium chloride and deionized water with different concentrations (17, 20, 35 and 70 g L⁻¹) representing a conductivity range from 1.2 mS m⁻¹ until 9.7 S m⁻¹.

The results of these experiments are depicted in figure 3.7. From there we can see that conductivity plays a small role concerning the whipping limit and is not strongly affecting the dispersion limit.

Based on that we defined a whipping line and a dispersion line which are the linear fit of all the whipping points and the dispersion points regarding the

relation between B and We .

The correlation coefficients for the fitted lines (R^2) were 0.87 (for the whipping line) and 0.95 (for the dispersion line). Both values indicated a good linear correlation between the parameters for the two groups.

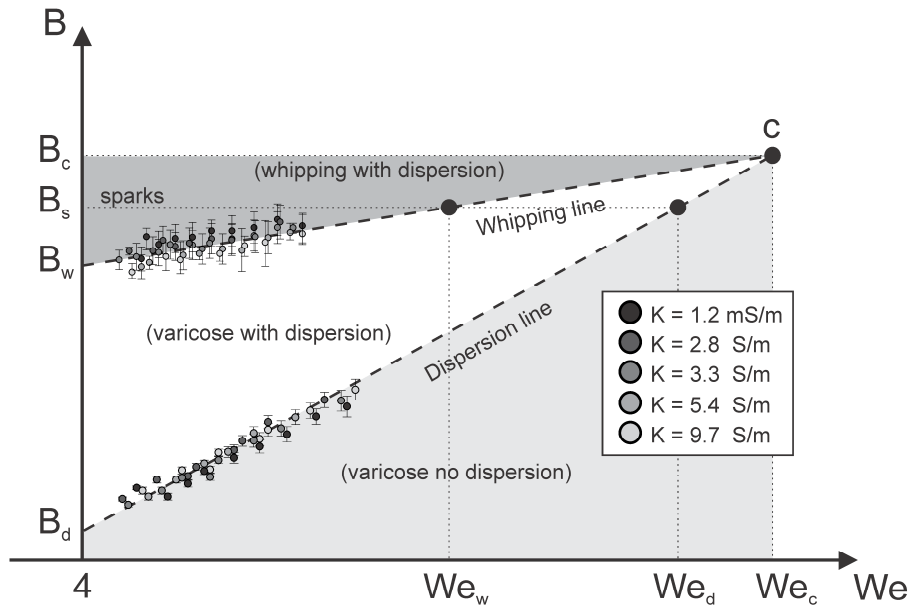


Figure 3.7 - Whipping line and dispersion line from linear fits of experiments with water and sodium chloride aqueous solutions with different concentrations (17, 20, 35 and 70 $\text{g}\cdot\text{L}^{-1}$) for different values of We and B . The insertion shows the electric conductivity of the solutions for the different concentrations respectively.

This diagram is defined only inside the jetting regime ($We > 4$). It shows primarily that liquids with different conductivities can be compared to deionized water regarding the mentioned limits. These lines define some important points, i.e. the maximum value of We to create whipping instabilities (We_w) and spray dispersion (We_d) with respect to the sparking limit (B_s), the minimum value of B to start dispersion (B_d) and to start whipping instabilities (B_w) inside the jetting regime ($We > 4$) and the critical value of We in which dispersion and whipping require the same potential (point c, figure 3.7). The value and existence of some

of the mentioned points (We_w and We_d) are intrinsically related to the sparking limit (B_s) which is a consequence of the chosen configuration and the surrounding atmosphere. Therefore, they can be manipulated if the last mentioned parameters are properly selected.

B_d , B_w and B_s are respectively 80, 609 and 1070 for the conditions of our experiments. While We_w (24.5), We_d (44.7), We_c (289) and B_c (7102) were calculated using linear extrapolation.

4.3 Jet and droplets characteristics

Figure 3.8 shows the influence of We and B on the spray (normalized) electric current, i.e. $i_n = \frac{i}{i_0}$, where i_0 is i for $B = 7.9$ ($\Phi = 1$ kV), with $i_0 \sim 2$ nA. The values of i were calculated as the average value of the electric current measured each 2 seconds during one hour for each selected potential. The error bars are the calculated standard error.

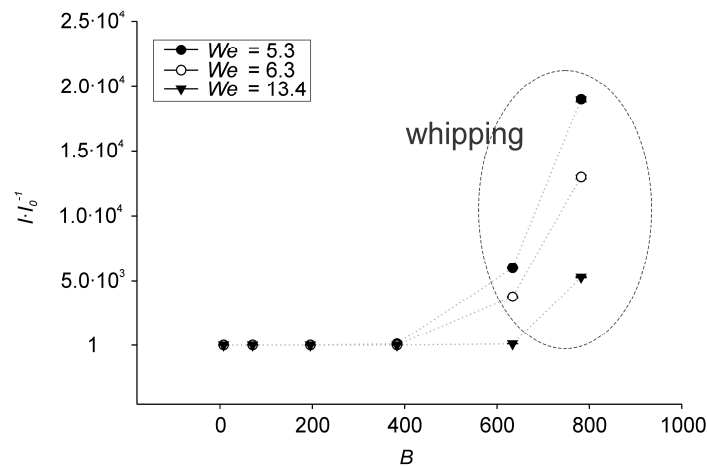


Figure 3.8 - Normalized electric current against B for three different flows ($We = 5.3$, $We = 6.3$, $We = 13.4$) for NaCl solution ($35 \text{ g}\cdot\text{L}^{-1}$). The dotted lines connecting the symbols are to guide the eyes.

From the data we could see no significant change of the spray current in the varicose breakup (see figure 3.8).

A big jump in the current values is visible when the spray reaches the whipping breakup, i.e. varicose currents are $\sim 10^{-9}$ A and whipping currents three to four orders of magnitude higher. As seen in figure 3.6b(iii) the whipping breakup creates a region where the dimensions of the jet radius gets very small. This causes a concentration of the electric field which could produce cone-jet mode spraying and justify the high value of the electric current. However, more research is necessary to get a better understanding.

The values shown in figure 3.8 show that the spray electric current can be used as an indication of the breakup mechanism.

Figure 3.9 shows the influence of the Bond number on the dimensionless jet radius ($r_j \cdot (2a)^{-1}$) at a normalized axial position $z \cdot a^{-1} = 9.4$ for different values of the liquid Weber number. We see a negative linear correlation between $r_j \cdot (2a)^{-1}$ and B . The dashed lines represent the linear fit of the correlated parameters for each examined value of We . In all cases the parameters are linearly correlated within a 95% confidence interval.

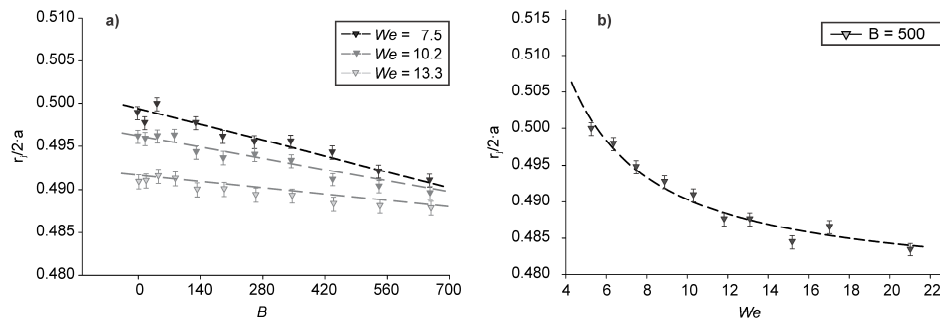
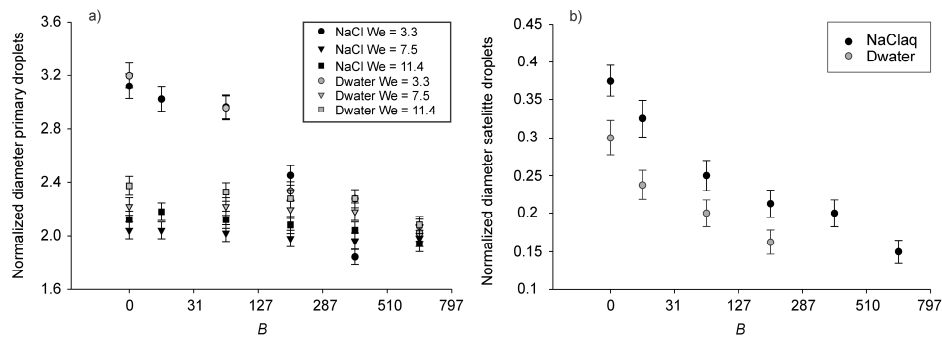


Figure 3.9 (a and b) - Jet nondimensional radius ($r_j (2a^{-1})$) against the electric Bond number at $z a^{-1} = 9.4$ for different values of the liquid Weber number and electric Bond number (3.9a) and for a constant electric Bond number and different values of We (3.9b) for liquid L2. Each data point represents the average of three or more different measurements with the error bar representing the minimum and maximum measured values.

Although not shown in the figure we performed the same experiments at different axial positions and found the same trend. Additionally, we also saw a small decrease of the jet radius for bigger axial distances. Another conclusion from the same plot is that the influence of the electric field is less pronounced for higher values of We .

Figure 3.9b shows a good exponential fit between the jet nondimensional radius and We . A similar behavior has been reported for uncharged jets^{21, 29}.

Next we investigated the diameter of the generated droplets. For that we used high speed imaging to measure the diameter of the droplets at different values of We and B for deionized water and a sodium chloride solution (35 g·L⁻¹). The images were treated with a Matlab[®] self made routine which allowed us to distinguish between primary and satellite droplets and to calculate their average diameter. The droplets diameter were normalized with the nozzle inner diameter (a) and presented as their *relative diameter* (Fig. 3.10).



Figures 3.10 (a and b) - Normalized diameter of the primary (3.10a) and satellite (3.10b) droplets generated for different values of the liquid Weber (in figure 3.10b $We = 11.4$) number and electric Bond number for deionized water and a solution of water and sodium chloride (35 g·L⁻¹). Error bars are data standard error.

From figure 3.10a we see that the average diameter of the primary droplets slightly decreases for higher values of the electric Bond number and that this influence is more pronounced at lower values of the Weber number. For the jetting regime ($We > 4$) this reduction was observed to be approximately 20% at B

= 221 ($\Phi = 5\text{kV}$) and for the transition regime ($We = 3.3$) the reduction of the primary droplet size was up to 50% when compared to the uncharged situation (see also Agostinho *et al*⁹).

From figure 3.10b we see that the diameter of the satellite droplets also decrease with B . This is contradicting what is reported by Collins *et al*²⁴ who have modeled the breakup of electrified jets and mentioned that the electrostatic stress would increase the size of the satellite droplets.

The next parameter studied was droplet surface charge. There are many models to predict the charge of formed droplets in the cone-jet mode^{25,29}, but not many information is available about this value in the simple-jet mode. In a recent work Agostinho *et al*³⁰ reported that, for the intermittent cone-jet mode, the charge of the droplets was between 2,5 and 19% of their Rayleigh limit. The method uses the droplet momentum, i.e. force balance, to estimate its charge.

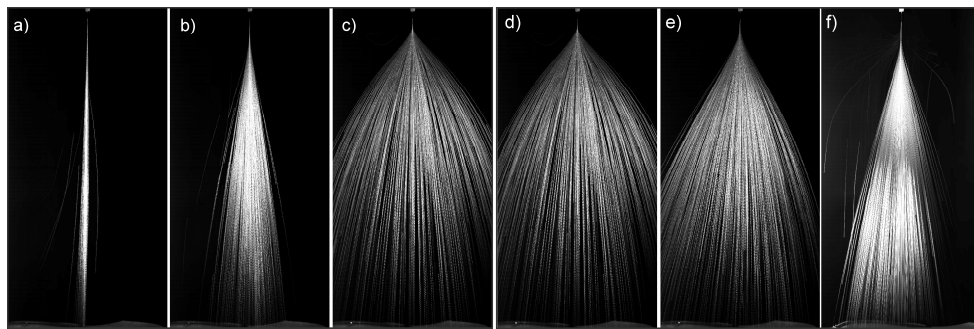


Figure 3.11: Superposed images of the droplets for $We = 5.2$ and $B = 0$ (a), $B = 280$ (b) and $B = 500$ (c) and for $B = 500$ with $We = 5.2$ (d), $We = 7.5$ (e) and $We = 10.3$ (f). Both experiments were performed with deionized water (L1).

In our calculations we assumed a constant charge distribution over the droplet surface and we used the electric current values to estimate the amount of charge given to the spray per second. Using high speed imaging we could calculate the amount of droplets generated in the same interval and their average diameter.

The results showed that simple-jet mode droplets are charged between 5 and 10% of their Rayleigh limit. These results also have shown that the droplet charge slightly increases with increasing We and B . No conclusive relation was yet found for different electric conductivities.

The dispersion of the droplets and the formation of the conical envelope can be seen in figure 3.11.

The figure shows that the envelope angle (θ) increases with B and decreases with We . Both are expected considering that for a given We higher values of B imply stronger fields and consequently an enhanced deflection of the droplets' trajectory in the radial direction. On the other hand, for a given B , higher values of We imply a higher droplets inertia which causes less deflection in the radial direction. A quantitative description of Fig. 3.11 is presented in Fig. 3.12.

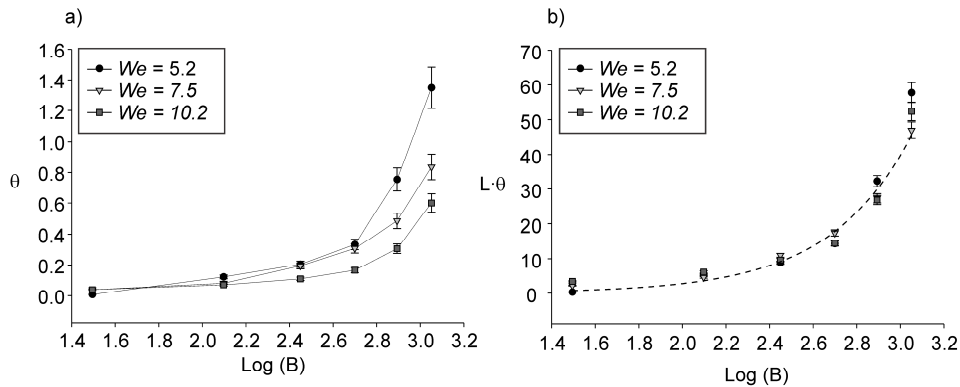


Figure 3.12 - Influence of B on θ for different values of We (a) and of B on $L \theta$ for different We (b). Each data point represents the average of the measurements with the error bar representing the minimum and maximum measured values.

Table 3.2: Break up length (h_B) and normalized breakup length (L) for different values of We and B with deionized waster (L1).

B	We = 5.2		We = 7.5		We = 10.2	
	hB (m)	L	hB (m)	L	hB (m)	L
32	0.01081	43.2	0.01413	56.5	0.02200	88.0
126	0.01078	43.1	0.01410	56.4	0.02190	87.6
281	0.01077	43.1	0.01410	56.4	0.02190	87.6
500	0.01075	43.0	0.01408	56.3	0.02180	87.2
782	0.01070	42.8	0.01406	56.2	0.02180	87.2

Fig. 3.12 shows that θ changes with B according to a power function. It is also evident that higher values of We decrease this influence while it increases the breakup length. By multiplying the normalized breakup length, i.e. $L = \frac{h_B}{2 \cdot a}$ (data presented on table 3.2), by θ the data collapse into one curve (Fig. 3.12b) and scales with B according to:

$$\ln(L \cdot \theta) \propto 3 \cdot \log_{10}(B) \quad (\text{for } B > 0) \quad (3.8)$$

5. Conclusions

The presented data show the characteristics and operational window of the simple-jet mode. It has been proven that this mode can be divided by the characteristics of its breakup mechanism and that these characteristics are a function of the liquid Weber number and the electric Bond number for a given setup. Furthermore, it was shown that the influence of the electric field decreases the size of the primary and satellite droplets and favors monodispersion. The charge of the produced droplets was calculated between 5 and 10% of their Rayleigh limit. And lastly, the dispersion of these droplets is much more pronounced than seen in uncharged jets and it is a function of the liquid Weber number and of the electric Bond number.

6. References

1. A. H. Lefebvre, *Atomization and Sprays*. (New York, 1989).
2. S. P. Lin, *Breakup of Liquid Sheets and Jets*. (2010).
3. J. Marijnissen, *J. of Aerosol Science* **35** (Supplement 1), 3-4 (2004).
4. M. Cloupeau and B. Prunet-Foch, *Journal of Electrostatics* **22** (2), 135-159 (1989).
5. M. Cloupeau and B. Prunet-Foch, *Journal of Electrostatics* **25** (2), 165-184 (1990).
6. M. Cloupeau and B. Prunet-Foch, *Journal of Aerosol Science* **25** (6), 1021-1036 (1994).
7. A. Jaworek and A. Krupa, *Journal of Aerosol Science* **30** (7), 975 (1999).
8. J. M. Grace and J. C. M. Marijnissen, *Journal of Aerosol Science* **25** (6), 1005-1019 (1994).
9. L. L. F. Agostinho, C. U. Yurteri, E. Fuchs and J. C. M. Marijnissen, *Applied Physics Letters* **100** (24), 4 (2012).
10. B. Ambravaneswaran, S. D. Phillips and O. A. Basaran, *Physical Review Letters* **85** (25), 5332-5335 (2000).
11. B. Ambravaneswaran, H. J. Subramani, S. D. Phillips and O. A. Basaran, *Physical Review Letters* **93** (3), 034501 (2004).
12. C. Clanet and J. C. Lasheras, *Journal of Fluid Mechanics* **383**, 307-326 (1999).
13. J. A. F. Plateau, *Statique expérimentale et théorique des liquides soumis aux seules forces moléculaires* (Gauthier-Villard, Paris, 1873).
14. L. Rayleigh, *Proceedings of the Royal Society of London* **29**, 71-97 (1879).
15. G. Taylor, *Proceedings of the Royal Society of London. A. Mathematical and Physical Sciences* **313** (1515), 453-475 (1969).
16. H. Zhao, H.-F. Liu, X.-K. Cao, W.-F. Li and J.-L. Xu, *Breakup characteristics of liquid drops in bag regime by a continuous and uniform air jet flow*. *International Journal of Multiphase Flow*, 2011. **37**(5): p. 530-534.
17. R. Vázquez and A. M. Gañán-Calvo, *Journal of Physics A: Mathematical and Theoretical* **43** (18), 185501 (2010).
18. M. R. Turner, J. J. Healey, S. S. Sazhin and R. Piazzesi, *Stability analysis and breakup length calculations for steady planar liquid jets*. *Journal of Fluid Mechanics*, 2011. **668**: p. 384-411.
19. P. Lafrance, *Physics of Fluids* **18** (4), 428-432 (1975).

20. Furlani, E.P. and M.S. Hanchak, *Nonlinear analysis of the deformation and breakup of viscous microjets using the method of lines*. International Journal for Numerical Methods in Fluids, 2011. **65**(5): p. 563-577.
21. J. Eggers and E. Villermaux, Reports on Progress in Physics **71** (3), 036601 (2008).
22. G. F. Christopher and S. L. Anna, Journal of Rheology **53** (3), 663 (2009).
23. R. P. A. Hartman, D. J. Brunner, D. M. A. Camelot, J. C. M. Marijnissen and B. Scarlett, Journal of Aerosol Science **31** (1), 65-95 (2000).
24. R. T. Collins, M. T. Harris and O. A. Basaran, Journal of Fluid Mechanics **588**, 75-129 (2007).
25. G. Riboux, Á. G. Marín, I. G. Loscertales and A. Barrero, Journal of Fluid Mechanics **671**, 226-253 (2011).
26. Geerse, K.B., *Applications of Electrospray: from people to plants*. 2003, PhD Thesis. Delft University of Technology: Delft.
27. M. M. Hohman, M. Shin, G. Rutledge and M. P. Brenner, Physics of Fluids **13** (8), 2201-2220 (2001).
28. M. M. Hohman, M. Shin, G. Rutledge and M. P. Brenner, Physics of Fluids **13** (8), 2221-2236 (2001).
29. N. Ashgriz, *Handbook of Atomization and Sprays*. (Springer, New York, NY, 2011).
30. L. L. F. Agostinho, E. C. Fuchs, S. J. Metz, C. U. Yurteri and J. C. M. Marijnissen, *Reverse movement and coalescence of water microdroplets in electrohydrodynamic atomization*. Physical Review E, 2011. **84**(2): p. 026317.

Appendix 3A

Nozzle/ringup, nozzle/ringdown or nozzle/plate?

The nozzle to plate configuration is a classical configuration used in electrospray. The majority of the literature about this subject is based on this configuration [1-5]. In this case, the plate is used as a counter electrode to create the necessary electric field between it and the nozzle tip. After electrosprayed the droplets are normally collected on the plate surface which, in some cases, is not desirable because can disturb the characteristics of the electric field and consequently the spray itself.

The nozzle to ring configuration with the ring placed beneath the nozzle tip was probably proposed to overcome this accumulation problem. This configuration can create a similar electric field and, if well adjusted, the droplets pass through the ring avoiding accumulation on its surface. A common problem in that case is the presence of returning droplets which can collide with the ring.

Both mentioned configurations have the disadvantage that, if the droplets are produced to collide with a certain surface (coating or deposition processes), this surface can not be placed close to the nozzle tip because it shields the electric field and stops the spray.

The nozzle to ring configuration with the ring placed above the nozzle tip was probably firstly proposed by Geerse [6]. In this configuration the electric field also creates the necessary conditions for electrospraying and, if well adjusted with the inertia of the produced droplets, can efficiently avoid collisions caused by returning droplets. In this configuration if the droplets are produced to collide with a certain surface it can be placed close to the nozzle tip which increases the range for possible applications.

To the knowledge of the authors, a more detailed description of the intrinsic characteristics of the electric field for the three above mentioned configurations is not available in the literature so far. This appendix is meant to

give a bit more inside information about this topic.

Comsol Multiphysics version 4.1a was used to model and compare the characteristics of the different electric fields. The model gave predictions of normal, axial and radial components of the electric field and the equipotential lines in the studied region.

The model was done with the electrostatic group of equations inside the 2D AC/DC module. Figure 3A.1 shows the 2D model geometries used to represent a cross section of each studied configuration.

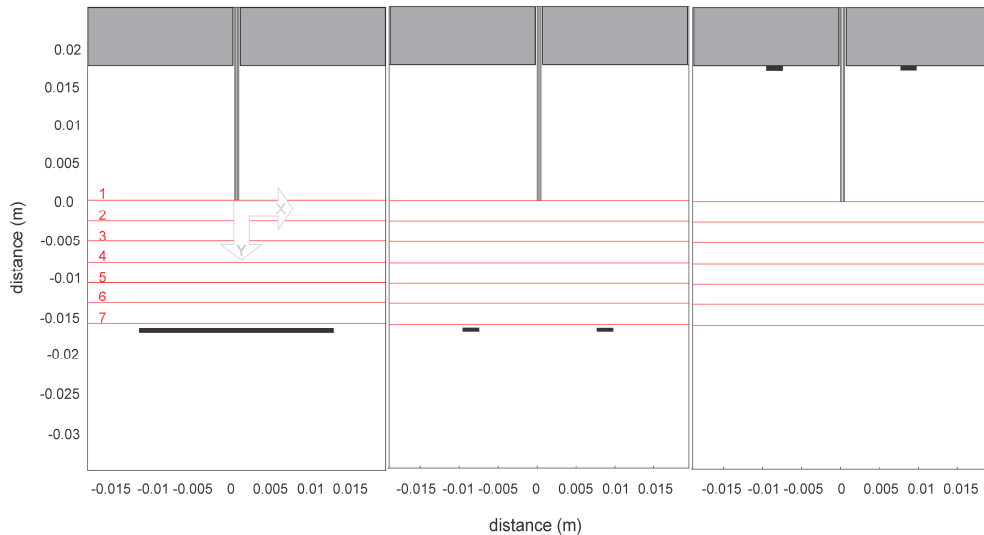


Figure 3A.1 - 2D model geometries of the studied symmetric configurations.

The counter electrodes (rings and plate) are represented by the black rectangles. The plate was drawn 25mm long and 1mm thick. The rings and nozzles were drawn with the same dimensions as used in the majority of the experiments presented in this thesis, which is: 0.51mm and 0.25mm outer and inner nozzle diameter, 25mm nozzle length, and the ring with 15mm inner diameter and 17 mm outer diameter. The distance between nozzle tip and ring in the nozzle/ringdown and nozzle/plate configuration were chosen to be the same as used in the nozzle/ringup configuration, 17mm, which is also the distance most

commonly used for the experiments.

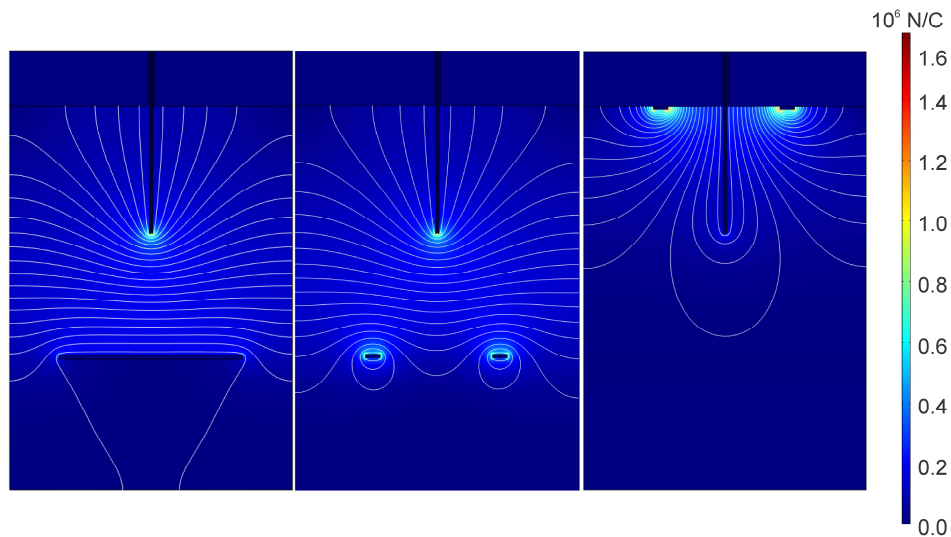


Figure 3A.2 - Surface plot (electric field) and contour plot (electric potential) plots of the configurations. The color scale applies only to the surface plot.

The top grey rectangles are to represent the insulative board which normally holds the nozzle in place. Around the whole geometry a rectangular chamber was defined to represent the surroundings (ambient air). The red lines numbered from 1 until 7 were base lines defined for the plotting of the graphics.

Comsol materials library was used to define the physical properties of the modeled objects. From it we could define the ring material as copper, the nozzles as stainless steel, the insulation board as Polyoximethylene and the surroundings as ambient air.

The boundaries conditions were defined as follows: The rings and plate boundaries were defined with a specific electric potential (-3kV). The nozzles boundaries were defined as *grounded*. The board boundaries were selected as *dielectric shielding* and the surroundings boundaries were selected as *no charge*.

Figure 3A.2 is a surface and contours plot of the configurations. The surface plot was selected as *electric field* (it represents the resultant vector of the axial and radial component of the electric field in each point) and the contour plot

is representing the equipotential lines.

As expected, the plots show higher electric field intensity close to the nozzle tip and the rings and plate corners. From the structure of the equipotential lines it is possible to see that each configuration will present electric fields with significantly different structures.

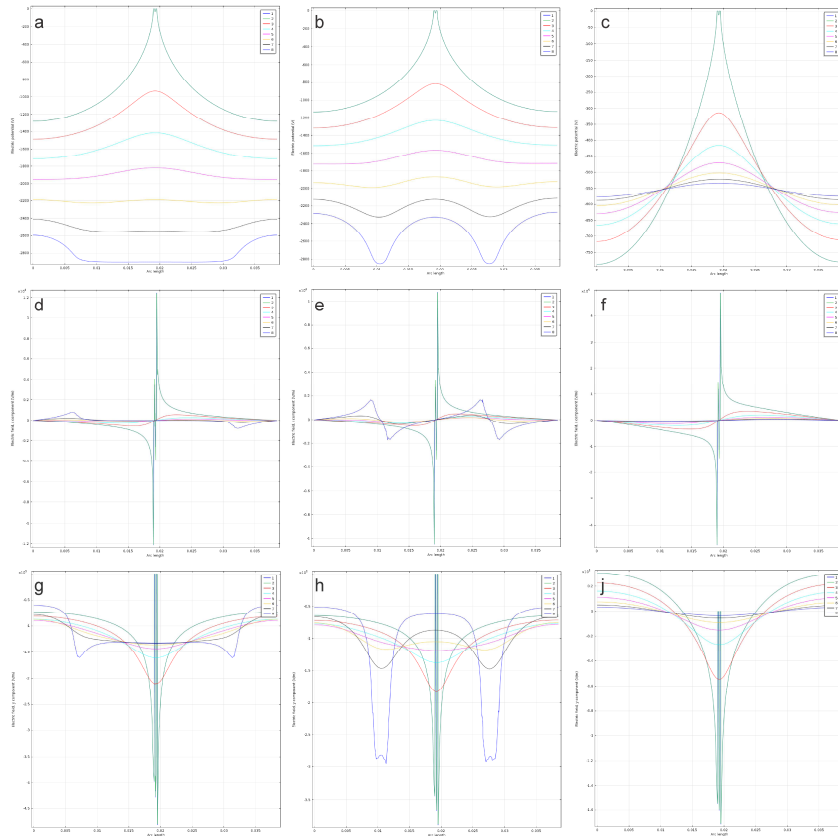


Figure 3A.3 - Electric potential (a, b and c), axial component of the electric (d, e and f) field and radial component of the electric field (g, h and e) for each configuration. Nozzle/plate plots are figures 3A.3a, 3A.3d and 3A.3g. Nozzle/ringdown are the plots shown in figures 3A.3b, 3A.3e and 3A.3h. Nozzle/ringup are the plots represented in figures 3A.3c, 3A.3f and 3A.3i.

Figure 3A.3 is a general idea for the values of the electric potential and the

radial and axial component of the electric field for the three configurations.

A more comparative idea is presented in figure 3A.4.

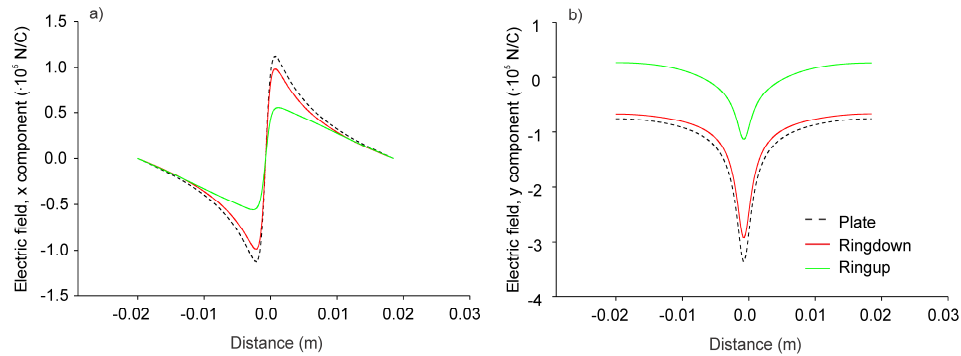


Figure 3A.4 - Radial (3A4.a) and axial (3A4.b) component of the electric field for the three configurations 1mm beneath the nozzle tip.

The figure is a comparison between the radial and axial components of the electric field measured at 1mm from the nozzle tip, 2cm along the x axis in both directions.

Firstly it is possible to see that the electric field components behave similarly (along the investigated line) for the three configurations. However, it is clear that the axial component of the ringup configuration is always smaller than the other configurations.

From figure 3A.4a it is possible to see that the axial component of the field presents a similar behavior for the three studied configurations. For the plate and ringdown configurations it reaches a maximum of $\sim \pm 1.1 \cdot 10^5$ N/C close to the nozzle tip. For the ringup configuration this value is $\sim \pm 0.5 \cdot 10^5$ N/C at the same point.

From figure 3A.4b we see that the axial component of the field also reaches its maximum at the nozzle tip. Its values for plate and ringdown configuration at this point are ~ -3.5 and $\sim -2.9 \cdot 10^5$ respectively and $\sim -1 \cdot 10^5$ N/C for the ringup configuration. Both figures show that the electric field presents the same characteristics for the three configurations. However the plate configuration

presents electric field values slightly higher than ringdown configuration for the same positions and both present values up to 2 times higher than ringup configuration for the axial component and ~3 times higher for the axial component.

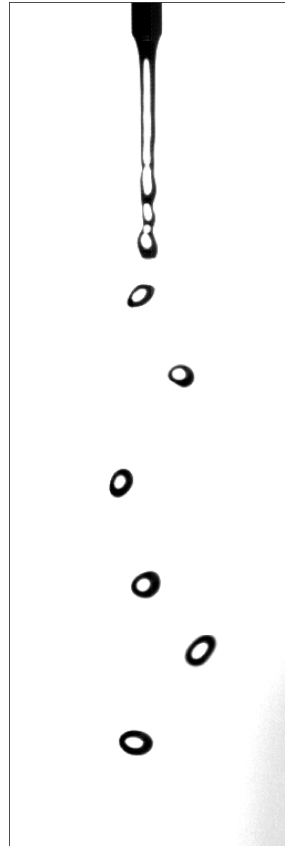
Some practical conclusions are. Firstly, the fact that the electric field presents the same characteristics close to the nozzle tip is an indication that the three configurations can be used efficiently for electro spraying in different modes. The higher values found for the axial and radial component of the electric field for plate and ringdown configuration indicate that, at the studied position, the resultant field is higher for the same applied potential compared to the ringup configuration. This might ultimately reflect on different droplets dispersion or thinner jets and consequently smaller droplets for the same potential.

References

1. Marginean, I., P. Nemes, and A. Vertes, *Astable regime in electro sprays*. Physical Review E, 2007. **76**(2): p. 026320.
2. Hartman, R.P.A., D.J. Brunner, J.C.M. Marijnissen, and B. Scarlett, *Scaling laws for droplet size and current produced in the cone-jet mode*. Journal of Aerosol Science, 1998. **29**(Supplement 2): p. S977-S978.
3. Gañán-Calvo, A.M. and J.M. Montanero, *Revision of capillary cone-jet physics: Electro spray and flow focusing*. Physical Review E, 2009. **79**(6): p. 066305.
4. Gañán-Calvo, A.M., J. Dávila, and A. Barrero, *Current and droplet size in the electro spraying of liquids. Scaling laws*. Journal of Aerosol Science, 1997. **28**(2): p. 249-275.
5. Gañán-Calvo, A.M. and A. Barrero, *A global model for the electro spraying of liquids in steady cone-jet mode*. Journal of Aerosol Science, 1996. **27**(Supplement 1): p. S179-S180.
6. Geerse, K.B., *Applications of Electro spray: from people to plants*. 2003, Delft University of Technology: Delft.

Chapter 4

Monodisperse sprays²



Picture by Anne Kamau

² This chapter is based on the publication:
Agostinho, L.L.F., C.U. Yurteri, E. C. Fuchs, and J.C.M. Marijnissen, *Monodisperse Water Microdroplets Generated by Electrohydrodynamic Atomization in the Simple-Jet mode*. Applied Physics Letters, 2012. **100**(24): p. 4.

1. Introduction

The generation of monodisperse sprays is crucial for many industrial and medical applications¹⁻⁷. Among others, such sprays can be used to control droplet deposition in ink-jet printing⁸, to improve lung targeting in drug inhalation technology^{9, 10} and they are known to enhance the evaporation rate in combustion systems¹¹.

Commonly, the droplets generated in these processes are formed from the breakup of a liquid ligament. The process is named after the mechanism used to create the filament, e.g. pressure gradients (pressure atomizers), gas streams (air assisted atomizers), centrifugal forces (rotary atomizers) and electrostatic forces (electrohydrodynamic atomizers)^{1, 12, 13}. Empirical and theoretical investigations have been done to understand the mechanism responsible for the formation of such sprays. Among them, the most famous one is the study done by Rayleigh¹⁴ who found that non-compressible inviscid liquid jets are unstable regarding axisymmetric disturbances of wave number (k) less than a certain cut-off wave number, i.e. the critical wave number (k_c) and calculated that the diameter of the formed droplet (d) is related to the jet diameter (D) as $d \approx 1.89 \times D$. It is known nowadays that for each disturbance forming a main droplet one or more usually smaller droplets (satellite or secondary droplets) can be formed¹. However, it is possible to disturb the jet such that these satellite droplets are not formed, thereby generating a monodisperse spray^{1, 15}.

From all the above mentioned atomization methods electrohydrodynamic atomization (EHDA) is one of the few which is capable to generate monodisperse micrometer size droplets. Another unique feature of this method is the electric charge acquired by the droplets which provides self dispersion and prevents coalescence^{3, 16}. In view of these appealing characteristics the production of monodisperse sprays using EHDA has attracted considerable attention in the literature^{2-7, 10, 12, 17, 18}. Some examples are the works of Tang and Gomez (1994), who investigated monodisperse electrospayed water droplets for targeted drug delivery⁷ and monodisperse sprays of low conductivity liquids³ as well as the works of Deng *et al* (2009) and Arnanthigo *et al* (2011) who have developed multiplex systems for the production of such sprays^{6, 19}. These papers consider electro spray in the cone-jet mode largely due to the fact that droplets generated

in this mode are monodisperse and much smaller than the nozzle diameter; thus, allowing the usage of big nozzles, which has advantages, i.e. less clogging. However such a mode operates at very low flow rates^{3,20-22} which is a limitation for applications requiring high throughput¹⁹, e.g. cooling towers, thermal desalination and spray drying. A solution for this problem is to operate at higher flow rates, therefore, in a different mode. According to the classifications presented by Cloupeau and Prunet Foch²³ and Grace and Marijnissen²⁴, one option would be the simple-jet mode.

In the present work we studied the production of monodisperse aqueous electrospays in the simple-jet mode. The effects of flow rate, applied voltage and electric conductivity on monodispersity and droplet size were investigated. The liquids used were deionized water and a solution of sodium chloride in deionized water. The focus is on applications which require monodisperse sprays with high throughput and droplets in the hundreds of micrometers size.

2. Materials and Method

To conduct the investigations electrospay was studied using a nozzle to ring configuration (Figure 4.1). A blunt ended, polished, stainless steel needle (FED Inc.) was used as nozzle (gauge number 22, 250 μm ID and 510 μm OD, uncoated). A pump type SIMDOS[®] Model: FEM 1.10 KT.18S was used to create a constant flow rate (Q) through the nozzle. The liquids used in the experiments were deionized water ($\sim 18 \text{ M}\Omega\text{-cm}$, Millipore system), and a solution of deionized NaCl (99% Sigma Tech) in deionized water with a concentration of 35 g/L, from now on referred to as Dwater and NaCl_{aq} respectively. Viscosity, density, relative permittivity, conductivity and surface tension (liquid-air interface) of the liquids are given in table 4.1.

Table 4.1: Viscosity, density, relative permittivity, conductivity and surface tension (liquid-air interface) of the liquids.

Liquid	μ [N.s.m ⁻²]	ρ [kg.m ⁻³]	ϵ_r	K [S.m ⁻¹]	γ [N.m ⁻¹]
Dwater	$1.00 \cdot 10^{-3}$	$1.00 \cdot 10^3$	$8.01 \cdot 10^1$	$1.20 \cdot 10^{-3}$	$7.19 \cdot 10^{-2}$
NaCl aq.	$9.21 \cdot 10^{-4}$	$1.05 \cdot 10^3$	$7.35 \cdot 10^1$	4.50	$7.3 \cdot 10^{-2}$

High voltage was applied with a FUG HCP 35-35000 DC high voltage power supply. In all experiments the counter electrode was set on a negative potential (Φ) whereas the nozzle was grounded. The distance between nozzle and ring was kept constant with the ring placed 1.7 cm above the nozzle tip as done by Geerse²⁵. A multi-meter (Fluke 8846A 6.5 digit precision multimeter) connected in series with the nozzle and the ground (not shown in the picture) was used to measure the electric current through the liquid jet. An optical system consisting of a Photron SA-1 high speed camera (HS camera) and diffused backlight illumination (Microscope light source Karl Storz Technolight 270 with liquid light guide and diffuser) was employed to record the experiments. ImageJ[®] was used for image processing; brightness and contrast corrections were done using Corel Photopaint[®] 15. After being processed the image data were analyzed statistically using a self made Matlab[®] routine.

The liquid Weber number $W_e = \frac{\rho_l \times r \times v^2}{\gamma}$ (where ρ_l is the liquid density, r

is the nozzle inner radius, v is the liquid velocity and γ is the liquid surface tension) was chosen as an indicator ascertaining the system's operation in the simple-jet mode. From the literature it is known that, for uncharged jets with $W_e \geq 4$, the droplet formation mechanism happens in the jetting regime²⁶⁻³³. Just below this value it happens in the so called *transition regime*²⁸, i.e. in between the dripping and the jetting regime. As mentioned by Cloupeau and Prunet-Foch²³ for electrified jets this transition is expected to happen at lower Weber number values, corresponding to the transition regime, because the tangential component of the electric field increases liquid acceleration. We consider the simple-jet mode as the mode in which the breakup happens from an electrified jet but at flow rates in the order of the jetting regime and the transition regime.

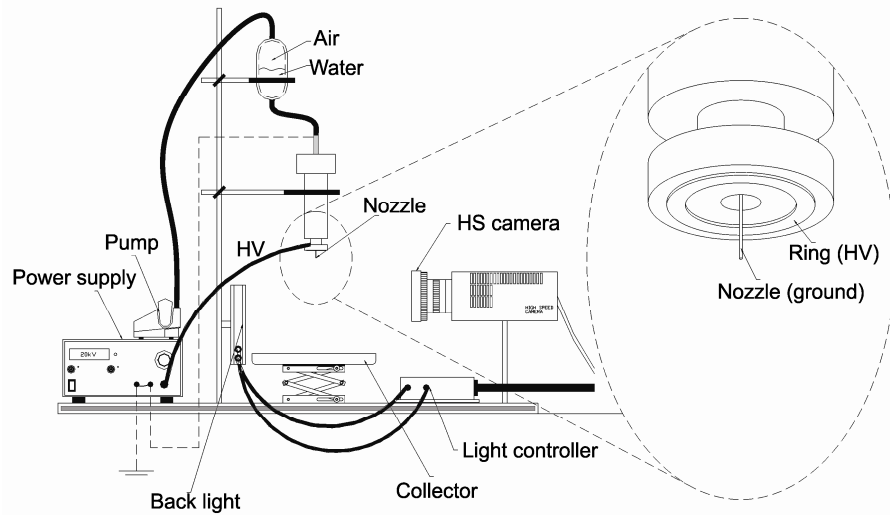


Figure 4.1 – Electro-spray and optical system scheme.

The characteristics and definition of this mode has also been reported by Agostinho *et al*³⁴. According to the authors it can be obtained when the liquid is electro-sprayed at $We \geq 4$ (jetting regime) or at lower values of We (transition regime) for certain values of the electric field. The spray size distribution was determined for three different flows $6.8 \times 10^{-8} \text{ m}^3 \cdot \text{s}^{-1}$ ($We = 3.3$), $1.02 \times 10^{-7} \text{ m}^3 \cdot \text{s}^{-1}$ ($We = 7.4$) and $1.36 \times 10^{-7} \text{ m}^3 \cdot \text{s}^{-1}$ ($We = 13.4$) for both liquids at different potentials (from 0 to -10kV). The lower flow ($We = 3.3$) was chosen expressly to investigate whether the simple-jet mode could be imposed at $We \leq 4$ and whether monodispersity could be achieved under these conditions.

3. Results and Discussion

The curves shown in Figure 4.2 are the particle size distribution of the electro-sprayed droplets. They are plotted for two different values of We (3.3 and 13.4) at different potentials (from 0 to 10 kV) for the two tested liquids (Dwater and NaCl_{aq}).

From the curves it is possible to see that inside the transition regime ($We = 3.3$) the breakup at $\Phi = 0$ creates a bimodal distribution (two peaks with similar frequencies). With the increase of the applied potential the two peaks start to merge and a more monodisperse distribution is formed. We repeated this experiment for other values of the Weber number inside the transition regime ($We = 3$ and 3.6) and the same effect was observed.

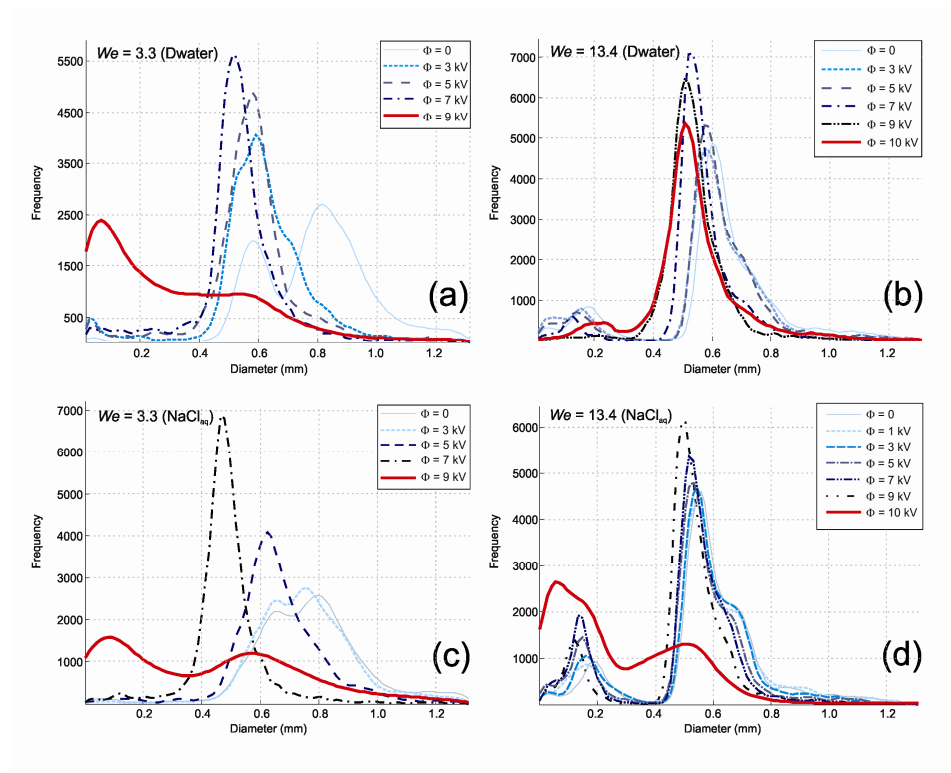


Figure 4.2(a-d) - Particle size distribution of the droplet diameters for deionized water at $We = 3.3$ (4.2a) and 13.4 (4.2b) and NaCl aqueous solution at $We = 3.3$ (4.2c) and 13.4 (4.2d) for different potentials.

Inside the jetting regime ($We \geq 4$) the effect of the applied potential on droplet size distribution is noticeable but not strongly pronounced. As can be seen in figure 4.2b and 4.2d, for $We = 13.4$ the breakup of the uncharged jet is already

rather monodisperse. Longer critical wavelengths (λ_c) are expected at this Weber number and, as a consequence, the formation of secondary or satellite droplets is likely^{1, 15, 35}. The presence of satellite droplets compromises the monodispersity because they cause a second class of diameters (smaller than the primary droplets) and they can coalesce with the main droplets generating a third (and bigger) class of diameters (tertiary droplets). This is seen in figure 4.2b and 4.2d by the presence of the two extra peaks (left and right side of the primary droplet's peak). An effect of the electric potential is decreasing the third peak (tertiary droplets). This result is due to the electric charge acquired by the droplets during atomization which causes columbic repulsion and decreases coalescence effects.

In general we noticed that an increase in potential causes a decrease of the satellite and primary droplet diameters. Regarding the primary droplets this happens because the electrostatic stresses decrease the jet radius^{15, 36, 37}, which shortens the wavelength of the fastest growing perturbation and consequently the droplet size. Similar phenomena were experimentally observed by Tang and Gomez for monodisperse sprays generated in the cone-jet mode^{3, 7}. The influence of the applied potential on the satellite droplets has not been much explored in the literature. Some examples are the work of Collins *et al*³⁷ who have modelled the breakup of electrified jets and mentioned that the electrostatic stress increases the size of the satellite droplets; and the work of Hartman *et al*³⁵ who reported that the presence and size of these droplets is a function of the electric current through the liquid jet in the cone-jet mode.

In the case of deionised water (figure 4.2b) it was remarkable to observe that the peak associated with satellite droplets has almost disappeared for $\Phi = 9$ kV and has returned at $\Phi = 10$ kV. This observation was reproducible and further investigations will be carried out to verify whether different electric fields (magnitude and direction) can be used to suppress the formation of satellite droplets and to change size distribution.

The broad size distribution presented for the two liquids for $We = 3.3$ at $\Phi = 9$ kV (figure 4.2a and 4.2c) and for the NaCl_{aq} for $We = 13.4$ at $\Phi = 10$ kV (figure 4.2d) is a consequence of whipping instabilities in the jet. As presented in literature³⁵, if the ratio between electrical and surface tension stresses

overcomes a certain threshold, off axis instabilities develop in parallel to the axisymmetric instabilities making the size distribution broader. Figure 4.3 shows images of some sprays represented in figure 4.2.

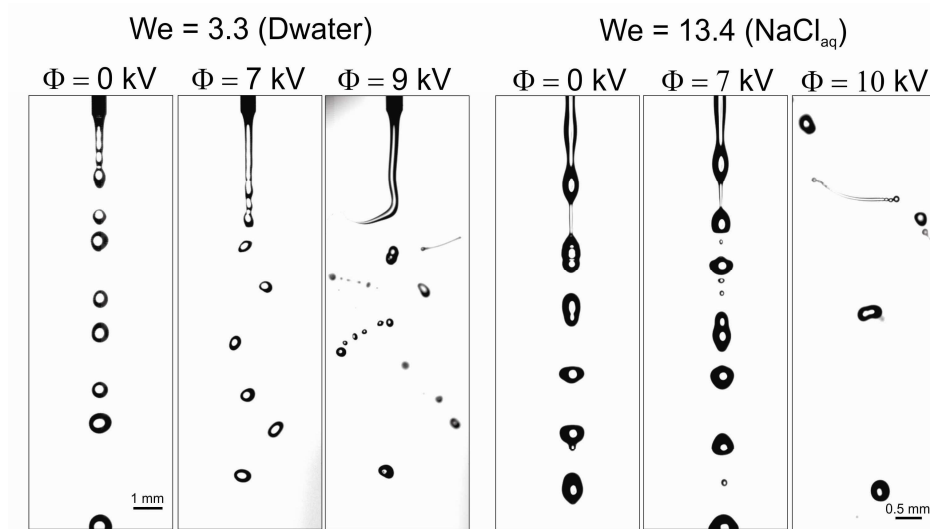


Figure 4.3 - Sprays at different potential and Weber number for Dwater and NaCl.

The bimodal distribution represented in figures 4.2a and 4.2c can clearly be seen for $We = 3.3$ and $\Phi = 0$. For the same value of We , the figure also shows a good monodispersity at $\Phi = 7$ kV and the whipping instabilities with a very broad size distribution for $\Phi = 10$ kV. For $We = 13.4$ the figure shows that the ligament between two main droplets decreases as the potential increases. Also, in the same sequence, the reduction on the primary droplet size for increasing potentials is noticeable especially for $We = 3.3$ (see also figure 4.2a).

To quantitatively describe the influence of the applied potential on the droplets size distribution we use the Relative Standard Deviation (RSD)^{2, 3, 7}.

Figure 4.4 shows that the RSD decreases with increasing potential for $We = 3.3$ and 13.4 for both liquids. The most significant reduction happens for $We = 3.3$ where the RSD decreases from 0.5 to 0.18. Sprays with RSD smaller than 0.2 are

considered monodisperse^{7,38}. For $We = 7.5$ the influence of the applied potential on the RSD is very small. This is due to the fact that such a spray is already rather monodisperse without the application of an electrical potential. Therefore, electro spraying the liquid under these conditions does not improve the droplet size distribution significantly. Comparing figures 4.4a with 4.4b shows that the influence of the liquid's electrical conductivity on the RSD is not very pronounced as the values are similar for both liquids. Extra experiments (not shown) have indicated that higher conductivities cause whipping instabilities at slightly lower potentials, meaning that the potential range wherein a monodisperse distribution can be achieved decreases with increasing conductivity. RSDs above 0.6 indicate a whipping breakup.

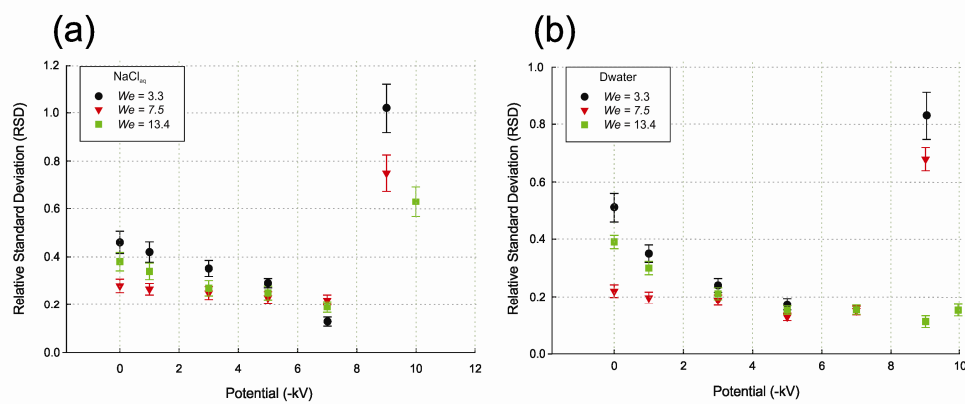


Figure 4.4 - Relative Standard Deviation (RSD) of the analyzed distributions for NaCl_{aq} (4.4a) and Dwater (4.4b) for different values of We and Φ .

For the specific kind of nozzle used in our experiments it was observed that, inside the jetting regime ($We > 4$), for the uncharged condition ($\Phi = 0$), the diameter of the primary droplets is between 2.1 and 2.2 times bigger than the nozzle's inner diameter. The application of the electric potential reduces their diameter by approximately 20% at $\Phi = 5$ kV. In the transition regime ($We = 3.3$) the reduction of the primary droplet size was up to 50% when compared to the uncharged situation. A similar result was found for the diameters of the satellite droplets which were also reduced up to 50%.

4. Conclusions

These findings lead us to infer that the electric potential can significantly change the droplet size distribution in electrosprays operating in the simple-jet mode, especially for the transition regime, i.e. for $We < 4$. We have shown that for $We = 3.3$ the RSD of the distributions can be decreased from 0.5 in the uncharged situation to 0.18 at 5 kV, values comparable to those found for monodisperse electrosprays in the cone-jet mode^{2, 3, 7}. Sprays in the jetting regime already exhibited $RSD \cong 0.2$, but the application of an electrical potential could still decrease these values.

Simple-jet mode sprays are a very good option for applications which require monodispersity of droplets in the hundreds of micrometers range with much higher throughput as the flow required for the cone-jet mode.

5. References

1. N. Ashgriz, *Handbook of Atomization and Sprays*. (Springer, New York, NY, 2011).
2. K. Tang and A. Gomez, *Journal of Colloid and Interface Science* **175** (2), 326-332 (1995).
3. K. Tang and A. Gomez, *Journal of Colloid and Interface Science* **184** (2), 500-511 (1996).
4. I. G. Loscertales, A. Barrero, I. Guerrero, R. Cortijo, M. Marquez and A. M. Ganan-Calvo, *Science* **295** (5560), 1695-1698 (2002).
5. L. Gradon and J. Marijnissen, *Optimization of Aerosol Drug Delivery*. (Kluwer academic publishers, Dordrecht, 2003).
6. W. Deng, C. M. Waits, B. Morgan and A. Gomez, *Journal of Aerosol Science* **40** (10), 907-918 (2009).
7. K. Tang and A. Gomez, *Journal of Aerosol Science* **25** (6), 1237-1249 (1994).
8. D. B. Bogy, *Annu. Rev. Fluid Mech.* **11**, 207-228 (1979).
9. D. M. Mitchell, M. A. Solomon, S. E. Tolfree, M. Short and S. G. Spiro, *Thorax* **42** (6), 457-461 (1987).
10. G. M. H. Meesters, P. H. W. Vercoulen, J. C. M. Marijnissen and B. Scarlett, *Journal of Aerosol Science* **21**, Supplement 1 (0), S669-S672 (1990).
11. F. A. Williams, *Physics of Fluids* **1** (6), 541-545 (1958).
12. A. M. Gañán-Calvo, *Physical Review Letters* **80** (2), 285-288 (1998).
13. H. Liu, *Science and Engineering of Droplets*. (William Andrew, New York, 1981).
14. L. Rayleigh, *Proceedings of the Royal Society of London* **29**, 71-97 (1879).
15. R. P. A. Hartman, D. J. Brunner, D. M. A. Camelot, J. C. M. Marijnissen and B. Scarlett, *Journal of Aerosol Science* **31** (1), 65-95 (2000).
16. L. L. F. Agostinho, J. Marijnissen, C. U. Yurteri, E. Fuchs and S. Metz, *Phys. Rev. E* (2011).
17. A. M. Ganan-Calvo and J. M. Montanero, *Phys. Rev. E* **79** (6) (2009).
18. M. A. Herrada and A. M. Gañán-Calvo, *Physics of Fluids* **21** (4), 042003 (2009).
19. Y. Arnanthigo, J. Marijnissen, C. U. Yurteri, G. Biskos and A. Schmidt-Ott, *Powder Technology* (2011).
20. M. Cloupeau and B. Prunet-Foch, *Journal of Electrostatics* **22** (2), 135-159 (1989).
21. D. M. A. Camelot, D. Brunner, R. P. M. Hartman, J. C. M. Marijnissen and B. Scarlett, *Journal of Aerosol Science* **29** (Supplement 2), S841-S842 (1998).

22. R. Hartman, Delft University of Technology, 1998.
23. M. Cloupeau and B. Prunet-Foch, *Journal of Aerosol Science* **25** (6), 1021-1036 (1994).
24. J. M. Grace and J. C. M. Marijnissen, *Journal of Aerosol Science* **25** (6), 1005-1019 (1994).
25. Geerse, K.B., *Applications of Electrospray: from people to plants*. 2003, PhD Thesis. Delft University of Technology: Delft.
26. B. Ambravaneswaran, S. D. Phillips and O. A. Basaran, *Physical Review Letters* **85** (25), 5332-5335 (2000).
27. B. Ambravaneswaran, H. J. Subramani, S. D. Phillips and O. A. Basaran, *Physical Review Letters* **93** (3), 034501 (2004).
28. C. Clanet and J. C. Lasheras, *Journal of Fluid Mechanics* **383**, 307-326 (1999).
29. W. v. Hoeve, S. Gekle, J. H. Snoeijer, M. Versluis, M. P. Brenner and D. Lohse, *Physics of Fluids* **22** (12), 122003 (2010).
30. P. Lafrance, *Physics of Fluids* **18** (4), 428-432 (1975).
31. J. Eggers and E. Villermaux, *Reports on Progress in Physics* **71** (3), 036601 (2008).
32. S. P. Lin, *Breakup of Liquid Sheets and Jets*. (2010).
33. M. Rohani, F. Jabbari and D. Dunn-Rankin, *Physics of Fluids* **22** (10), 107103 (2010).
34. L. L. F. Agostinho, J. Wartena, E. C. Fuchs, C. U. Yurteri and J. C. M. Marijnissen, presented at the European Aerosol Conference, Manchester, UK, 2011.
35. R. P. A. Hartman, D. J. Brunner, D. M. A. Camelot, J. C. M. Marijnissen and B. Scarlett, *Journal of Aerosol Science* **30** (7), 823-849 (1999).
36. A. L. Huebner and H. N. Chu, *Journal of Fluid Mechanics* **49** (02), 361-372 (1971).
37. R. T. Collins, M. T. Harris and O. A. Basaran, *Journal of Fluid Mechanics* **588**, 75-129 (2007).
38. P. A. Baron, K. Willeke and P. Kulkarni, *Aerosol Measurements: Principle, Techniques and Applications.*, 3rd ed. (Wiley and Sons., 2011).

Appendix 4A

Droplets position and velocity

To provide a better understanding of the droplets generated by the investigated sprays and their behaviour, we developed a routine which was able to split the droplets from an image sequence and determine their diameter, position (x and y), velocity and Reynolds number. The results of this analysis were presented orally during the 2009 European Aerosol Conference in Thessaloniki, Greece.

Firstly we used ImageJ[®] to treat a recorded image sequence. With the program we could isolate different droplets present in a given frame and determine their diameter (Ferrets diameter) and the position of their centroid (x,y). The position of the centroid was given in relation to a coordinate system defined as presented in figure 4A.1.

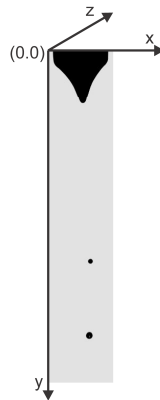


Figure 4A.1 - Axis directions and origin.

A homemade routine was then written in MatLab[®] to treat the data generated by ImageJ[®] after analyzing the complete set of images.

In this routine three matrixes were initially generated, matrix D (diameter),

Y (axial position of the droplet centroid) and X (radial position of the droplet centroid). The data about each droplet were positioned in the matrices according to their appearance in the sequence of images. These matrices were defined as follows:

$$D = \begin{bmatrix} D_{ij} & \dots & D_{im} \\ \dots & \dots & \dots \\ D_{nj} & \dots & D_{nm} \end{bmatrix}, X = \begin{bmatrix} X_{ij} & \dots & X_{im} \\ \dots & \dots & \dots \\ X_{nj} & \dots & X_{nm} \end{bmatrix} \text{ and } Y = \begin{bmatrix} Y_{ij} & \dots & Y_{im} \\ \dots & \dots & \dots \\ Y_{nj} & \dots & Y_{nm} \end{bmatrix}$$

The subscript indices i and j are respectively the number of times a droplet appeared in the image treatment *field of interest* (FOI) and the droplet number (droplets were numbered by appearance).

The droplet number (j) corresponds to the number of droplets analyzed in the whole image sequence, starting from 1 until m .

From these, two new matrices ($X2$ and $Y2$) were defined. Their elements were calculated as follows:

$$\begin{aligned} X2_{ij} &= (X_{i+1,j} - X_{ij})^2 \\ Y2_{ij} &= (Y_{i+1,j} - Y_{ij})^2 \end{aligned}, i = 1 \dots (n-1) \text{ and } j = 1 \dots m \quad (4.1)$$

The space travelled by each droplet was defined as a new matrix (S) with elements calculated as:

$$S_{ij} = \sqrt{X2_{ij} + Y2_{ij}}, i = 1 \dots n-1 \text{ and } j = 1 \dots m \quad (4.2)$$

The velocity of each droplet was defined as another matrix (V). Its elements were calculated using the elements from S and the camera frame rate as follows:

$$V_{ij} = S_{ij} \cdot fps \quad , i = 1 \dots n-1 \text{ and } j = 1 \dots m \text{ for } V_{ij} > 0 \quad (4.3)$$

Where fps is the camera frame rate.

The results obtained for the diameter of the droplets generated by a single nozzle electrospray running with $1.2 \text{ mL} \cdot \text{h}^{-1}$ and 4.5 kV are presented in figure 4A.1.

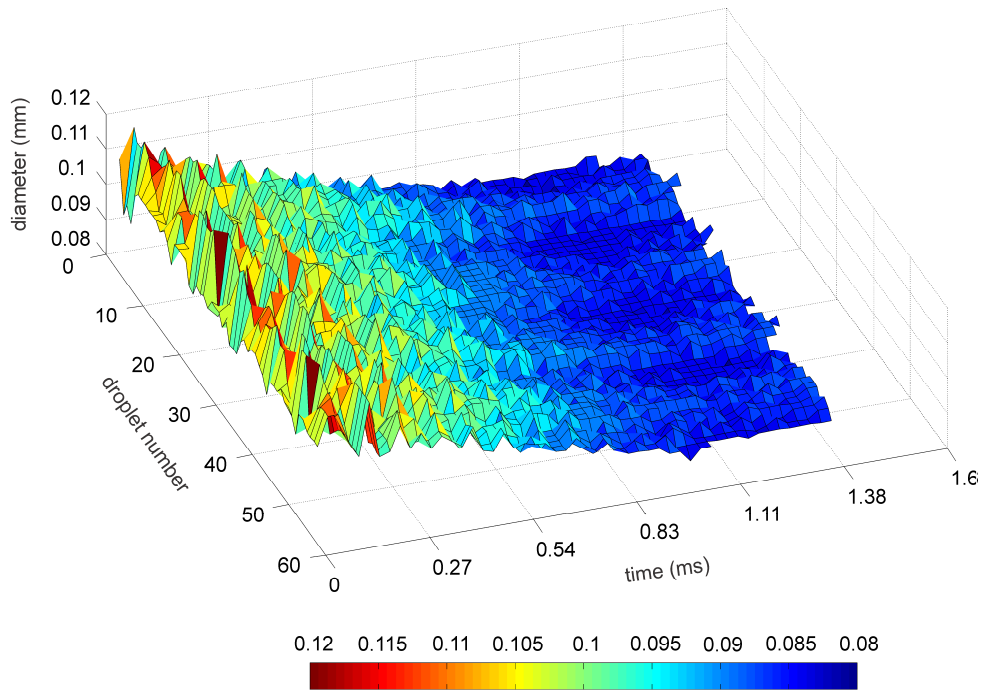


Figure 4A.2 – Droplets Ferrets diameters in a single nozzle electrospray.

For this experiment the used camera frame rate was 36k images per second in which ~ 3000 frames were recorded. Approximately 55 droplets were isolated in that case. The electrospray configuration was nozzle to ring with nozzle grounded and ring charged. The liquid is a solution of sodium chloride and deionized water ($35 \text{ g} \cdot \text{L}^{-1}$) and the nozzle dimensions are 0.25 mm and 0.51 mm inner and outer diameters respectively.

From the figure it is possible to see the variation of the droplet Ferrets

diameters created by capillary waves on the droplet surface. As expected, the oscillations are stronger after breakup and are dissipated ~0.83ms after the breakup when the diameter gets stable around 80µm. The data also show that, for the examined time, the generated spray presented a narrow size distribution.

Figure 4A.3 shows the calculated velocity for the same droplets.

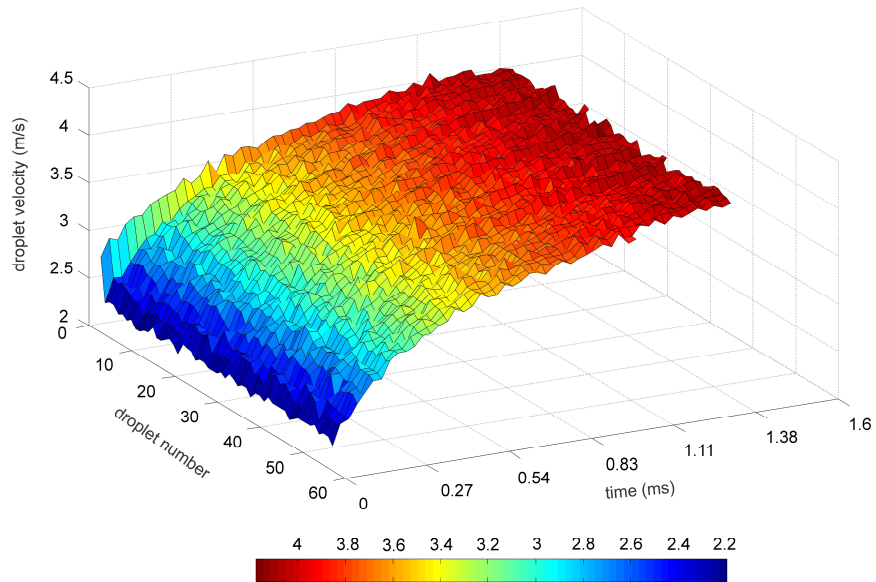


Figure 4A.3 - Droplets velocities.

It is possible to see that the droplets start their movement after the breakup with approximately 2m/s and are accelerated by the electric field and gravitational forces. After ~1.1ms they reach 4m/s, which is probably very close to their final velocity.

Using the droplets diameter and velocities we defined another matrix with elements calculated as follows:

$$M_{ij} = V_{ij} \cdot D_{i+1,j}, \quad i = 1 \dots n-1 \text{ and } j = 1 \dots m \quad (4.4)$$

And from that matrix we could define a matrix composed by the droplets Reynolds number with the elements defined as:

$$Re_{ij} = M_{ij} \cdot \frac{\rho_{air}}{\eta_{air}}, \quad i = 1 \dots n-1 \text{ and } j = 1 \dots m \quad (4.5)$$

Where ρ_{air} and η_{air} are respectively the surrounding air density and viscosity. The result is shown in figure 4A.3.

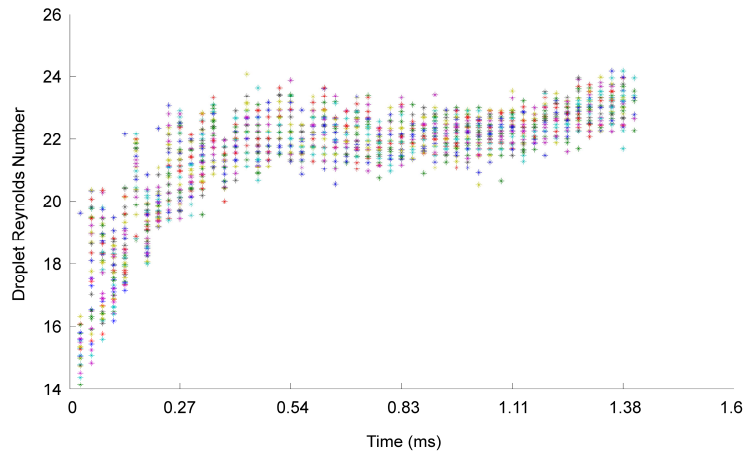
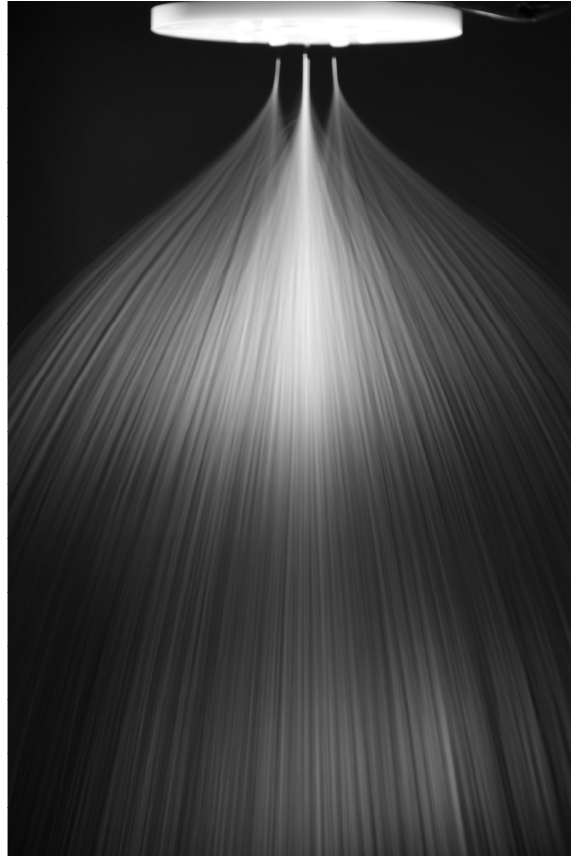


Figure 4A.4 - Droplets Reynolds numbers.

Chapter 5

Process out-scaling³



Picture by Luewton L. F. Agostinho and Siebren Brouwer

³ This chapter is based on the publication:
Agostinho, L.L.F., S. Brouwer, C.U. Yurteri, E.C. Fuchs, and J.C.M. Marijnissen, *Insulated multinozzle system for electrohydrodynamic atomization in the simple-jet mode*. Submitted to Applied Physics Letters, 2012.

1. Introduction

Electrohydrodynamic atomization (EHDA), shortly electro spraying, is the atomization of a bulk liquid under the influence of electrical forces¹⁻³. The different droplet formation mechanisms in this atomization method, also known as electro spray modes, are mainly related to the flow rate and the characteristics of the electric field⁴. Many authors have reported about the different modes in electro spray^{1,2,5-7}. Among them, Grace and Marijnissen² showed that they can be divided into two general categories: continuous and non continuous modes. The former consist of the simple-jet, the cone-jet and the ramified jet mode; the latter of the dripping, the microdripping, the spindle and the intermittent cone-jet mode. Recently Agostinho *et al.*⁸ have related the electro spray modes with the different regimes used in non-charged situations to classify the formation of the droplets, i.e. dripping regime, jetting regime and transition regime⁹⁻¹¹. The authors said that the electro spraying modes known as dripping, microdripping, spindle, intermittent cone-jet and cone-jet mode happen when the flow is adjusted to a level comparable to the dripping regime (low flow rates) and the simple-jet mode happens when the flow rate is adjusted to a level comparable to the transition and jetting regimes (higher flow rates).

EHDA in the so called cone-jet mode is widely used in processes which require droplets in the nano and micrometer size range with narrow size distribution. However, key drawbacks that have hampered its application are, first, the low flow rates and, to a lesser extent, the restrictions on the physical properties of the liquids that can be atomized with this technique¹². Good reviews about the different applications of EHDA and their characteristics can be found in the literature^{3,13,14}.

Many studies have been done on out-scaling electro spraying in the cone-jet mode. The most explored option is the design of multinozzle devices. Some examples are the works presented by Bocanegra *et al.*¹⁵, Deng *et al.*¹² and Arnanthisgo *et al.*⁴. The first authors reported on the construction and operation of a multi-hole electro spray atomizer, bearing up to 37 holes with a packing density of up to 115 emitters per square centimeter. The second reported the successful operation of a multiplexed electro spray system with a packing density of up to 11.547 sources per square centimeter. The third designed a multinozzle

electrospray device operating with high precision pumps and using a hydraulic head.

Out-scaling of EHDA by increasing the number of capillary nozzles seems to be a simple way to increase the throughput of these systems. However, factors such as electrical interferences between the neighboring sprays and non-uniformity of the liquid flow rate to all nozzles are problems that have to be overcome⁴.

Increasing the flow rate per nozzle in the cone-jet mode is not an option for out-scaling as the droplet size is a function of this parameter. It is however possible to electro spray in another mode, the simple-jet mode, which operates at much higher flow rate^{1,2,6}. Some information about this mode has been reported in the literature^{8,16,17} but it is not largely applied because it forms much bigger droplets than the cone-jet mode for the same nozzle geometry⁶. However, Agostinho *et al*¹⁷ have shown that the application of an electric field in that case can decrease the droplet diameter up to 20% in relation to the uncharged situation for the jetting regime and up to 50% in the transition regime, produces droplets with a charge of 5-10% of their Rayleigh limit and can create monodisperse sprays¹⁸. Additionally, it also provides dispersion of the droplets after the breakup¹⁷. The authors concluded that such mode is a good option for applications which require high throughput with droplets on the hundreds of micrometers range.

Taking into consideration the two options mentioned above one can expect that multinozzle systems operating in the simple-jet mode would provide a very high throughput without requiring a high packing density.

In this work we designed a multinozzle device for electro spraying in the simple-jet mode. We show that the device proposed can operate in this mode and that the characteristics of each individual nozzle are similar regarding flow per nozzle and produced droplet diameter. Additionally, an insulation layer was applied between the nozzle tip and the counter electrode to allow its operation under high humidity levels without current leakages. The proposed configuration works with the mode which presents the highest flow rate per nozzle in EHDA, therefore it offers very high throughput with very low packing density.

2. Materials and Method

Figure 5.1 is a representation of the multinozzle device. We chose for a nozzle-ring electrospray configuration with the nozzle grounded and the counter electrodes (rings) charged. The device is composed of 4 nozzles arranged in a circular configuration around a central nozzle. The configuration was chosen for its symmetry and to study the influence of neighboring nozzles on a central one. The five nozzles (EFD precision tips ID = 250 μm and OD = 510 μm) are located in a 36mm radius circumference, which gives a packing density (PD) of $2 \cdot 10^3$ nozzles·m⁻². Each nozzle is isolated by a cylindrical chamber to avoid possible contact with the counter electrodes. The counter electrodes are copper rings positioned concentrically with each nozzle and placed 1.7 cm above the nozzle tip. An insulation layer (circuit board, FR-4) is placed in between the nozzle tips and the rings (figure 5.1 caption 5) in order to keep the charged rings isolated from other parts of the device (the evaporation chamber).

The liquid used for the experiments was an aqueous solution of NaCl (Sigma Aldrich) at 35 g·L⁻¹ (physical properties listed in table 1). It was forced through an aperture on the top part of the chamber using a pump (SIMDOS® Model: FEM 1.10 KT.18S). To maintain a constant and equal flow rate through each nozzle and decrease possible oscillations from the pump a gas column was kept above the liquid/gas interface inside the pre-heating chamber. This chamber gets pressurized (1.2 - 1.6 bar) due to the action of the pump.

Table 5.1. Physical properties of the liquid.

Liquid	μ [Pa·s]	Ξ [kg·m ⁻³]	Ξ_r	K [S·m ⁻¹]	Ξ [N·m ⁻¹]
NaCl <i>aq.</i>	$9.21 \cdot 10^{-4}$	$1.05 \cdot 10^3$	$7.35 \cdot 10^1$	$4.5 \cdot 10^0$	$7.37 \cdot 10^{-2}$

In all experiments the high potential was supplied to the rings by a FUG HCP 35-35000 DC power supply while nozzles and liquid were grounded. To measure the electric current through the spray an electrometer (Fluke 8846A 6.5) was connected between the ground and the nozzles. The body of the multinozzle device (8) was made of Polyoximethylene (DELRIN) because of its high resistivity, resistance to corrosion and thermal resistance. The pressurized chamber was made of glass to allow visualization of the liquid/gas interface.

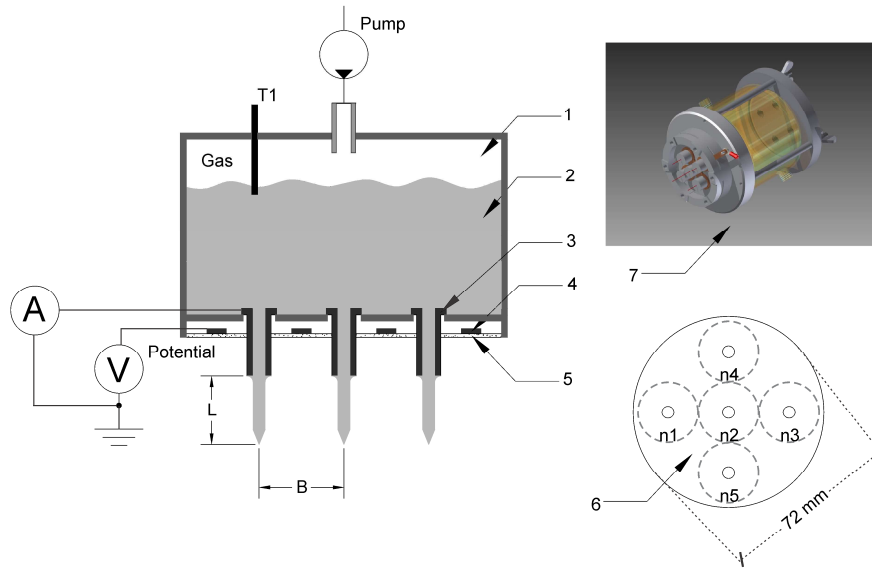


Figure 5.1 - Multinozzle configuration. (1) Gas column, (2) liquid column, (3) metallic nozzles, (4) counter electrodes (rings), (5) protective layer (insulation), (6) multinozzle array, (7) 3D view of the glass heating jacket and the multinozzle body without the insulative layer. The break-up length is represented by L and the distance between two nozzles (18mm) by B .

To define the dimensions and general characteristics of the device a theoretical analysis of its electric field was initially made using Comsol® Multiphysics 4.2. The sprays and their similarities were investigated by measuring the droplet size and breakup length (L) at each nozzle using high speed imaging (Photron SA1). After being recorded the pictures were analyzed using ImageJ® software and a homemade routine developed in Matlab®.

The experiments were done for three different flow rates (300, 360 and 420 mL/h-nozzle). For each flow rate the potential difference between nozzle and counter electrode was varied between 0 and 8 kV. The electric current for each applied potential was defined as the average value measured each 2 seconds during 10 minutes of uninterrupted spray time. The spray symmetry, droplet size distribution and droplet dispersion were investigated with respect to the applied flow rate and the potential difference by taking photographs of the spray from

large distances (4 m) using a Canon EOS 550d digital camera with frontal illumination.

A long term experiment was designed to evaluate the effectiveness of the insulation layer which was made to avoid electrical contact between the rings and other parts of the device when the spray operated at very high humidity levels. For that experiment the multinozzle device was coupled to a closed glass chamber (evaporation chamber, not shown in figure 5.1). The influent was pre-heated to 80°C and the spray was running uninterruptedly for approximately 13 hours. Humidity inside the chamber was measured using a humidity probe. The electric current, inlet temperature and the humidity inside the chamber were monitored online during the whole experiment. The experiment was repeated for 4 different potentials (2, 4 and 6 and 7 kV).

3. Results and Discussions

3.1 Breakup length and droplet size and size distribution

Figures 5.2 and 5.3 show the spray breakup length and droplet average diameter measurements, respectively, in each nozzle obtained by high speed imaging. Each data point is an average measurement of 20.000 images recorded at 1000 frames per second of the spray in each nozzle. The experiments were done in duplicate for three different flow rates (300, 360 and 420 mL·h⁻¹·nozzle⁻¹) and two different potentials (0 and 3 kV).

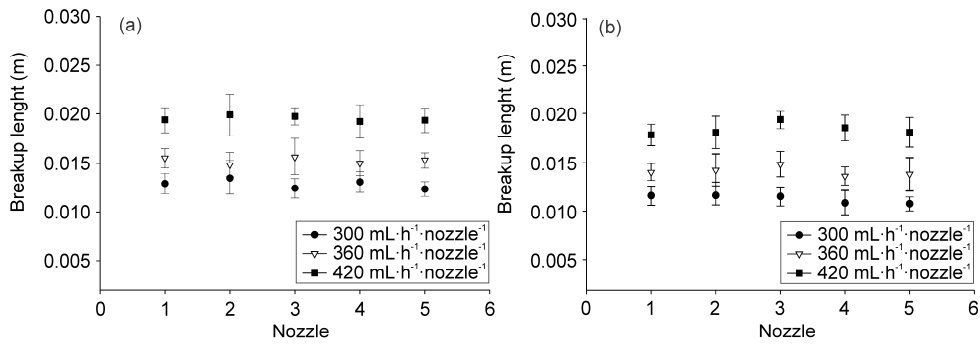


Figure 5.2 – Breakup length (L) in each nozzle at different flow rates ($300 \text{ mL}\cdot\text{h}^{-1}\cdot\text{nozzle}^{-1}$, $360 \text{ mL}\cdot\text{h}^{-1}\cdot\text{nozzle}^{-1}$ and $420 \text{ mL}\cdot\text{h}^{-1}\cdot\text{nozzle}^{-1}$) for 0 (5.2a) and 3 kV (5.2b). Error bars represent the standard error of each measurement.

Figure 5.2 shows a constant breakup length for each nozzle which indicates a similar flow rate through each of them for both situations (with and without the application of the electric potential). The similar breakup length found at each nozzle for the uncharged situation ($\Phi = 0$) is an indication that the flow rate is equally distributed over them. The fact that the same behavior is seen for the charged situation ($\Phi = 3\text{kV}$) might be an indication that the magnitude and characteristics of the electric field are similar in each nozzle.

As expected L increases with increasing flow rate^{3, 19, 20} and a small decrease is observed with the application of an electric potential. This reduction is probably caused by the reduction of the jet radius due to the influence of the electric field²¹. Such behavior is known and was recently reported by Agostinho *et al.* in a study about the characteristics of the simple-jet mode¹⁷.

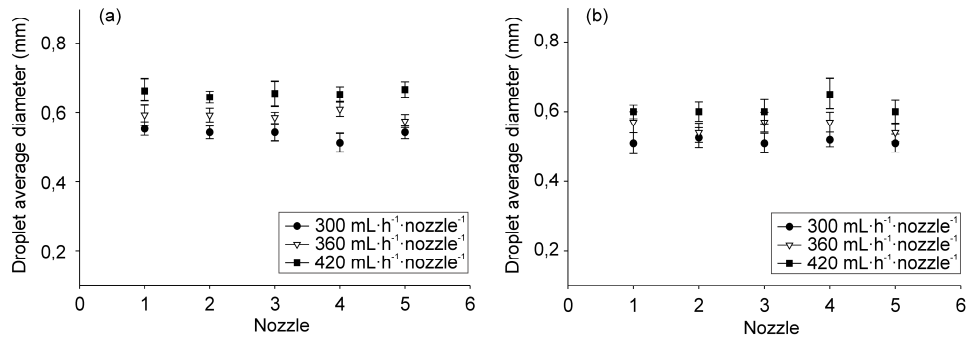


Figure 5.3 – Droplet average diameter in each nozzle at different flow rates (300 mL·h⁻¹·nozzle⁻¹, 360 mL·h⁻¹·nozzle⁻¹ and 420 mL·h⁻¹·nozzle⁻¹) for 0 (5.3a) and 3 kV (5.3b). Error bars represent the standard error of each measurement.

Figure 5.3 shows similar average droplet diameters for all the nozzles for the different flow rates and potential differences. This is expected as the diameter of the droplets generated under such conditions is a function of the jet radius which also determines the breakup length³. Additionally, the data show a small decrease of the droplet diameter with the application of the electric potential and an increase of the same parameter for higher flow rates.

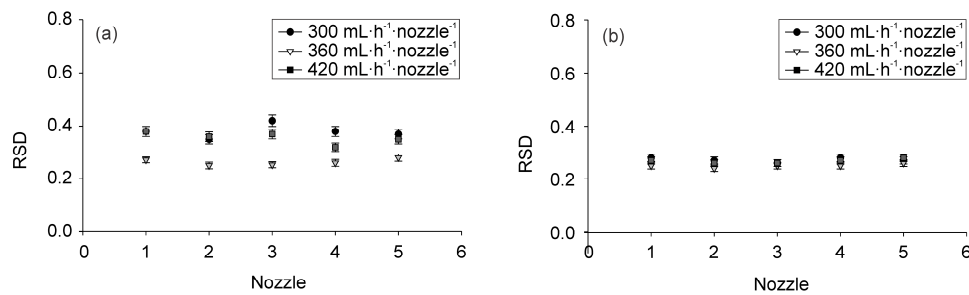


Figure 5.4 – Relative standard deviation of the generated droplets in each nozzle at different flow rates (300 mL·h⁻¹·nozzle⁻¹, 360 mL·h⁻¹·nozzle⁻¹ and 420 mL·h⁻¹·nozzle⁻¹) for 0 (5.4a) and 3 kV (5.4b). Error bars are calculated error based on the distributions.

The influence of the applied potential on the droplet size distribution is shown in figure 5.4. It is possible to see that the spray initially present a relative standard deviation (RSD), i.e. ratio between the standard deviation and the droplet average size, of approximately 0.4 for the 300 and 420 mL·h⁻¹·nozzle⁻¹ and 0.25 for 360 mL·h⁻¹·nozzle⁻¹. After the application of the electric potential (3kV) the RSD of the three flow rates decreases to ~0.22. This is an indication that the application of the electric potential improves size distribution, i.e. it favors the production of monodisperse sprays. The plot also shows RSD values comparable for all nozzles.

3.2 – Droplet dispersion

The multinozzle spray was also studied regarding the dispersion of the produced droplets. Figure 5.5 is a view of the spray for a constant flow rate (300 mL·h⁻¹·nozzle⁻¹) and different electric potentials (0 to 7.5 kV). The influence of the applied potential is immediately seen because the dispersion of the droplets is enhanced as it increases. The figure also shows that the droplets produced by the outside nozzles are similarly dispersed in relation to the central nozzle for all the applied potentials. This can be related to the previously mentioned facts that the spray behaves identically for all nozzles.

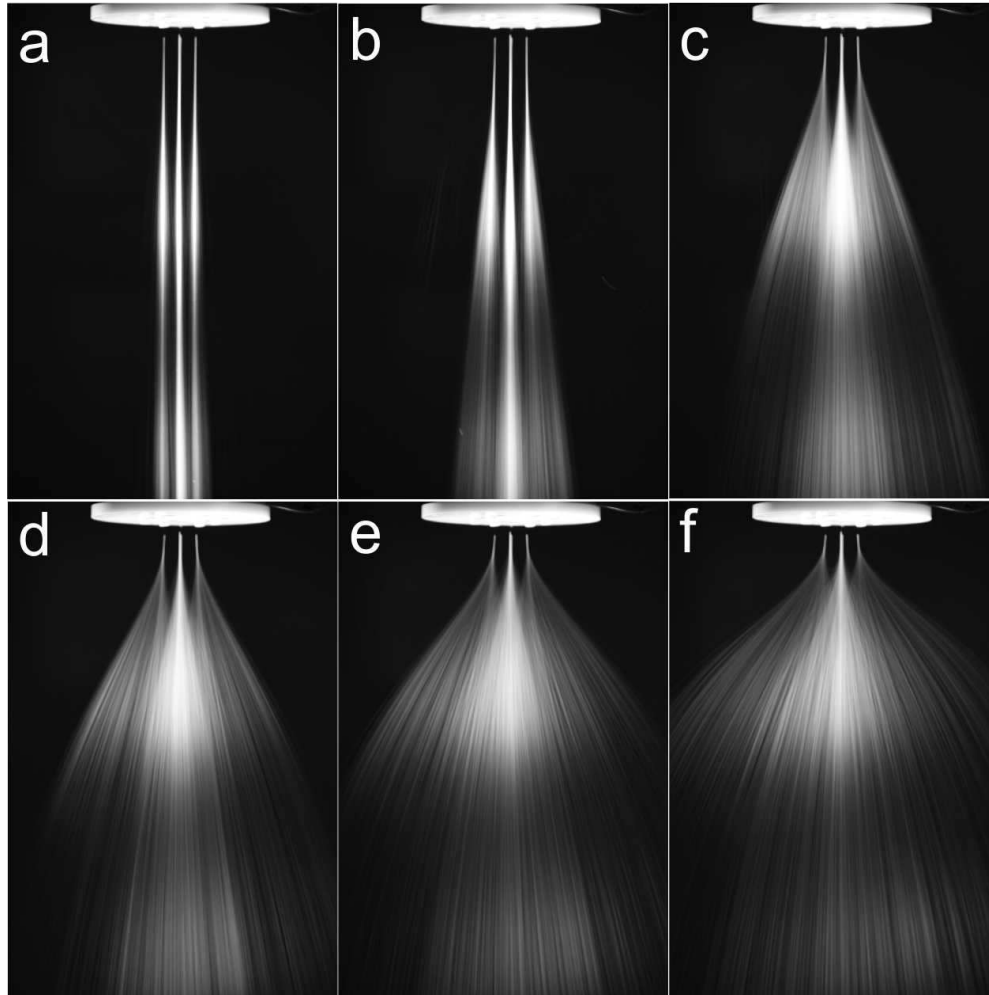


Figure 5.5 – Overview of the multinozzle spray. The flow was stabilized at $300 \text{ mL}\cdot\text{h}^{-1}\cdot\text{nozzle}^{-1}$ and the potential was increased from 0 (5.5a) to 7.5 kV (5.5f) in steps of 1.5 kV.

3.3 – Effect of the insulation layer

In some experiments performed without the insulation layer and with the application of an electric potential we observed that under these conditions some droplets, after being sprayed, were returning attracted by the charged rings. These droplets were eventually short circuiting the region between nozzle and ring and

high current peaks (some times sparks) could be detected which ultimately interrupted the functioning of the spray. The same problem happened much faster when the multinozzle device was coupled to an evaporation chamber. But in this case it was also due to the accumulation of condensed water vapor in the region between nozzle and ring.

To verify whether the presence of the insulation layer could guarantee a stable operation of the multinozzle system under the mentioned conditions we ran the electrospray inside an evaporation chamber for 13 hours with a flow rate of $360 \text{ mL}\cdot\text{h}^{-1}\cdot\text{nozzle}^{-1}$ and a potential difference of 7 kV.

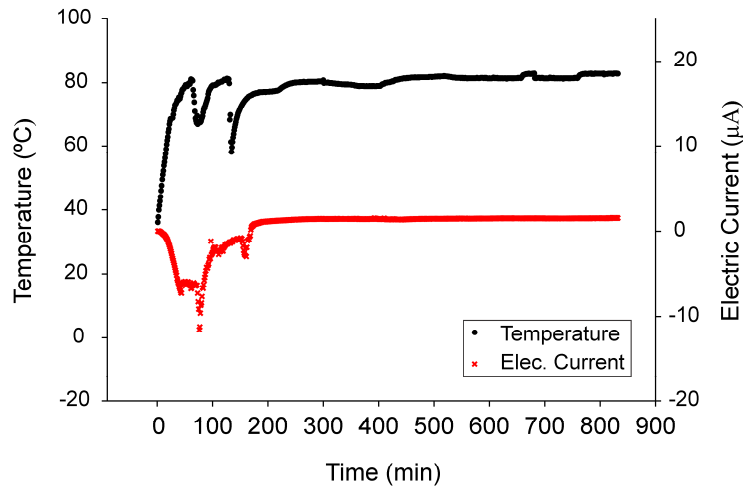


Figure 5.6 – Plot of electric current and liquid influent temperature against time.

Figure 5.6 shows that the presence of the insulation layer effectively avoids high oscillations of the electric current during the operation of the spray. The oscillation of the electric current observed during the first 200 minutes (red curve) was most probably due to the unstable temperature of the liquid influent during the same time interval (black curve). After this period the electric current stabilized around $\sim 2\mu\text{A}$. Other experiments were performed for different flow rates (300 and $420 \text{ mL}\cdot\text{h}^{-1}\cdot\text{nozzle}^{-1}$) and electrical potentials (3 and 5 kV); and similar results were obtained.

4. Conclusions

We present a novel multinozzle spraying device having 4 nozzles placed in a circular array around a central nozzle electro spraying in the simple-jet mode. Electro spraying in this mode with only 5 nozzles has provided throughputs of $2.2 \text{ L}\cdot\text{h}^{-1}$ with rather low packing density¹². Additionally, the presence of an insulation layer between nozzle tips and counter electrodes allowed a stable operation of the device under high relative humidity levels. Droplet size and jet breakup length measurements proved that all nozzles are operating at very similar conditions. Long distance images showed that the electric potential causes a significant dispersion of the droplets. Results indicate that such configuration can be a good option for processes which require high throughput, droplets with diameter in the sub-millimeter range and aim at the evaporation of the influent after atomization.

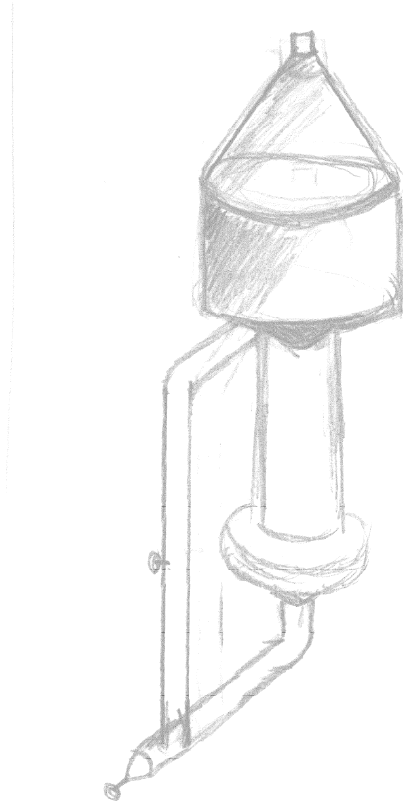
6. References

1. M. Cloupeau and B. Prunet-Foch, *Journal of Aerosol Science* **25** (6), 1021-1036 (1994).
2. J. M. Grace and J. C. M. Marijnissen, *Journal of Aerosol Science* **25** (6), 1005-1019 (1994).
3. N. Ashgriz, *Handbook of Atomization and Sprays*. (Springer, New York, NY, 2011).
4. Y. Arnanthigo, J. C. M. Marijnissen, C. U. Yurteri, G. Biskos and A. Schmidt-Ott, *Powder Technology* (2011).
5. A. Jaworek and A. Krupa, *Journal of Aerosol Science* **30** (7), 975 (1999).
6. M. Cloupeau and B. Prunet-Foch, *Journal of Electrostatics* **25** (2), 165-184 (1990).
7. J. Zeleny, *Physical Review* **10** (1), 1 (1917).
8. L. L. F. Agostinho, J. Wartena, E. C. Fuchs, C. U. Yurteri and J. C. M. Marijnissen, presented at the European Aerosol Conference, Manchester, UK, 2011.
9. C. Clanet and J. C. Lasheras, *Journal of Fluid Mechanics* **383**, 307-326 (1999).
10. B. Ambravaneswaran, H. J. Subramani, S. D. Phillips and O. A. Basaran, *Physical Review Letters* **93** (3), 034501 (2004).
11. B. Ambravaneswaran, S. D. Phillips and O. A. Basaran, *Physical Review Letters* **85** (25), 5332-5335 (2000).
12. W. Deng, C. M. Waits, B. Morgan and A. Gomez, *Journal of Aerosol Science* **40** (10), 907-918 (2009).
13. K. B. Geerse, Delft University of Technology, 2003.
14. C. U. Yurteri, R. P. A. Hartman and J. C. M. Marijnissen, *KONA Powder and Particle Journal* **28**, 24 (2010).
15. R. Bocanegra, D. Galán, M. Márquez, I. G. Loscertales and A. Barrero, *Journal of Aerosol Science* **36** (12), 1387-1399 (2005).
16. J. Wartena, *Analysis and Optimization of Evaporation in Electrospray Desalination*, Master thesis, TU Delft, 2011.
17. L. L. F. Agostinho, C. U. Yurteri, J. C. M. Marijnissen, S. Brouwer and G. Taminga, *Physics Review E*, **86**, 066317 (2012).
18. L. L. F. Agostinho, C. U. Yurteri, E. Fuchs and J. C. M. Marijnissen, *Applied Physics Letters* **100** (24), 4 (2012).
19. J. Eggers and E. Villermaux, *Reports on Progress in Physics* **71** (3), 036601 (2008).

20. S. P. Lin, *Breakup of Liquid Sheets and Jets*. (2010).
21. R. T. Collins, M. T. Harris and O. A. Basaran, *Journal of Fluid Mechanics* **588**, 75-129 (2007).

Chapter 6

Single-effect evaporator⁴



Drawing by Caio Newton Abreu Agostinho

⁴ This paper is based on the publication:

Agostinho, L.L.F., A. Kamau, S. Brouwer, C.U. Yurteri, E.C. Fuchs, and J.C.M. Marijnissen, *Application of a multinozzle electrohydrodynamic atomizer to enhance evaporation in a single-effect evaporator*. Submitted to *Desalination*, 2012.

1. Introduction

Desalination technologies are increasingly becoming a reliable approach for producing freshwater ¹. It accounts nowadays to a biggest part of the total fresh water production ²⁻⁴. The processes can be mainly categorized as thermal or membrane processes of which Multi-Stage Flash (MSF) and Reverse Osmosis (RO) are respectively the most explored of each category ^{5,6}.

In thermal desalination, freshwater is produced by different methods of evaporation of brackish or saline water. For instance, in Multiple Effect Distillation (MED), the feed is sprayed onto the surface of hot tubes and forms a thin film where evaporation takes place ^{7,8}. For MSF, seawater is evaporated by reducing the pressure in the flashing chamber/stage ⁹.

Some developments have been done in order to optimize the performance of the thermal processes. Some examples are the implementation of hybrid processes ^{10,11}, the application of renewable energy ¹² and the study and application of new materials ⁶. Particularly for MED units, new trends are the optimization of the systems by decreasing the top brine temperature ⁶ and for MSF, the process efficiency was improved by spraying the influent inside the evaporation chamber and enhancing turbulence in the low temperature stage ¹³.

An increasingly explored topic for thermal processes where a spraying system is involved is the proper selection of the spraying method, i.e. liquid atomization, and its influence on the dynamics of the spray evaporation. Some of these studies are mentioned below.

Jingwei *et al.* ¹⁴ have shown that a careful selection of the atomization method in thermal desalination can produce recovery rates as high as 90%. Osamu Miyatake ¹⁵ conducted experiments on spray flash evaporation and showed that the efficiency is enhanced when a superheated liquid was ejected through nozzles into a decompressed chamber. Kalogirou ¹⁶ designed a low cost spray evaporator that incorporates fewer heat exchange areas by spraying seawater into droplets finer than normally found in desalination processes. Lastly, a technology called Rapid Spray EvaporationTM (RSE) ejects the feed through nozzles at high velocities whereby evaporation is determined by the size and the velocity of the droplets ¹⁷.

The disintegration of a liquid into droplets can happen by various means. The most applied mechanisms are pressure¹⁸, ultrasonic oscillations¹⁹ and centrifugal forces¹⁹. Normally these methods produce polydisperse sprays and don't offer a good control regarding the size distribution and/or the dispersion of the droplets. However it is known that for evaporation methods small, well dispersed and monosized droplets are desirable²⁰. Thus, a method which could provide small droplets, narrow size distribution and a good droplet dispersion inside the chamber would certainly enhance evaporation.

A process which can achieve this is electrohydrodynamic atomization (EHDA), also known as electrospraying. EHDA produces charged droplets formed from the breakup of a liquid in the presence of a strong electric field²¹⁻²⁴. When applied in the so called cone-jet mode this process is known by its fine control over the generated droplets size and the production of monodispersed sprays²⁵. It is commonly used in applications that require nanometer to micrometer-sized droplets like mass spectrometry²⁶, production of thin films²⁷ and drug inhalation²⁸. A known draw back of EHDA in this mode is the fact that it operates at very low flow rates. Focusing on this problem, Agostinho et al²⁹ recently published that electrospraying in another mode, i.e. the simple-jet mode, is a good option for systems which require a high throughput and charged droplets in the sub-millimeter range. Additionally, the authors have shown that this mode also allows droplet size control and creates good dispersion, making it a very good option for some evaporation-distillation processes³⁰. Aiming on even higher throughputs, the same authors have published another work³¹ reporting a novel multi nozzle device for electrospraying in the simple-jet mode. The proposed design was able to produce droplets with the same average size for all nozzles and to operate inside chambers with a high relative humidity level (95%).

In this paper we report on the usage of an electrohydrodynamic multinozzle atomizer in a single step evaporation chamber. The main objective is to evaluate whether such atomizers can enhance the spray evaporation and decrease the overall energy consumption in thermal desalination and related processes. The relation between the applied electric potential (Φ) and the spray evaporation was studied. The influences of other operating conditions like the application of forced convection (injected dry air in a counter flow) and the

influent temperature were also explored.

2. Experimental method

For the spray evaporation experiments we coupled an EHDA multi-nozzle device to a single-effect evaporator. A general scheme of the device is shown in Figure 6.1.

The device is composed of two chambers, chamber A and B. Chamber A is the multi-nozzle atomizer and the preheating chamber and chamber B is the evaporation chamber.

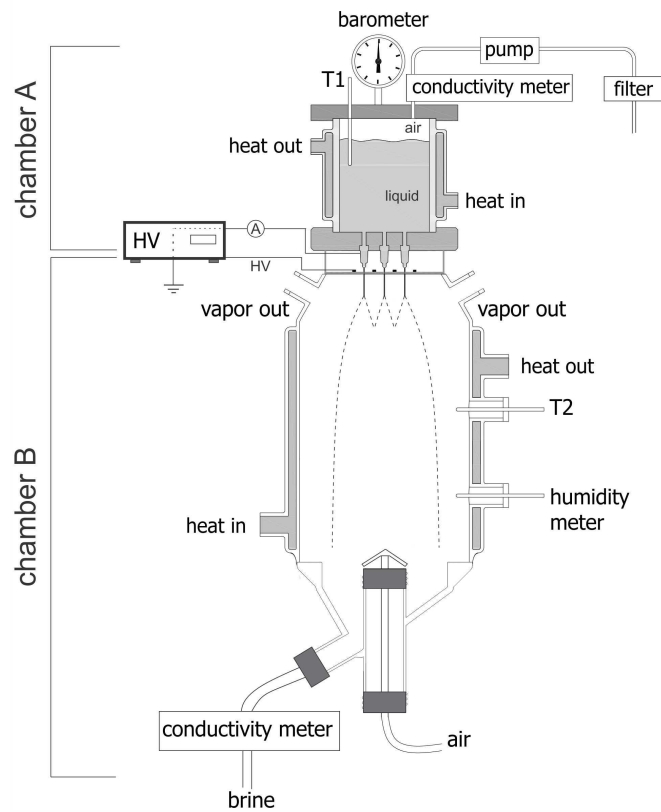


Figure 6.1 - Complete multi-nozzle EHD atomizer coupled with single-effect evaporator with chamber A and B (not in scale). Thermal baths for pre-heating oil and for the jacket are not shown in the diagram.

The multinozzle device and pre-heating chamber are the same as used in a previous work³¹. It is composed of 4 nozzles placed around a central nozzle in a 36mm radius circle which gives a packing density of $2 \cdot 10^3$ nozzles per m^2 (figure 6.2). Each nozzle is isolated from the rings by a cylindrical chamber of radius $6.5 \cdot 10^{-3}$ m. The counter electrodes are copper rings positioned 1.7 cm above the nozzle tip and connected together. High voltage (FUG HCP 14-20000 DC) is applied to the rings while the liquid (and nozzles) is kept grounded. The nozzles are blunt ended, polished, stainless steel needles (FED Inc.) gauge number 22, 250 μm ID and 510 μm OD, uncoated. An insulating layer (circuit board FR-4) is placed between the rings and the nozzles to isolate the rings from the rest of the device to prevent transfer of charge to the evaporation chamber, i.e. possible current leakage which could electrify the interior of the reactor. To assure an uniform liquid flow through the nozzles and to decrease possible oscillations from the pump, an air gap was kept above the liquid/air interface inside the pre-heating chamber which gets pressurized (1.2-1.6 bar) due to the action of the pump. The liquid was pumped (SIMDOS® FEM 1.10 KT.18S model) from a tank and filtered with a carbon filter (BOSCH F4058) to prevent blockage of the nozzles. A temperature probe (PT100) indicated by T_1 is used to measure the initial temperature of the inlet before electrospaying.

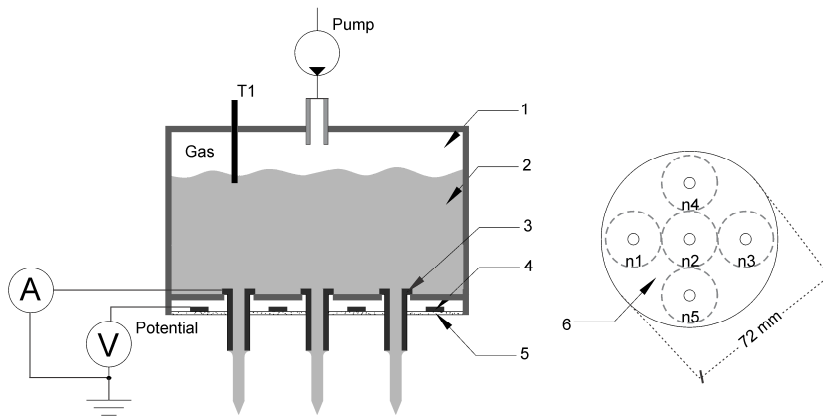


Figure 6.2 - Schematic diagram of chamber A (not in scale). The chamber is made out of glass and polypropylene (PP). The specified parts are: Gas column (1), salt solution (2), nozzles (3), cooper rings (4), insulation layer (5). The nozzles and rings are organized in a circular pattern (6)³².

Chamber B (figure 6.1) was made of glass (h = 30cm and D = 10 cm) to allow visualization of the spray. Previous experiments allowed us to measure the diameter of the spray at the highest used potential (4 kV) and the diameter of the chamber was made to be greater than that to avoid the droplets from contacting the wall (see also Agostinho *et al*³¹ about the dispersion of the electrospayed droplets at different applied potentials). A PT100 temperature probe (shown as T₂) was used to measure the temperature inside the chamber and a humidity meter (Michel MDM25) was used to measure the relative humidity. A heating jacket was used to provide a constant temperature of the evaporation chamber wall (chamber B) throughout the experiments (25°C). Dry air was introduced from below counter-currently with the spray using a T-shaped air diffuser to provide forced convection and its flow rate could be adjusted and measured with a flow meter (KOBOLD KFR-2218NO). The electrical conductivities and temperatures of the influent and brine were measured using a SMARTEC–T CLD 633 conductivity meter. All the mentioned sensors were connected to a Data logger (ENDRESS-HAUSSER RSG30) which allowed online determination of the parameters. In all the experiments, the condensate was blown out and the brine was collected.

The liquid used for the experiments was a solution of deionized water with NaCl of concentration 35g/L to simulate sea water. Some of its physical properties are shown in table 6.1.

Table 6.1: Physical properties of NaCl with concentration of 35g/l.

Liquid	μ [Pa·s]	Ξ [kg·m ⁻³]	Ξ_r	K [S·m ⁻¹]	Ξ [N·m ⁻²]
NaCl aq.	$9.21 \cdot 10^{-4}$	$1.05 \cdot 10^3$	$7.35 \cdot 10^1$	$4.5 \cdot 10^0$	$7.37 \cdot 10^{-2}$

In all experiments the liquid was pre-heated before electrospaying. Four different flow rates were used in the experiments 240, 300, 360 and 420 mL·h⁻¹·nozzle⁻¹. The potential difference was varied from 0 to 4 kV (for each flow rate) following the data reported by Wartena³³ who reported that, for single nozzle electrospays operating in the simple-jet mode, the maximum evaporation rate was reached at ~4 kV for similar flows. The author performed experiments in open air and with a closed chamber similar to chamber B.

For each combination of flow and potential, the evaporation was measured using a general mass balance, assuming steady-state conditions;

$$\% \text{ evaporated} = \frac{(m_i - m_b)}{m_i} \times 100\% \quad (6.1)$$

Where m_i is the inflow mass flow rate ($\text{kg}\cdot\text{h}^{-1}$), m_b is the mass flow rate of the brine ($\text{kg}\cdot\text{h}^{-1}$).

The influence of forced convection on the evaporation level was also studied. For that dry air was injected at different flow rates (35, 45, 75 and 85 L/min) for the different flow rates and electric potentials. Lastly we also studied the influence of the spray initial temperature (60 and 80°C) on the evaporation rate at different applied potentials. The spray electric current was measured continuously in all experiments with an electrometer (Fluke 8846A 6.5) connected between the ground and the nozzles to verify the stability of the spraying system during the experiments. All experiments were done in duplicate.

3. Results and discussion

Figure 6.3 shows online measurements of the inlet and brine electric conductivity during experiments with two flows rates (360 and $420 \text{ mL}\cdot\text{h}^{-1}\cdot\text{nozzle}^{-1}$) and the electrical potential varying from 0 until 3 kV. The applied potential was programmed to shift automatically. The observed increase of the brine electrical conductivity for higher electrical potentials, while the inlet conductivity remains constant, is an indication that the electrical potential enhances spray evaporation. The picture also shows that higher flow rates decrease the influence of the electric potential on the evaporation rate. This is expected as higher flow rates generally reduce droplets dispersion and increase droplet diameters as reported in previous works^{29, 30}.

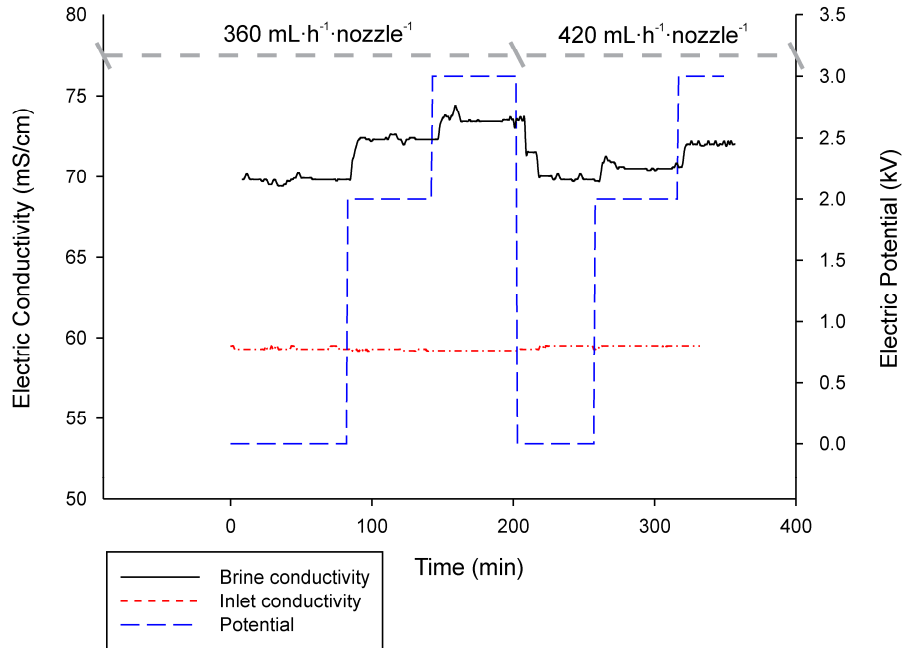


Figure 6.3 - Online measurements of the brine conductivity (solid line) and inlet conductivity (small dashed line) for different potentials (long dashed line) and two different flow rates. In this experiments $T_1 = 80^{\circ}\text{C}$, $T_2 = 25^{\circ}\text{C}$ and dry air counter flow $75 \text{ L}\cdot\text{min}^{-1}$

To check for possible current leakages or sparking the electric current was monitored online in all experiments. Additionally, some extra experiments were performed with different combinations of potentials and flow rates for a 72 hours uninterrupted operation period. In all situations the reactor performed stable until 4kV.

To quantify the influence of the electric potential on enhancing the spray evaporation we performed some experiments with four different flow rates. For each the potential was varied from 0 until 4 kV. The liquid inlet temperature was fixed at $\sim 80^{\circ}\text{C}$ and dry air was injected in a counter flow to provide relative humidity inside the reactor $\sim 95\%$ ($45 \text{ L}_{\text{dair}}\cdot\text{min}^{-1}$). The results of these experiments are shown in figure 6.4.

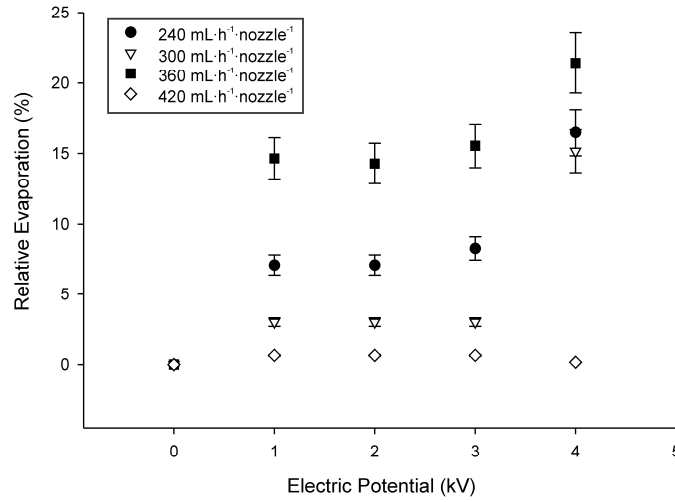


Figure 6.4 - Relative evaporation at different potentials (0 to 4kV) for different flow rates (240, 300, 360 and 420 mL·h⁻¹·nozzle⁻¹). Spray temperature (T₁) was fixed at ~80°C, dry air was inject in a counter flow at 45 L·min⁻¹ and reactor jacket temperature was kept at 25°C (T₂). Each data point represents the average of the two measurements with the error bar representing the minimum and maximum measured values.

In this figure the shown *relative evaporation* (RE_{xkV}) is the ratio between the evaporation of the spray at a certain potential (E_{xkV}) and its value for $\Phi = 0$ kV (E_{0kV}) and it is expressed as a percentage as follows,

$$RE_{xkV} = \left(\frac{E_{xkV}}{E_{0kV}} - 1 \right) \cdot 100\% \quad (6.2)$$

In general, for the conditions of the experiments, the evaporation of the uncharged spray was between 6 and 7% of the total atomized volume.

From the plot it is seen that the application of the electric potential enhances the spray evaporation compared to the uncharged situation up to 22% (~ 8.5% of the total atomized volume). The best results were obtained with a flow rate of 360 mL·h⁻¹·nozzle⁻¹ and a potential difference of 4 kV. Wartena³³ has also reported this flow rate as the one which presented the best performance when

investigating the same relation with single nozzle electrospays in the simple-jet mode. We observed that for this flow rate the spray is already rather monodisperse without the application of the electric field (see also Agostinho *et al*³⁰). The good results found when an electric field is applied are probably a consequence of the enhanced dispersion and smaller droplets.

Regarding $240 \text{ mL}\cdot\text{h}^{-1}\cdot\text{nozzle}^{-1}$ it is important to mention that the level of evaporation for the uncharged situation ($\Phi = 0$) at this flow rate was the lowest measured (5.8%). However, after subjected to the application of the electric potential, it increased to levels similar to those found for 300 and $360 \text{ mL}\cdot\text{h}^{-1}\cdot\text{nozzle}^{-1}$ ($\sim 8.5\%$). This can be explained because the influence of the electrical potential on reducing the droplet size for this flow rate is much more pronounced than for the others, i.e. it can reduce the average main droplet size up to 50% ³⁰. Additionally, it has been proved that droplet dispersion for this flow rate is more pronounced at the same potential level than for the other investigated flow rates²⁹.

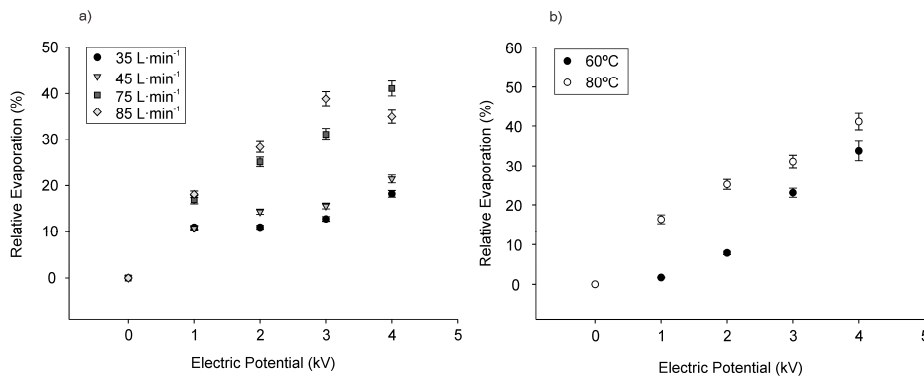


Figure 6.5 – Influence of different flow rates of the injected dry air with the liquid pre-heated to 80°C (6.5a) and influence of the different spray initial temperature (6.5b) on the spray relative evaporation. Both experiments were done for $360 \text{ mL}\cdot\text{h}^{-1}\cdot\text{nozzle}^{-1}$. The experiments presented in figure 5b were done for a constant air flow rate of $75 \text{ L}\cdot\text{min}^{-1}$. Each data point represents the average of the two measurements with the error bar representing the minimum and maximum measured values.

For $300 \text{ mL}\cdot\text{h}^{-1}\cdot\text{nozzle}^{-1}$ the situation is very similar to $240 \text{ mL}\cdot\text{h}^{-1}\cdot\text{nozzle}^{-1}$ but the evaporation level for the initial potentials (1 until 3kV) was lower. This can be explained because for these electric potentials the sprays produce droplets with similar diameter but the higher inertia of the droplets at $300 \text{ mL}\cdot\text{h}^{-1}\cdot\text{nozzle}^{-1}$ decreases their dispersion inside the chamber³⁰.

The low values found for $420 \text{ mL}\cdot\text{h}^{-1}\cdot\text{nozzle}^{-1}$ are probably a combined effect of the higher inertia of the droplets and the presence of satellite droplets³⁰.

The influence of the spray initial temperature and different forced convection flow rates were also evaluated. For these experiments the liquid flow rate was kept at $360 \text{ mL}\cdot\text{h}^{-1}\cdot\text{nozzle}^{-1}$ while the potential varied from 0 until 4kV. The sequences were done for two different initial temperatures of the spray (60 and 80°C) and four different air flows (35, 45, 75, $85 \text{ L}\cdot\text{min}^{-1}$). The results are shown in figure 6.5.

Figure 6.5a shows the influence of the injected dry air flow rate on the evaporation level. This injection influences the evaporation level because it reduces the relative humidity inside the chamber by enhancing the convection of the generated vapor. Additionally the droplets residence time, i.e. time inside the reactor, is increased. For a constant air flow, this influence increases with the electric potential. This can be related to the fact that higher potentials create a broader dispersion of the spray, i.e. bigger droplet to droplet distances, favoring the removal of the produced vapor around the droplets liquid air interface.

For $75 \text{ L}\cdot\text{min}^{-1}$ and 4 kV the relative evaporation was $\sim 40\%$ higher than obtained for the uncharged situation ($\sim 10\%$ of the total atomized volume). The relative humidity inside the chamber for the same air flow was $\sim 16\%$, whereas for $35 \text{ L}\cdot\text{min}^{-1}$ it reached up to 90%.

For the highest air flow ($85 \text{ L}\cdot\text{min}^{-1}$) it was observed that the relative evaporation is reduced when the potential reaches 4 kV. This phenomenon needs more investigation.

When applying the flow rate which presented the best results ($75 \text{ L}\cdot\text{min}^{-1}$) and experimenting with different spray initial temperatures (60 and 80°C) it is seen, as expected, that the evaporation ratio is higher for the higher temperature

(figure 6.5b).

To have an idea about the energy performance of the proposed device we calculated its droplet generation efficiency.

The theoretical energy required to generate droplets from a liquid, can be estimated by the energy needed to create the surface of the droplets, i.e. the product of droplet surface area and surface tension (eq. 6.3)³⁴.

$$E = \sigma \cdot \pi \cdot D^2 \quad (6.3)$$

Where D is the droplet average diameter and σ is the surface tension of the liquid. In the above estimation the energy needed to overcome viscous forces during liquid breakup is neglected. Doing this for aqueous solutions as opposed to e.g. oils, is a valid assumption³⁴.

With high speed imaging we could estimate the number of droplets (N) generated in a certain time interval and measure their individual diameters. For each droplet the above mentioned equation was applied and the system “theoretical energy input” was calculated as follows:

$$E_T = \sum_{i=1}^N E_i \quad (6.4)$$

Using the spray current and the electric potential difference for the same time interval needed to produce the N droplets we calculated the electrical energy input of the system (E_E). From the pressure difference inside chamber A, the flow rate and the pump efficiency we estimated the energy input for the pumping system for the same time interval (E_P). We then considered the atomizer “actual energy input” as:

$$E_A = E_E + E_P \quad (6.5)$$

Thus, the theoretical energy efficiency of our atomization method was calculated as:

$$\eta = \frac{E_T}{E_A} \quad (6.6)$$

In general such efficiency is very small because only a very small part of the input energy is converted into surface energy to generate the droplets. A large percentage is converted into kinetic energy and heat.

From the above mentioned values we determined that the droplet efficiency energy of our systems is, in average, $\sim 0.43\%$ while a typical efficiency for swirl atomizers running with water ($\Delta P = 10$ MPa driving force) is $\sim 0.22\%$ ³⁴. Another author has mentioned that for old traditionally used atomizers the efficiency is very small, namely $< 0.1\%$ ³⁵.

Regarding scaling problems we could observe that the nozzles remained operational after more than 72 hours of continuous running. After long term experiments some salt crystals were observed at approximately 1cm above the nozzle tip and were possibly formed due to evaporation of counter charged droplets attracted by the nozzle surface. This phenomenon has been previously mentioned by Agostinho *et al* for studies with the intermittent cone-jet mode³⁶. Further studies with real sea water are needed to better quantify and understand scaling problems. Additionally, nozzle based systems naturally require good pre-treatment to remove suspended solids and avoid clogging. In this case, considering the nozzle inner diameter, microfiltration systems can be a good option.

4. Conclusions

The results have shown that a multinozzle electrohydrodynamic atomization device operating in the simple-jet mode enhances spray evaporation up to 40% when compared to the uncharged situation. Droplet efficiency energy was calculated as $\sim 0.43\%$ which is two times more than calculated for swirl atomizers. Such systems can be applied if a high throughput is required with droplets in the sub-millimeter range. Additionally, the produced droplets are electrically charged and can be manipulated to collide with heated surfaces. From the results it can be inferred that such systems might be a good option for processes like thermal desalination and spray drying.

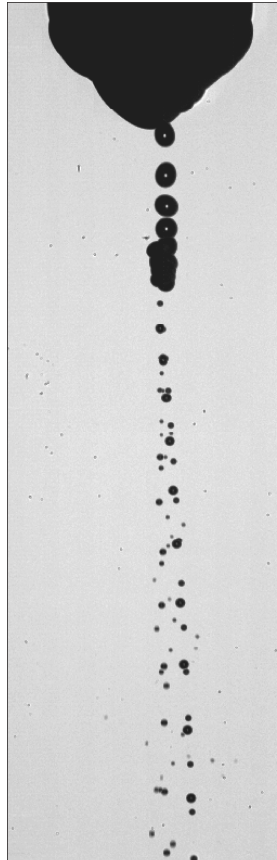
6. References

1. A. M. K. El-Ghonemy, *Renewable and Sustainable Energy Reviews* **16**, 1537-1556 (2012).
2. J. M. Miller, 2003.
3. I. D. A. IDA, 2006.
4. G. M. Andrea Cipollina, Lucio Rizzuti, *Sewater Desalination*, 01 ed. (Springer, Palermo, 2009).
5. E. D. F. Macedonio, A.A. Gusev, A. Bardow, R. Semiat, M. Kurihara, *Chemical Engineering and Processing* **51**, 2-17 (2012).
6. I. K. K. Akili D. Khawaji, Jong-Mihn Wie, *Desalination* **221**, 47-69 (2008).
7. R. M. K. Bourouni, L. Tadrict, and H. Tadrict, *Desalination* **116**, 165-184 (1998).
8. A. Al-Radif, *Desalination* **93**, 119-125 (1993).
9. R. Semiat, *Water International* **25**, 54 - 65. (2000).
10. N. D. Abdullah Alkhudhiri, Nidal Hilal, *Desalination* **287**, 2-18 (2012).
11. C. Charcosset, *Desalination* **245**, 214-231 (2009).
12. N. N. Veera Gnaneswar Gude , Shuguang Deng *Renewable and Sustainable Energy Reviews* **14**, 2641–2654 (2010).
13. K. Z. A.-. Subaie, *Desalination* **206**, 29-35 (2007).
14. H. C. Jingwei Hou, Duo Wang, Xueli Gao, Congjie Gao, *Desalination* **258**, 5–11 (2010).
15. O. Miyatake, *Desalination* **96**, 163-171 (1994).
16. S. A. Kalogirou, *Progress in Energy and Combustion Science* **31**, 242–281 (2005).
17. M. Svensson, (2005).
18. J. R. P. P. Maniarasan, M.T. Nicholas, *Desalination* **235**, 139–145 (2009).
19. W. A. Siringano, *Fluid dynamics and transport of droplets and sprays*, 2nd ed. (Cambridge University Press, 2010).
20. F. A. Williams, *The Physics of Fluids* **1** (6), 541-545 (1958).
21. J. C. M. M. J. M. Grace, *Journal of Aerosol Science* **25** (6), 1005-1019 (1994).
22. C. U. Y. Y. Annanthigo, G. Biskos, J.C.M. Marijnissen, A. Schmidt-Ott, *Powder Technology* **214**, 382-387 (2011).
23. M. P. Bhupendra G. Prajapati, *International Journal of Pharmaceutical Sciences Review and Research* **1** (1), 11-13 (2010).
24. B. P-F. Michel Cloupeau, *Journal of Aerosol Science* **25** (6), 10221-11036 (1994).

25. J. D. a. A. B. A. M. Gañan-Calvo, *Journal of Aerosol Science* **28** (2), 249-275 (1997).
26. J. Thunig, L. Flø, S. Pedersen-Bjergaard, S. H. Hansen and C. Janfelt, *Rapid Communications in Mass Spectrometry* **26** (2), 133-140 (2012).
27. L. M. O. Wlihelm, S.E. Pratsinis, *Journal of Aerosol Science* (34), 815-836 (2003).
28. J. Marijnissen, *J. of Aerosol Science* **35** (Supplement 1), 3-4 (2004).
29. L. L. F. Agostinho, C. U. Yurteri, J. C. M. Marijnissen, S. Brouwer and G. Taminga, *Physics Review E*, **86**, 066317 (2012).
30. L. L. F. Agostinho, C. U. Yurteri, E. Fuchs and J. C. M. Marijnissen, *Applied Physics Letters* **100** (24), 4 (2012).
31. L. L. F. Agostinho, S. Brouwer, C. U. Yurteri, E. C. Fuchs and J. C. M. Marijnissen, *Applied Physics Letters* (2012).
32. S. P. Brouwer, Master thesis, Delft University of Technology, 2011.
33. J. Wartena, TU Delft, 2011.
34. H. Liu, *Science and EGINEERING of Droplets*. (William Andrew, New York, 1981).
35. L. Bayvel and Z. Orzechowski, *Liquid Atomization*. (1993).
36. L. L. F. Agostinho, E. C. Fuchs, S. J. Metz, C. U. Yurteri and J. C. M. Marijnissen, *Phys. Rev. E* **84** (2), 026317 (2011).

Chapter 7

*Bouncing droplets and clouds*⁵



Picture by Luewton L. F. Agostinho

⁵ This paper is based on the publication:
Agostinho, L.L.F., E.C. Fuchs, S.J. Metz, C.U. Yurteri, and J.C.M. Marijnissen, *Reverse movement and coalescence of water microdroplets in electrohydrodynamic atomization*. Physical Review E, 2011. **84**(2): p. 026317.

1. Introduction

Electrohydrodynamic atomization (EHDA), or simply Electrospray, is a physical process that concerns the disruption of a liquid into a spray of charged droplets when it is subjected to an intense electric field (EF). The history of electrospray research dates back to the late sixteenth century when William Gilbert discovered that in the presence of a charged piece of amber, a drop of water deformed into a cone¹. Almost 300 years later Lord Rayleigh estimated the maximum amount of charge a liquid droplet could carry^{2, 3} based upon equilibrium between electrostatic repulsion and surface tension, the so called "Rayleigh limit". In the early 20th century, Zeleny published two important works about electrified liquid surfaces^{4, 5}, and in the 1960's, Taylor paved the way for modern Electrohydrodynamics (EHD)⁶. Examples of EHD based technologies include electrospray-ionization mass spectroscopy (ESI-MS)⁷ and the production of particles for medical and agricultural purposes⁸⁻¹⁰. A good overview of the field is given in the book by Bailey¹¹, in the review by Grace & Marijnissen¹² and in the work of Eggers and Villermaux¹³. The different kinds of electrosprays generated under different conditions are classified as "spray modes". The classification and characteristics of the different modes in EHDA is a topic extensively explored by many authors^{12, 14-18}. Based on the reported classifications, we could identify that the phenomenon reported in this work was observed in a regime between the dripping and the cone-jet mode, which can be called as pulsating jet mode¹². The mode is sometimes differentiated into spindle mode and intermittent cone-jet mode^{12, 15}. We will not go into further details and we will refer to our spray as operating in a "pulsating jet" mode throughout the text.

The recent advances done in the EHDA field are not only important for the development of the above mentioned technologies but also because it triggers a whole new group of phenomena based on the interaction of liquids with strong electric fields. Among these phenomena one can mention the work of Fuchs *et al.*^{19, 20}, who rediscovered Armstrong's²¹ rope of water and published a series of papers about this "floating water bridge", the influences of EF on liquid/liquid coalescence²²⁻²⁷, the work of Ristenpart *et al.*²⁸ who has reported on the non-coalescence of oppositely charged droplets immersed in strong EF and the deformation of droplets immersed in strong electric fields^{29, 30}. The last three

examples are especially important for the good understanding of this paper; and therefore will be better explored in the following paragraphs.

The influences of an external EF on liquid/liquid coalescence was probably firstly reported by ²⁶ in 1961. They claimed that the application of strong electric fields increases the ratio of coalescence due to induced charge polarization. The same authors later also investigated coalescence of liquid droplets in electric and shear fields ²⁴. They observed that oppositely charged water droplets immersed in silicone oil repelled one another below a critical separation distance. The authors could not completely explain the phenomenon and have said simply, based on the observation of some images that the reason was probably an “electrical discharge” between the droplets.

Contrary to the assumption that EFs can enhance coalescence of droplets with opposite polarity, a recent report by Ristenpart *et al* ²⁸ showed that above a critical EF strength charge transfer can take place before coalescence happens, and the droplets, instead of coalesce, bounce off each other. After that, Bird *et al* ²⁵ investigated electrically driven coalescence and recoil of water droplets and claimed that the EF has an important role distorting droplet’s surface prior to contact, and also that the subsequent dynamics depend predominantly on capillary forces. Apart from the experiments done by Allan and Manson, the other authors investigated coalescence for very low droplet velocities (e.g. $v < 1 \text{ m}\cdot\text{s}^{-1}$) only. Allan and Manson took inertia into account but still could not explain the bouncing effect completely.

Regarding the stability of droplets in an EF it is known that these fields cause droplets to develop conical structures oriented along the direction of the field lines. Many authors investigated these effects both for charged and uncharged droplets ²⁹⁻³¹. Commonly referred to as *Taylor Cones* ⁶ these structures result from a balance of charge induced pressure from the applied EF and surface tension stresses resisting interfacial deformation ²⁵. In a situation where the physical characteristics of a droplet are constant (i.e. permittivity, surface tension and radius), the field is the critical factor to define whether the droplet will be stable or not. According to Grimm and Beauchamp ³⁰, for critical values of the field, an uncharged single droplet will develop two opposing conical tips aligned with it. If the droplet is charged, instead of adopting a prolate spheroidal shape, it

becomes distinctly tear-shaped.

A direct consequence of these instabilities is the spraying of charged progeny droplets from the formed Taylor cones. Grimm and Beauchamp³⁰ also investigated the formation of these sprays. The authors found that neutral droplets exhibited the same prolate elongation mentioned by Brazier-Smith²⁹ with symmetric “cone-jets” of positive and negative progeny droplets. Droplets with a net charge q take the form of asymmetric tear-shapes and emit a single charged jet. According to the authors, sometimes the total charge loss can be greater than the original droplet charge resulting in oppositely charged droplets. These instabilities, even apparently similar, can not be directly related to the so called droplet Rayleigh limit. Both phenomena assume droplet’s disruption as a consequence of an unbalance between the cohesive forces due to surface tension and the repulsive electrostatic forces. The last one is a consequence of droplet charge density, which surpasses a certain threshold, the Rayleigh limit. The first one, on the other hand, explains that the strong electric field induces charge migration (electrokinetic movements) inside the droplet leading to some deformations on its spherical shape like the ones predicted by³⁰. These deformations can, eventually, end up with droplet disruption. Consequently, the instabilities mentioned by²⁹⁻³¹ can be seen even when the droplet charge is way below its Rayleigh Limit.

Bird *et al*²⁵ suggested the nondimensional electrocapillary number $\varepsilon_c = \frac{\varepsilon \cdot \varepsilon_0 \cdot E^2 \cdot a}{\gamma}$, where $\varepsilon \cdot \varepsilon_0$ is the permittivity of the liquid, E is the magnitude of the electric field at droplet’s surface, a is the droplet radius and γ surface tension, to predict whether a droplet will deform or not when immersed in a certain electric field. The number represents the ratio between charge induced pressure from the applied electric field and surface tension stress resisting interfacial deformation²⁵. If this ratio is bigger than one, a liquid droplet will deform inside the field. In the same paper they found that if $\varepsilon_c > 1.44$ two oppositely charged water droplets failed to coalesce. The explanation for this is, according to them, that at higher values of ε_c the droplets became unstable prior to contact, causing electrospraying²⁵, and the electrospray will balance charges

causing the recoil. Due to these observations, they have concluded that electro spray may play an important role in the recoil of charged droplets.

In this study, we report the unexpected observation of a reverse movement of EHDA produced water droplets back to the nozzle from which they were ejected. The phenomenon was observed in the pulsating jet mode. Considering that the returning of a sprayed droplet normally leads to contact between this droplet and the liquid meniscus, it is believed that this phenomenon can be used to better understand charged liquid-liquid coalescence and its implications. The importance of investigating the coalescence between droplet and meniscus under this specific situation is that, in addition to what has been reported in the literature, with EHDA we are able to verify whether droplet inertia also plays an important role in this situation or not.

2. Experimental

2.1 Electro spray configuration

Electrospraying of water was studied using a capillary-plate configuration with variable nozzle to plate distances, i.e. between 2 cm and 4 cm (see Fig. 7.1). A blunt ended, polished, stainless steel needle (FED Inc.) was used as a nozzle (gauge number 22, 410 μm ID and 710 μm OD, uncoated). A syringe pump type SP-12S PRO AITEC was used to deliver the liquid to the nozzle. The flow rate was also variable, but generally established around 2 $\text{mL}\cdot\text{h}^{-1}$. High voltage was applied with a FUG HCP 35-35000 DC high voltage power supply. In some experiments the counter electrode (steel plate 4x4 cm^2) was subjected to a high voltage (negative) with the nozzle grounded, in other experiments the nozzle was subjected to a high voltage (positive) with the counter electrode grounded. Configurations were always defined in order to allow the formation of positive droplets in the pulsating jet mode^{12, 15, 32-35}. The liquid used was deionized water ($\sim 18 \text{ M}\Omega\cdot\text{cm}$, Millipore). When required, simulations were done with the electrostatics module of Comsol® Multi Physics software bundle. In some cases the spray currents were measured using a 1 $\text{M}\Omega$ resistor (5% tolerance), which was placed between the ground and the nozzle (with the potential applied on the counter electrode). To synchronize

the electric current signal with the recorded movies a CONTEC (16 channels) data acquisition board and a RIGOL oscilloscope DS1022C (not represented in fig. 7.1) were used.

2.2 Optical system

An optical system consisting of a high speed (HS) camera (Photron SA-1) and diffused backlight illumination (Microscope light source Karl Storz Technolight 270 with liquid light guide and diffuser) was used to record the experiments (see Fig. 7.1). ImageJ[®] was used for image processing; brightness and contrast corrections were done using Corel Photopaint[®] 15. All experiments were performed under ambient conditions at a temperature of $\sim 23^{\circ}\text{C}$ and $\sim 55\%$ relative humidity.

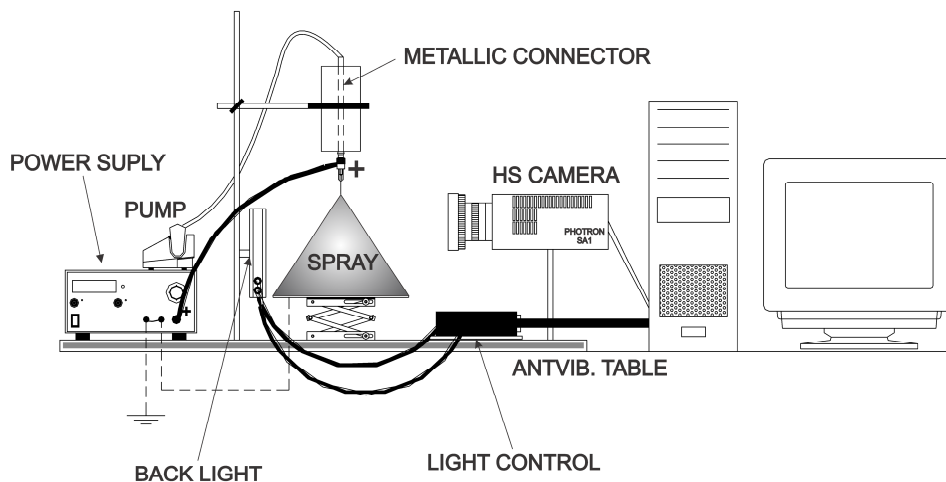


Figure 7.1 - Electro spray and optical system scheme.

3. Results and Discussion

3.1 Electro spray characteristics, droplet charge and velocity

Under the experimental conditions different electro spray (ES) modes were observed using a constant flow rate while increasing the applied voltage. Due to the high surface tension of water it was not possible to reach a stable cone-jet mode. Therefore, the experiments were done in the pulsating jet mode.

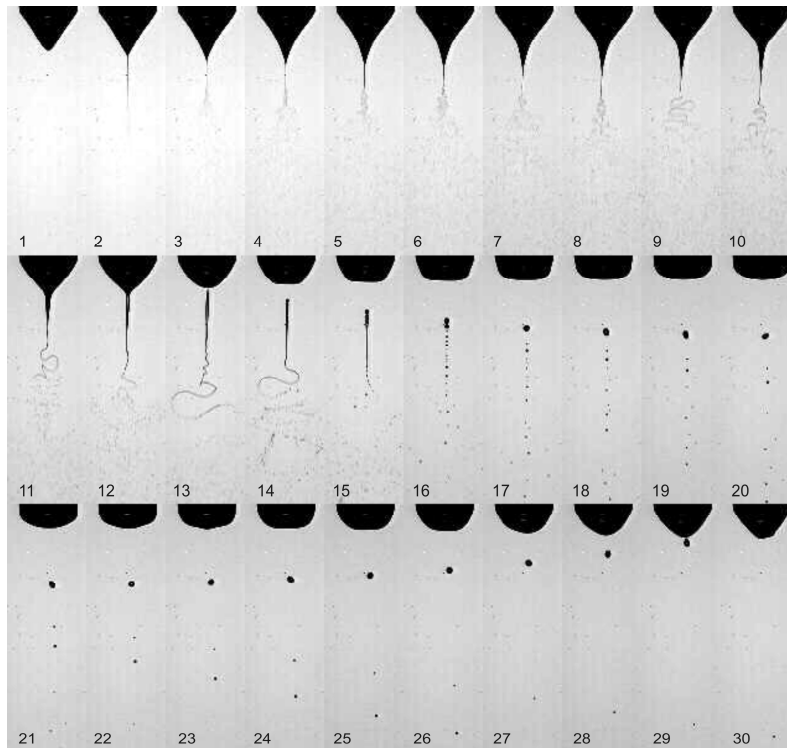


Figure 7.2 - Category C1 (complete coalescence) – a droplet returns to the cone after being formed from a liquid ligament. The diameter of the returning droplet is $\sim 80 \mu\text{m}$, time frame between images is $\sim 45 \mu\text{s}$, applied potential is -5.67 kV on the counter electrode and used flow rate is $1 \text{ mL}\cdot\text{h}^{-1}$.

The basis of this classification is already addressed in the introduction. In the pulsating jet mode we observed some unexpected phenomena which will be described in this paper divided in three different categories. We saw some droplets returning (bouncing) to the meniscus and being completely re-integrated to it. This category will be named as returning followed by “complete coalescence” or category C1.

Fig. 7.2 shows an example of the situation. The sequence starts with the meniscus assuming a conical shape (frame 1) from which a jet emerges and is atomized into fine droplets (frames 2-9). The jet starts to elongate and a liquid ligament is formed (frames 10-12). This ligament is then detached from the meniscus (frame 13) and subsequently breaks-up into droplets bigger than the previous ones (frames 14-16). These droplets descend due to gravity and electric forces (frames 17-20), but the uppermost droplet reverses its path (frames 21 - 28) and collides with the meniscus (frame 29) where they coalesce (frame 30).

When considering the physical parameters of this experiment, a reverse movement of a droplet is most probably due to electrostatic attraction which is only possible if this returning droplet is negatively charged. But since the potential applied on the nozzle is positive, only positive droplets thus are expected. A polarization of the liquid ligament by the strong electric field is the most plausible assumption and also justifies why the phenomenon was seen in the pulsating jet mode only, where long ligaments are created (see figure 7.3). Checking the literature we found that charging by polarization of water was already reported at the end of the 19th century by Lenard ³⁶. He was probably the first scientist to report accumulation of positive and negative charges on water droplets in nature next to water falls. Also Blanchard ³⁷ observed that bubbles bursting over the ocean release positively charged droplets. Its is important to remark that both situations do not happen in the presence of a strong electric field, just the normal field found on Earth and still both authors have related the phenomena to charge separation on air-water interfaces. More recently Maze et al. ³⁸ reported the existence of negative droplets created by positive electrosprays from purified water. However they do not elaborate on in which mode they were spraying. They have also considered that polarization would explain the existence of these negative droplets.

Figure 7.3 gives an overview of the mentioned charging mechanism. After detaching from the meniscus the liquid ligament becomes polarized causing the end nearest the nozzle to assume an opposite charge (Fig. 7.3a). Thus, the droplet(s) forming on this side may eventually carry less total charge or even opposite charge when compared to the charge of the initial ligament and the charge of the meniscus (Fig. 7.3b).

It must be taken into account that polarization requires charge carriers to create a bipolar jet prior to break-up. However, the species that are actually transported in EHDA still comprehend a topic not very well understood³⁹. Many authors have reported about these carriers, but none of the presented theories are well accepted so far. Regardless the inconsistencies normally found about this matter, some attempts to verify the nature of these charges were done. Polarization could be caused by electroconvection of H_3O^+ and OH^- under the strong electric field. As the liquid used in all experiments was deionized water these would be the possible ionic entities to consider inside the liquid. The formation of hydronium cations solvated in water is known by self-ionization of water⁴⁰ and can be enhanced in the presence of strong electric fields³⁸. One way to verify this in the time frame of the event is by checking how long the ligament persists in the electric field before it breaks-up into droplets. A stable lifetime of $\sim 90 \mu\text{s}$ was calculated from the video capture frame rate. If it is assumed that H_3O^+ and OH^- are charge carriers inside the droplet, one can conclude that, due to their high mobility⁴¹, this period is long enough to allow migration inside the ligament. This possibility would also have implications in changing the pH of the sprayed water. Experiments were done to verify water pH values before and after spraying. The pH measurements were done with WTW pH probes (340i series). The pH of the liquid was measured immediately after and immediately before the experiments. A nozzle-ring configuration was used to measure the pH after the spray, and the sprayed liquid was collected through a glass funnel into a glass bottle. Bottle and funnel were replaced each time, and each experiment was done in triplicate to confirm the results. No evidences of a pH change were found within the detection resolution of the equipment used.

Additional charge carriers could also come from electrochemical reactions inside the nozzle. Some authors have investigated the presence of metal ions in ESI

and have successfully demonstrated that they can be generated by such processes⁴², e.g. $54 \mu\text{g}\cdot\text{L}^{-1}$ of iron. As part of the experiments presented, an analysis of the sprayed liquid was done with ICP-OES (Perkin-Elmer Optima 5300 DV) to investigate the presence of metallic ions originating from the nozzle and metallic connector (see figure 7.1). This analysis did not indicate the presence of these ions in the sprayed liquid above the detection threshold of the instrument ($50\mu\text{g}\cdot\text{L}^{-1}$ for Fe and $25 \mu\text{g}\cdot\text{L}^{-1}$ for Cr and Cu, respectively).

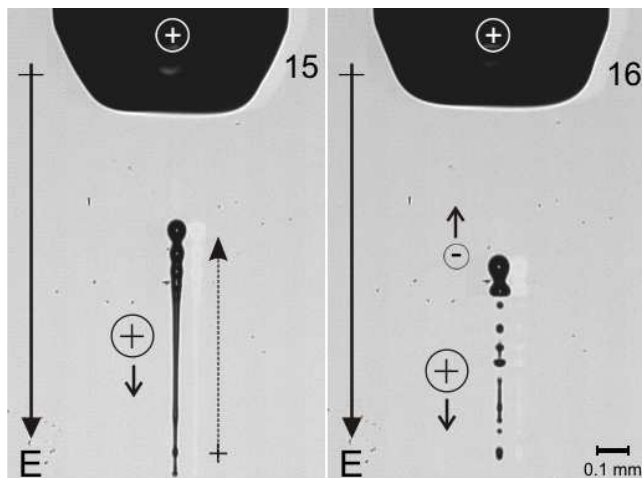


Figure 7.3a (left) and 7.3b (right) - Magnification of frames 15 and 16 of Fig. 7.2 showing the polarisation of the aqueous ligament which subsequently forms differently charged droplets.

To verify whether the phenomenon would happen with other liquids under the same conditions we also performed experiments with mixtures of deionized water and NaCl (99% Sigma Aldrich) and deionized water and ethanol (Sigma Aldrich) at different concentrations. Experiments with these liquids have also shown some droplets returning toward the liquid meniscus but much less frequent than observed with deionized water only. This could be based on the fact that deionized water has the right combination of physical properties to allow the formation of long ligaments inside the electric field. It is indeed observed that ligaments with deionized water are longer than ligaments with solutions of

deionized water and NaCl and solutions of deionized water and ethanol.

Returning to figure 7.3, it is expected that after polarization takes place the returning droplet will be charged oppositely with respect to the meniscus. Because the generation of big droplets (over $50\mu\text{m}$) in pulsating modes is rather low, the returning droplet was almost always following its path towards the meniscus without interferences of other nearby droplets. A possible interference could be created by space charge, i.e. charged droplets sprayed before the ligament is formed. However in many of the studied cases the returning droplet was formed much after the cone-jet phase of the pulsating spray, i.e. when the space charges are formed, thus this possibility was also disregarded. Later on, we will also mention that the space charges might be the reason for the fact that some droplets never came in contact with the meniscus (another studied case).

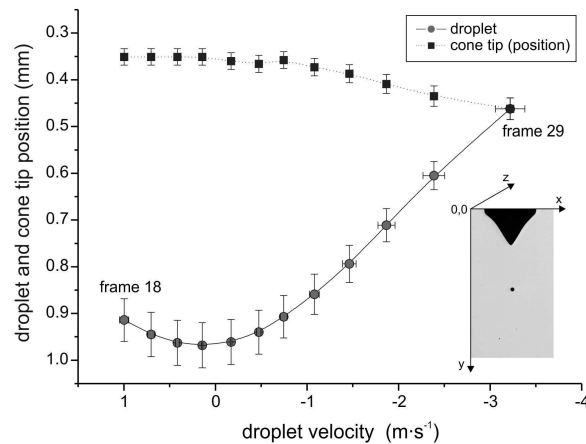


Figure 7.4 - Cone tip position, droplet axial coordinate against droplet velocity from frame 18 to 29 and coordinate system (returning droplet represented in Fig. 7.2).

The non existence of extra droplets was seen as a good possibility to try aerosol mechanics to calculate the charge of this droplet. If aerosol mechanics is to be used, droplet position, velocity and trajectory must be known. Using high speed imaging these parameters were determined quite precisely and are presented in Fig. 7.4 (returning droplet represented on Fig. 7.2). By checking the

droplet image's grey code it was possible to reduce the errors due to a possible movement perpendicular to the plane of observation (z axis). Nevertheless, a ~5% error is always expected due to the depth of field of the used lens.

3.2 Droplet charge calculation

The charge of the returning droplet was estimated from the experimentally observed trajectory using a vertical force balance. A critical parameter in this estimation was the electric field strength. The field close to the nozzle is particularly difficult to define for non-continuous ES modes due to the dynamics of the meniscus. For the present situation the model was simplified by neglecting the time variance of the electric field. After assuming a certain stable shape for the meniscus coherent with the analysed situation, the electric field strength was calculated using Comsol®.

A method combining HS imaging with a computer routine based on droplet momentum was used to calculate droplet charge. First, an image sequence of a returning droplet was chosen. To minimize the positional error caused by a possible movement of the droplet along the axis of observation, an initial routine selected droplets moving in the same plane by verifying their grey code. This also reduces the contribution from the radial component of the electric field. From the chosen set of images (Fig. 7.2) the droplet trajectory and diameter were then determined. The droplet velocity was calculated from the trajectory and the camera frame rate. To determine droplet charge another routine was used which modeled a "theoretical droplet" with the same diameter, initial position and velocity, immersed in the same electric field as applied experimentally. In order to create an upward momentum, an electric attraction between the droplet and the meniscus is assumed. Then the droplet trajectory and velocity, assuming different charges, are calculated using charge quantities from 1 μC to 1 fC. The theoretical droplet trajectory and velocity are thus compared to the real droplet values, and the closest fit chosen. In the present case, the best fits showed a deviation from the experiment of less than 5%. For these calculations the momentum conservation law applied to electrospray droplets⁴³ was used. Droplet-droplet interaction due to Coulombic effects was disregarded considering the distance of other droplets during the returning movement. The drag force was calculated

according to Hinds⁴⁴ assuming a normal atmosphere and stable conditions. Droplet's mass was assumed to be constant in the studied trajectory and deformations on droplet's surface were neglected.

3.3 Droplet charge and trajectory

The charge value adopted for a real droplet was the one which presented the best fit both for droplet axial position and droplet velocity. All selected droplets show an error smaller than 5% in relation to the fit.

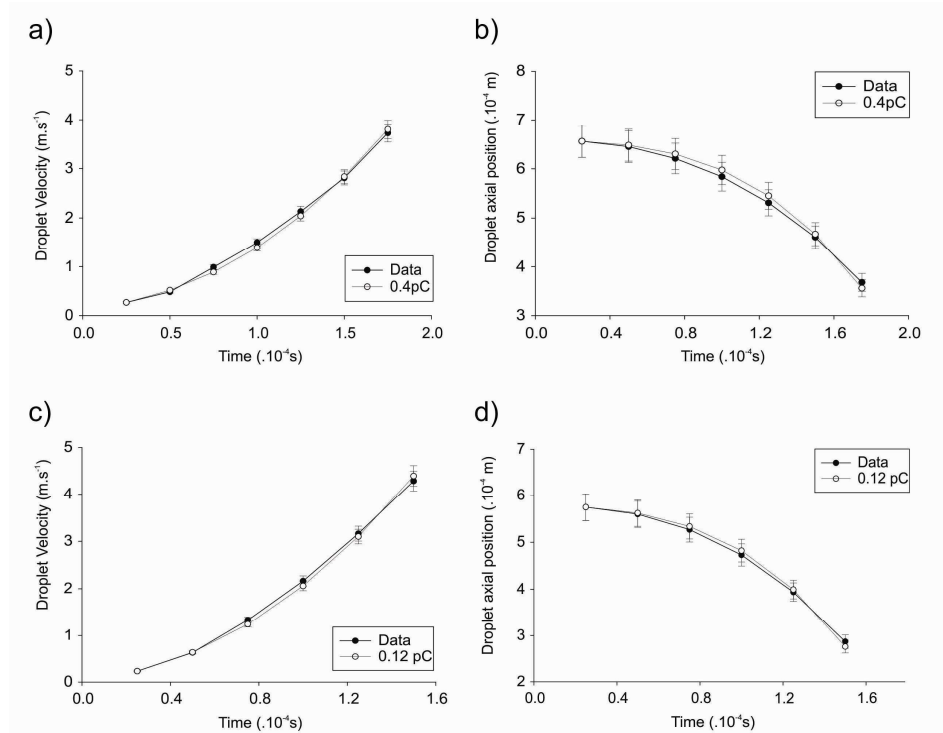


Figure 7.5(a, b, c, and d) - Droplet velocities and axial position calculated from a sequence of frames and theoretically calculated correspondences for the same sequences. Fig. 7.5a and 7.5b show the best fit found for a theoretical droplet charged with ~ 0.46 pC; Fig. 7.5c and 7.5d show the best fit found for a theoretical droplet charged with ~ 0.12 pC. The used potential for both situations was 6 kV with $1 \text{ mL}\cdot\text{h}^{-1}$ and 2 cm nozzle to plate distance.

Fig. 7.5 shows the comparison between measurement and model for axial

position and velocity of two different droplets with the adopted charge. Both cases are representative for bouncing with complete coalescence (C1). In the situation presented the resultant droplet charges were 0.12 pC and 0.46 pC, respectively.

Overall we found charges ranging between $0.32 \cdot 10^{-13}$ C ($d \sim 30 \mu\text{m}$) up to $8.0 \cdot 10^{-13}$ C ($d \sim 90 \mu\text{m}$) for the droplets as depicted in Fig. 7.6. Comparing the calculated droplet charge with the theoretical maximum charge a droplet can hold without disruption, the so-called “Rayleigh Limit”, we found charges between 2.5% and 19% of this limit.

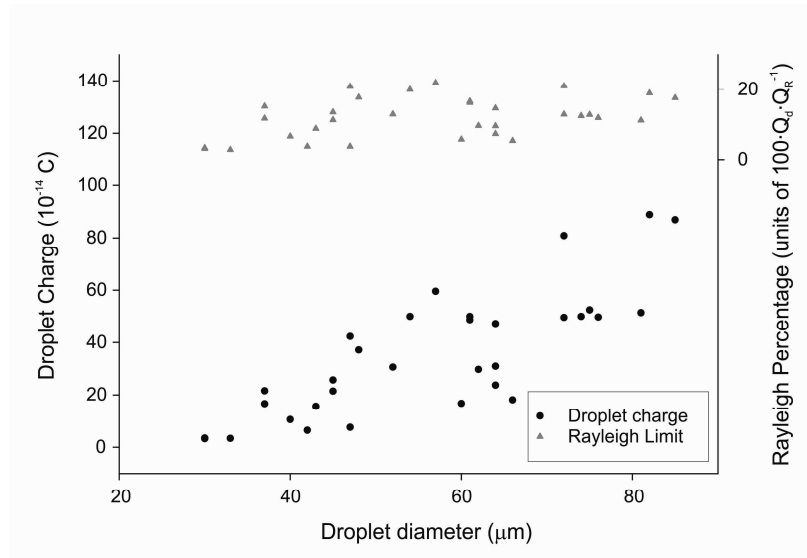


Figure 7.6 - Estimated droplet charges and respective percentage to Rayleigh Limit for different diameters.

A charge far from the Rayleigh Limit is expected for pulsating jet modes because these modes do not require relatively low potentials to be formed. There were no reported experimental values available in the literature so far according to the knowledge of the authors which would provide data to compare with the presented results.

We observed a direct correlation between droplet charge and diameter

indicating that droplets with a higher diameter would carry more charge. This is an expected trend considering that a larger surface would allow a bigger quantity of charge.

Based on the measured diameter and calculated droplet charge we observed that droplets presented small variations on their surface charge density (SCD). This can be seen in Fig. 7.7 which shows droplet SCD against diameter with an average SCD of $3.9 \cdot 10^{-5} \text{ C} \cdot \text{m}^{-2}$.

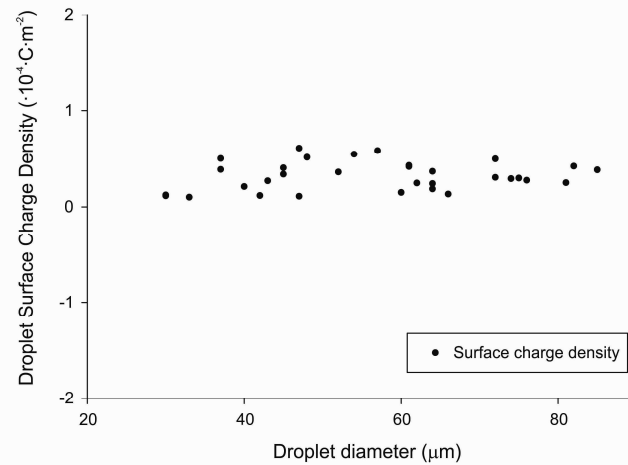


Figure 7.7 - Estimated droplet surface charge density for different diameters.

3.4 Droplet interaction with the liquid meniscus

Until now we explained a possible mechanism responsible for the return of a charged droplet against the electric field and a possible way to calculate these droplets' charge. An observed consequence of this return is contact with the liquid meniscus. In such situations the contact is normally followed by coalescence between droplet and meniscus. However, as mentioned previously, two other situations have also been observed: In the second case, droplets reversed their path after being ejected from the nozzle, touched the meniscus and were not completely reintegrated but just transferred part of their mass after the contact and returned with a smaller radius. This interaction will be, therefore, named as a

bouncing with “partial coalescence” or category C2.

The above referred interaction can be seen in Fig. 7.8. The sequence starts with the meniscus progressing from its spherical shape to a conical shape (frame 1 to 6). Some droplets from the previous cycle can be seen in the lower part of the image moving downwards. From frame 7 to frame 10 the jet starts from the meniscus tip. From frame 11 to frame 14 the jet starts to whip on its lower part and is about to detach from the meniscus in frame 15. It is also visible that from frame 8 till frame 15 small droplets are produced on the tip of the jet. The ligament break-up begins in frame 16. From frame 16 to frame 28 the uppermost droplet is formed, it moves down, stops and returns towards the meniscus. The droplet finally collides with the meniscus in frame 29, where it emits a spray of small droplets; and in frame 30 it goes back downwards with a smaller diameter.

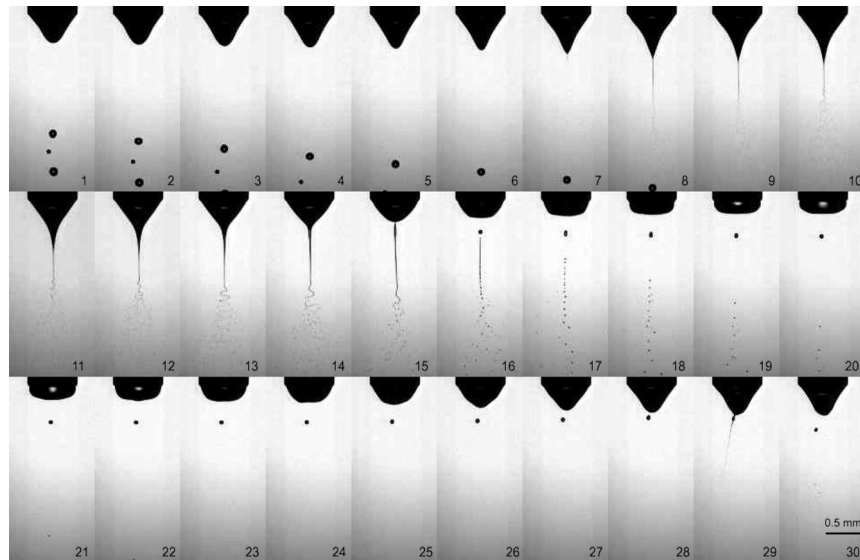


Figure 7.8 - Bouncing with “partial coalescence” or C2 – a droplet collides with the meniscus with mass exchange. The droplet diameter before collision with the meniscus is $\sim 70 \mu\text{m}$ and after is $\sim 40 \mu\text{m}$, time frame between images is $\sim 50 \mu\text{s}$, applied potential is 5.0 kV on the nozzle and the flow rate is $1 \text{ mL}\cdot\text{h}^{-1}$.

In the third case, after the break-up, droplets decelerate as they move downwards and stop. After remaining in equilibrium for some time they re-start their downward movement. In rare cases some droplets, instead of just stopping, first decelerated, then stopped, then moved slightly upwards, stopped again and finally moved downwards. But no good set of images to exemplify this last situation could be recorded. Because droplet and meniscus are not getting in direct contact in this category, it will be called “non-coalescent” bouncing or C3.

The sequence presented in Fig. 7.9 is a good example of category C3. The configuration applied was nozzle to plate, with 6 kV applied on the nozzle and a grounded plate placed 4 cm below.

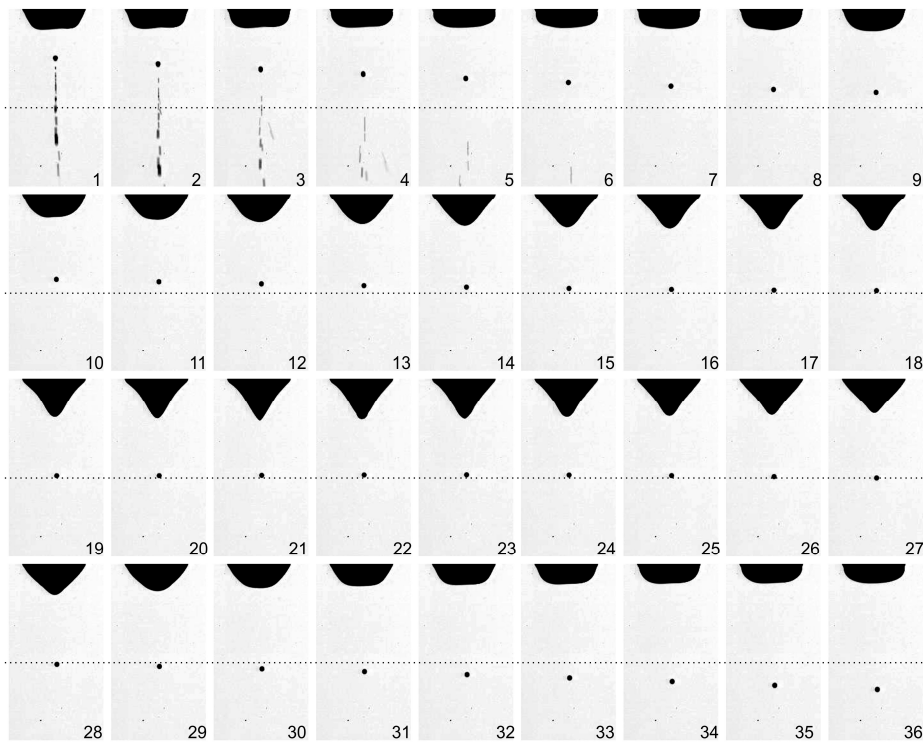


Figure 7.9 - Non-coalescent bouncing. Nozzle to plate configuration with 6 kV applied on the nozzle. Plate grounded and placed 4 cm below the nozzle. Dashed lines are arbitrarily placed to guide the eyes. Droplet’s diameter is $\sim 30 \mu\text{m}$ and the time frame between images is $40 \mu\text{s}$.

In the first frame of this sequence the jet has already broken up and the droplets are formed. From frame 2 to 6 one can see that all droplets below the uppermost one are going down following the field lines. From frame 1 to 17, the uppermost droplet is moving downwards, too. From frame 18 to 27 the droplet seems to be in “equilibrium”, its position is not changing with time. Starting with frame 27 (and continuing to frame 36) the droplet gets out from its equilibrium and moves downwards. It is also important to remark that the liquid meniscus assumes a conical shape in frame 21.

In order to better analyze this behavior, Fig. 7.10 is showing the axial coordinate of the droplet in each frame for the whole sequence. There are three different phases of the droplet’s movement. First, from frame 1 to 17, the droplet is moving downwards, from frame 18 to 27 the droplet’s axial coordinate is not changing corresponding to the “equilibrium” state mentioned before. After frame 27 the droplet continues its downward movement.

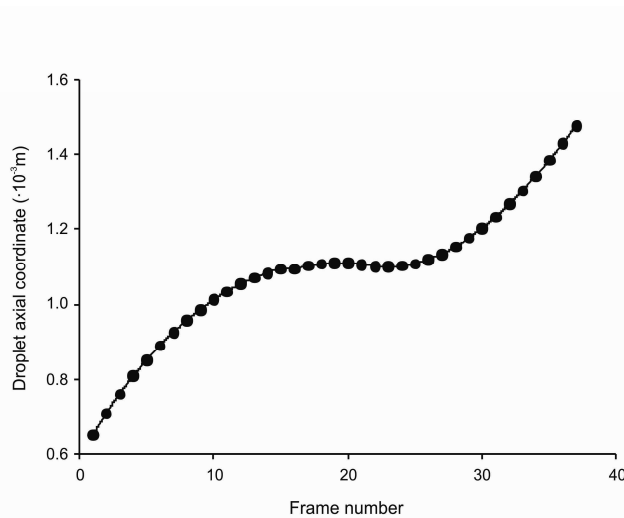


Figure 7.10 - Axial coordinate of the uppermost formed droplet represented in Fig. 7.9 against frame number. The chosen origin for the coordinate system is the same as in Fig. 7.4.

3.5 Comments on each category.

We believe that the situations described above depend on polarization and in some cases also on charge transfer between droplet and meniscus. It is possible that not only the applied electric field is an important factor to be considered in these cases, as reported by ^{26, 29, 30}, but also droplet's inertia. To better understand these different interactions we examined the stability of these droplets in the applied electric field, the coalescence phenomenon and droplet mechanics.

Concerning droplet stability it is known that from the shape assumed by the returning droplet during its movement, one can have a qualitative idea about its charge ^{26, 29, 30} before it contacts the meniscus.

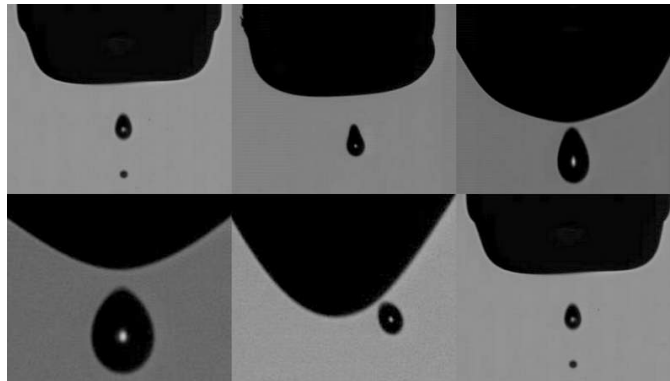


Figure 7.11 - Six examples of returning droplets assuming asymmetric tear-shapes immediately before contacting the meniscus (this is not a sequence).

Fig. 7.11 shows a close look at different droplets, from different electrospays, immediately before they touch the meniscus. The situations were all extracted from category C2 examples which allowed us to observe the variations of the droplet shape. It is easy to see that all droplets deform into an asymmetric tear-shape with the conical side pointing towards the meniscus. According to ³⁰ this implies that they are charged oppositely in relation to the meniscus and corroborates our assumption that polarization is in fact inverting droplet charge during the ligament break-up.

To verify the role of droplet inertia in different categories we analysed categories C1 and C2. Such analyses consisted in a random selection of droplets of these two categories followed by the calculation of their velocity and momentum from the break up position until the moment immediately before they collide with the meniscus, i.e. last frame with no contact. To assure the situations were consistently comparable the droplets were extracted from the same electro spray, i.e. same applied flow rate and same electric field.

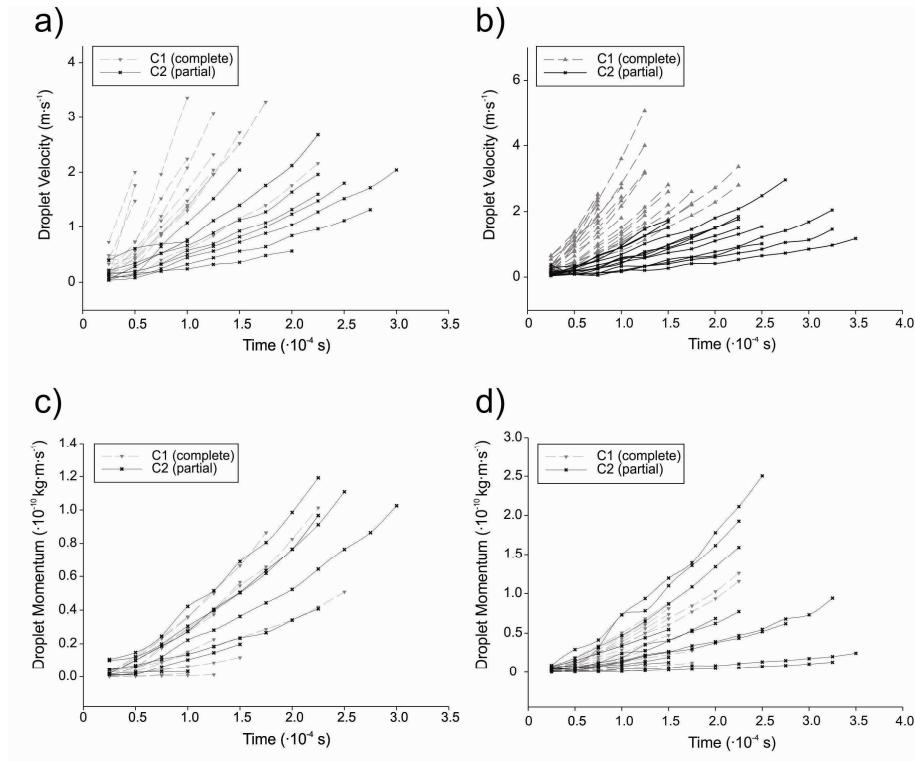


Figure 7.12 (a, b, c, d) - 7.12a and 7.12b - Droplets velocity against time in categories C1 and C2 for sprays of $0.5 \text{ mL}\cdot\text{h}^{-1}$ and $2 \text{ mL}\cdot\text{h}^{-1}$ respectively. Figures 7.12c and 7.12d, droplets momentum against time in categories C1 and C2 for the same sprays. Both sequences were recorded with 40.000 fps, which represents a time frame of $25 \mu\text{s}$ between two images. The flow and potential applied on the sprays represented in figures 7.12a and 7.12c are respectively $0.5 \text{ mL}\cdot\text{h}^{-1}$ and 6 kV and on the sprays in figures 7.12b and 7.12d are $2 \text{ mL}\cdot\text{h}^{-1}$ and 5.5 kV.

Two different electrospray configurations were chosen for each group of droplets, $0.5 \text{ mL}\cdot\text{h}^{-1}$ with 6 kV and $2 \text{ mL}\cdot\text{h}^{-1}$ with 5.5 kV applied to the nozzle. In both situations the nozzle to plate distance was 2.5 cm and the spray mode was pulsating jet mode.

Initially we studied possible differences between the variation of droplet's momentum against time for droplets in category C1 and C2. Because C1 droplets were completely reintegrated and C2 droplets just partially, we firstly verified whether complete reintegration of C1 droplets could be attributed to a higher inertia. From the plot one can see that figures 7.12a and 7.12b show droplet's velocities against time in category C1 and C2 for the two different sprays mentioned and figures 7.12c and 7.12d show droplet's momentum against time for the same droplets. By observing figures 7.12a and 7.12b one can see that C1 droplets and C2 droplets have different velocity profiles, i.e. final values of C1 droplets velocities are normally higher and they reach these values in a shorter time interval when compared to C2 droplets. If the droplets in both categories would have similar masses, their momentum would be also categorized similarly. However, when their momentum is compared there is no difference between both categories (figures 7.12c and 7.12d). This situation is plausible if droplets in category C1 are smaller than droplets in category C2. If a rather similar charge level for every droplet is assumed (see section 3.3), smaller droplets immersed in the same electric field would consequently accelerate more but their momentum would not be significantly different. The similar inertia found for the droplets in the two different categories would be explained because droplet's mass, in case C2, balances the higher values found for droplet's velocities in category C1. This assumption is supported by Fig. 7.13 which shows the calculated droplet diameters of both C1 and C2 droplets.

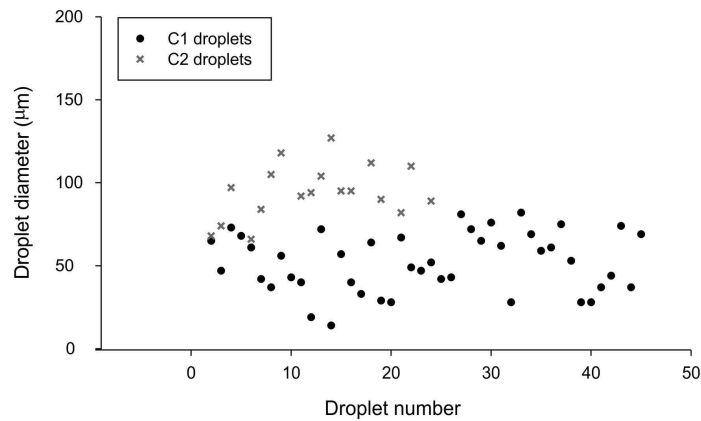


Figure 7.13 - Diameters of category C1 and C2 droplets for the sprays analysed in Fig. 7.11

The figure shows that droplets of category C1 have an average diameter of about 50 µm while droplets in category C2 have an average diameter of about 100 µm, thus droplets of category C1 are indeed smaller than droplets of category C2. A direct consequence of this observation is that droplet inertia cannot be seen as a criterion to define whether situation C1 or C2 will happen.

Contrary to that, the ligament break-up is an important factor which has to be considered because it defines both droplet size and position after polarization.

Following this line it is now important to take some considerations into account in order to explain why C1 droplets are smaller than C2 droplets. First, it can be attributed to some oscillations normally found in infusion pumps, e.g. like the one used in these experiments. Once the infused flow is not constant within a certain time frame, the jet volume will be also different with time and different droplet sizes will appear after break-up. Secondly, the break-up process of the ligament is a very random phenomenon. Many external factors, which are responsible for the necessary perturbations needed to initiate the instabilities on the ligament surface, are directly influencing this break-up, e.g. ligament length, air currents, electric field, and once we take this into account it is not reasonable to assume that all the droplets will have similar diameters in this mode.

Since inertia does not make a difference on bouncing categories, we will consider the role of the electric field. In case of deionized water, despite its high resistivity, hydraulic characteristic time can not be shorter than electric characteristic time⁴⁵. Nevertheless, we could see that droplets in category C1 were completely reintegrated, indicating that the hydraulic effect is dominating in this category. According to^{25,28}, the EF can provide bouncing of oppositely charged droplets but there is a threshold to consider in this case for the magnitude of the EF. This would imply in our case that electric field values are consistently different for C1 and C2 droplets at the moment they approach the liquid meniscus. This can be explained if we look into the intrinsic behaviour of the liquid meniscus in the pulsating jet mode. In this mode, the electric field oscillates continuously due to change of space charge density, which is visible in the changing of the meniscus shape. For pulsating jet modes this oscillation period is rather constant. A direct consequence of these oscillations is the fact that, depending on how long the droplet takes to complete its returning movement, it approaches the meniscus in a period of higher or lower electric field strength. It is straight forward that a collision with a more conical meniscus would imply that the field strength on that moment is close to its maximum value. This hypothesis can be verified from Figs 7.2 and 7.8 when, for the situation where the droplet is completely reintegrated to the meniscus (category C1, Fig. 7.2) the meniscus shape is still round and, for the partial coalescence situation (category C2, Fig. 7.8), the meniscus is more conical. Still, to test if this is true for all the other observed droplets we calculated the time interval the droplets remained in the air in each one of the mentioned categories, i.e. the droplets retention time. For C1 and C2 droplets the retention time is the time interval between the initial position after break-up to the last frame before contacting the meniscus. We also calculated the retention time for C3 droplets. In that case, since the droplet is not touching the meniscus, we define retention time as the time interval between the initial position after break-up and the position immediately after the droplet leaves its equilibrium. The droplets were extracted from sprays with three different flow rates, $0.5 \text{ mL}\cdot\text{h}^{-1}$, $1 \text{ mL}\cdot\text{h}^{-1}$ and $2 \text{ mL}\cdot\text{h}^{-1}$ in the pulsating jet mode. The droplet retention time can be used to have an idea if droplets will be exposed to high electric field intensity for a prolonged time or not. In order to have a quantitative confirmation, we compared the droplet's retention time with the half period of the oscillation of the meniscus. It's clear from Fig. 7.14

that the retention time for the C2 case is closer to the half period than the C1 case. The meaning is that C2 droplets are exposed to a higher electric field. It is important to note that the C3 case is even closer to the half period time however in this case the distance from meniscus to the droplets is much higher than in the other cases. As follows from the definitions of retention times, C3 can not be directly compared to C1 and C2.

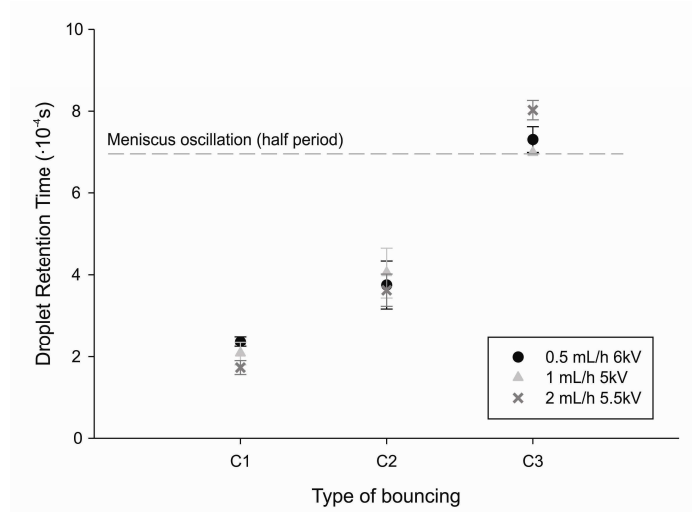


Figure 7.14 - Average retention time for droplets of category C1, C2 and C3 for three different flow rates (0.5 mL·h⁻¹, 1 mL·h⁻¹ and 2 mL·h⁻¹) compared with the average oscillation time of the liquid meniscus.

Looking now into category C3, a possible explanation for this situation would be the following: First the droplet initial velocity is caused by the ligament downwards momentum. After break-up the oppositely charged droplet starts its movement downwards and stops. The meniscus deforms into a conical shape, i.e. the EF intensity increases. As the electric field intensity increases, the electric force balances droplet gravity and the droplet reaches an equilibrium. The meniscus starts to retract indicating a reduction of the EF intensity. Electric forces also decrease and gravity moves the droplet downwards again.

It was further noticed that the reason for the downward movement is not only gravity because settling velocity of a droplet of this size is expected to be

around $2.72 \cdot 10^{-2} \text{ m}\cdot\text{s}^{-1}$ while our droplet moves with $1.2 \text{ m}\cdot\text{s}^{-1}$. This high velocity can be explained if the droplet is having its charge inverted by a short electrical discharge originating from the cone tip ⁴⁶. This suggestion is corroborated by the fact that the droplet retention time is bigger than the half oscillation period as can be seen in figure 7.14 and also by the current vs. time graph showed in figure 7.15. This graph shows a current peak at the moment that the meniscus assumes its conical shape, which indicates a possible electrical discharge.

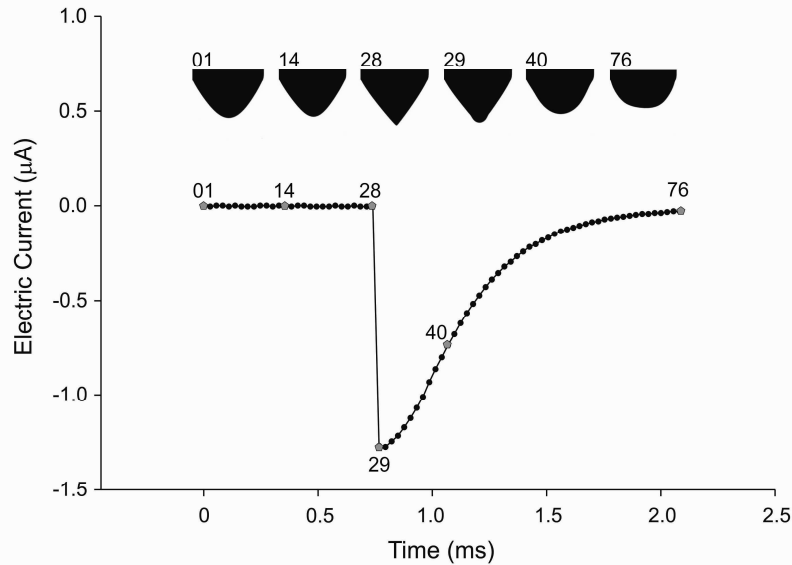


Figure 7.15 - Electric current against time synchronized with the spray movie. The spray flow was $1 \text{ mL}\cdot\text{h}^{-1}$ with -5 kV applied on the counter electrode. Time frame between two images is $27 \mu\text{s}$. The meniscus shape is represented by the images of some frames and the respective electric current signal for each frame is presented in the plot.

4. Conclusions

The presented experiments resembled classical EHDA: A DC electric field interacts with deionized water and creates an electrospray in different modes, dependent on the field strength. What was hitherto unknown, however, is that in the pulsating jet mode polarization forces can create oppositely charged droplets, thus changing repulsion into attraction, and making them return to the cone from

which they were ejected. Once there, there are different possibilities: coalescence, partial coalescence or non-coalescence. We found that the different categories depend on the retention time of the droplet in relation to the meniscus oscillation period, i.e. the changing of the electric field strength. We believe that these results can be used to better understand phenomena like the Lenard's effect ³⁶ and the build up of the electric field inside thunderstorm clouds ⁴⁷.

7. References

1. W. Gilbert, *De magnete, magneticisque corporibus, et de magno magnete tellure*. (London, 1600).
2. L. Rayleigh, Proceedings of the Royal Society of London **28**, 1878-1879 (1882).
3. L. Rayleigh, Proceedings of the Royal Society of London **29**, 71-97 (1879).
4. J. Zeleny, Physical Review **3** (2), 69 (1914).
5. J. Zeleny, Physical Review **10** (1), 1 (1917).
6. G. Taylor, Proceedings of the Royal Society of London. A. Mathematical and Physical Sciences **313** (1515), 453-475 (1969).
7. J. Marijnissen, J. of Aerosol Science **35** (Supplement 1), 3-4 (2004).
8. K. B. Geerse, J. C. M. Marijnissen, A. Kerssies, M. van der Staaij and B. Scarlett, Journal of Aerosol Science **30** (Supplement 1), S553-S554 (1999).
9. L. Gradon and J. Marijnissen, *Optimization of Aerosol Drug Delivery*. (Kluwer academic publishers, Dordrecht, 2003).
10. C. U. Yurteri, J. C. M. Marijnissen and R. P. A. Hartman, KONA Powder and Particle Journal **28**, 24 (2010).
11. A. G. Bailey, *Electrostatic Spraying of Liquids*. (Jonh Wiley & Sons, 1988).
12. J. M. Grace and J. C. M. Marijnissen, Journal of Aerosol Science **25** (6), 1005-1019 (1994).
13. J. Eggers and E. Villermaux, Reports on Progress in Physics **71** (3), 036601 (2008).
14. I. Marginean, L. Parvin, L. Heffernan and A. Vertes, Analytical Chemistry **76** (14), 4202-4207 (2004).
15. M. Cloupeau and B. Prunet-Foch, Journal of Aerosol Science **25** (6), 1021-1036 (1994).
16. I. Marginean, P. Nemes and A. Vertes, Phys. Rev. E **76** (2), 026320 (2007).
17. R. S. Carson and C. D. Hendricks, AIAA Journal **3** (6) (1964).
18. R. Juraschek and F. W. Röllgen, International Journal of Mass Spectrometry **177** (1), 1-15 (1998).
19. E. C. Fuchs, Journal of Physics D: Applied Physics **40** (19), 6112 (2007).
20. E. C. Fuchs, L. L. F. Agostinho, M. Eisenhut and J. Woisetschlager, Proc. SPIE **7376** (2010) 73761E1-15.
21. W. Armstrong, the Newcastle Literary and Philosophical Society, The Electrical Engineer, 145-154 (1893).
22. H. T. Ochs and R. R. Czys, Nature **327** (6123), 606-608 (1987).
23. P. Atten, Journal of Electrostatics **30**, 259-269 (1993).

24. R. S. Allan and S. G. Mason, *Journal of Colloid Science* **17** (1962).
25. J. C. Bird, W. D. Ristenpart, A. Belmonte and H. A. Stone, *Physical Review Letters* **103** (16), 164502 (2009).
26. R. S. Allan and S. G. Mason, *Journal of Colloid and Interface Science*, **12** (1961).
27. J. P. Borra, D. Camelot, K. L. Chou, P. J. Kooyman, J. C. M. Marijnissen and B. Scarlett, *Journal of Aerosol Science* **30** (7), 945-958 (1999).
28. W. D. Ristenpart, J. C. Bird, A. Belmonte, F. Dollar and H. A. Stone, *Nature* **461** (7262), 377-380 (2009).
29. P. R. Brazier-Smith, *Physics of Fluids* **14** (1), 1-6 (1971).
30. R. L. Grimm and J. L. Beauchamp, *The Journal of Physical Chemistry B* **109** (16), 8244-8250 (2005).
31. M. A. Fontelos, U. Kindelan and O. Vantzios, *Physics of Fluids* **20** (9), 092110 (2008).
32. R. P. A. Hartman, D. J. Brunner, D. M. A. Camelot, J. C. M. Marijnissen and B. Scarlett, *Journal of Aerosol Science* **30** (7), 823-849 (1999).
33. R. P. A. Hartman, D. J. Brunner, D. M. A. Camelot, J. C. M. Marijnissen and B. Scarlett, *Journal of Aerosol Science* **31** (1), 65-95 (2000).
34. R. P. A. Hartman, D. J. Brunner, J. C. M. Marijnissen and B. Scarlett, *Journal of Aerosol Science* **29** (Supplement 2), S977-S978 (1998).
35. R. P. A. Hartman, J. C. M. Marijnissen and B. Scarlett, *Journal of Aerosol Science* **28** (Supplement 1), S527-S528 (1997).
36. P. Lenard, *Ann. Physik*, 149-198 (1902).
37. D. C. Blanchard, *American Meteorological Society* **15**, 383-396 (1958).
38. J. T. Maze, T. C. Jones and M. F. Jarrold, *The Journal of Physical Chemistry A* **110** (46), 12607-12612 (2006).
39. A. M. Ganan-Calvo and J. M. Montanero, *Phys. Rev. E* **79** (6) (2009).
40. A. A. Zavitsas, *The Journal of Physical Chemistry B* **105** (32), 7805-7817 (2001).
41. R. Hartman, Delft University of Technology, 1998.
42. A. T. Blades, M. G. Ikonomidou and P. Kebarle, *Analytical Chemistry* **63** (19), 2109-2114 (1991).
43. K. B. Geerse, Delft University of Technology, 2003.
44. W. C. Hinds, *Aerosol Technology*, 2 ed. (Wiley Interscience, 1998).
45. U. Stachewicz, J. F. Dijkstra, D. Burdinski, C. U. Yurteri and J. C. M. Marijnissen, *Langmuir* **25** (4), 2540-2549 (2009).
46. R. A. Roos, (Nocé, France, 2011).
47. C. Saunders, *Space Sci Rev* **137**, 335-353 (2008).

Appendix 7A

Calculation of a single droplet charge

To calculate the electric charge of a single isolated droplet returning to the liquid meniscus and sprayed in the intermittent cone-jet mode (as described in chapter 7) the following routine was developed. Initially, an image sequence with N images of a certain droplet was chosen. From this set of images the droplet's positions, i.e. position of its centroid, and diameter, i.e. droplet's Ferrets diameter, were determined. The direction and origin of the coordinate axis were chosen as demonstrated in figure 7A.1.

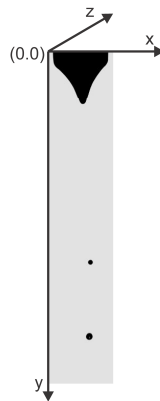


Figure 7A.1 - Axis direction and origin.

Droplets moving in the direction of the z axis were excluded based on modifications on their grey code to minimize positional errors. After defining droplet's positions its velocity was calculated according to

$$v = \frac{ds}{dt} \quad (7.1)$$

Where ds is the space traveled by the droplet between two consecutive positions and dt is the elapsed time between these positions calculated using the camera frame rate.

Another routine was then used to model a “theoretical droplet” with the following boundary conditions:

$$\begin{cases} D_i = D_d \\ s_{0i}(x, y) = s_0(x, y) \\ v_{0i}(x, y) = v_0(x, y) \end{cases}$$

Where D_i is the diameter of theoretical droplet, D_d is the Ferret diameter of the real droplet. S_{0i} and S_0 are the initial positions of the theoretical droplet and the real droplet respectively and v_{0i} and v_0 are the initial velocities of the theoretical droplet and the real droplet respectively.

After defining these values the routine attributed a certain value for the theoretical droplet charge (initially 1fC as previous calculations pointed for values in the order of 1pC) and a force balance was applied to calculate the resultant force acting on it using momentum conservation law applied to electrospray particles¹. For that the following forces were considered:

The electrostatic field force

The electrostatic field force is the interaction between the electric field and the charge on the droplet q_i given by

$$\vec{F}_i^E = q_i \cdot \vec{E} \quad (7.2)$$

The electric field strength was modeled with Comsol Multiphysics[®]. As a result its strength is known at every position within the setup so the force on the droplet could be obtained for every position. The volume element of the field model was selected by defining a grid 2 times smaller than the smallest distance between two consecutive points measured for all the selected droplets. The electric field strength at a certain position is obtained by performing a grid-point search followed by interpolation of the volume elements closest to the position to

be found.

The Coulomb interaction force

The Coulomb interaction force can be defined as the result of influencing electric fields of individual droplets and it is defined as:

$$\vec{F}_i^{i,j} = q_i \cdot \sum_{\substack{j=1 \\ j \neq i}}^N \frac{q_j \cdot \vec{r}_{ij}}{4\pi\epsilon_0 \cdot r_{ij}^3} \quad (7.3)$$

Where ϵ_0 is the permittivity of free space (similar to air), r_{ij} is the distance between two droplets and N is the total number of droplets.

The Drag force

The drag force is defined as the friction between the surrounding air and the droplet and is described as follows:

$$\vec{F}_i^D = C_D \cdot \frac{\pi}{8} \cdot \rho_{air} \cdot D_i^2 \cdot (\vec{v}_{air} - \vec{v}_i) \cdot |\vec{v}_{air} - \vec{v}_i| \quad (7.4)$$

Where C_D is the drag coefficient, ρ_{air} is the air density, \vec{v}_{air} is the air velocity and \vec{v}_i is the droplet velocity. C_D is defined according to the regime the particle is moving in. This regime is defined by the particle's Reynolds number calculated as:

$$Re = \frac{\rho_{air} |\vec{v}_{air} - \vec{v}_i| \cdot D_i}{\eta_{air}} \quad (7.5)$$

In the laminar Stokes regime ($Re \leq 1$) the drag coefficient is calculated as:

$$C_D = \frac{24}{Re} \quad (7.6)$$

For Reynolds numbers bigger than 1 this coefficient is different. For cases where $1 > \text{Re} > 1000$ the following correction can be applied ²:

$$C_D = \frac{24}{\text{Re}} \cdot (1 + 0.15 \cdot \text{Re}^{0.687}) \quad (7.7)$$

The droplets considered here were starting their movement inside the Stokes regime and some of them, in the last part of their trajectory only, reached $\text{Re} > 1$. Therefore we considered the droplets moving in the Stokes region.

The gravitational force

The gravitational force is the product between the particle mass by the gravitational constant \vec{g} . It was calculated as:

$$\vec{F}_i^G = \frac{\pi \cdot \rho_l \cdot D_i^3}{6} \cdot \vec{g} \quad (7.8)$$

Where ρ_l is the liquid density. The resulting force was then calculated for the theoretical droplets assuming the previously mentioned initial conditions and a movement in each studied direction (x and y) using Newton's law of motion as:

$$\vec{F}_{Ri} = \frac{d(m_i \vec{v}_i)}{dt} = q_i \cdot \vec{E} + q_i \cdot \sum_{\substack{j=1 \\ j \neq i}}^N \frac{q_j \cdot \vec{r}_{ij}}{4\pi\epsilon_0 \cdot r_{ij}^3} + C_D \cdot \frac{\pi}{8} \cdot \rho_{air} \cdot D_{id}^2 \cdot (\vec{v}_{air} - \vec{v}_i) \cdot |\vec{v}_{air} - \vec{v}_i| + \frac{\pi \cdot \rho_l \cdot D_{id}^3}{6} \cdot \vec{g} \quad (7.9)$$

The following assumptions were taken:

- Droplet-droplet interaction due to Coulomb effects was disregarded because we worked with isolated droplets.
- Data indicated small variation of the droplet diameter within the studied intervals (no evaporation).
- Droplets were considered spherical (no surface deformations).
- The charge on the droplet surface is constant.
- Liquid properties are constant.
- The ambient air has constant properties and is stagnant, $v_{air} = 0$.

As the theoretical droplet was assumed to be moving in the Stokes region we calculated its terminal velocity as:

$$V_{f_i} = \frac{F_{R_i}}{3\pi\eta D_i} \quad (7.10)$$

And its relaxation time as:

$$\tau_i = \pi D_i^3 \rho_l \frac{V_f}{6F_{R_i}} \quad (7.11)$$

Assuming straight line acceleration and a constant external force for the studied interval the theoretical droplet's velocity at each subsequent point was calculated as:

$$V_j = V_f - (V_f - V_0) \cdot e^{-\frac{t}{\tau}} \quad (7.18)$$

Where t is the time interval between two points. Finally its position at each subsequent point was calculated as:

$$s_j = s_{j-1} + (V_f \cdot t + (V_f - V_0) \cdot \tau \cdot (1 - e^{-\frac{t}{\tau}})) \quad (7.19)$$

The routine was repeated N-1 times in order to define the theoretical droplet's velocity and position for all points after its assumed initial position and velocity. After that a new charge was attributed and the sequence was repeated. The charge values were attributed in steps from 1fC until 1μC.

The theoretical droplet's trajectory and velocity were then compared to the real droplet and the droplet charge was selected as the charge which presented the best fit. The calculated values showed good agreement within a 5% error.

The effects of gravity were also checked by excluding the last term of equation 7.14 from the calculations and recalculating the droplet charge for these conditions. The modification did not cause big differences on the calculated charge of the droplet.

References

1. K. B. Geerse, Delft University of Technology, 2003.
2. W. C. Hinds, *Aerosol Technology*, 2 ed. (Wiley Interscience, 1999).

Chapter 8

General conclusions and outlook



Picture by Luewton L. F. Agostinho and Siebren Brouwer

Electrohydrodynamic atomization (EHDA), also known as electrospraying, is a technique which uses (primarily) an electric field to atomize a liquid. With this technique it is possible to produce monodisperse charged droplets in the micro and nanometer range. The monodispersity and the charge offer a variety of possibilities in which EHDA can be used.

In this technique different combinations of potential and flow rate produce different *modes*, e.g. the cone-jet mode, the intermittent cone-jet mode and the simple-jet mode.

Most of the scientific efforts invested on studying EHDA have been focused on the cone-jet mode. The reason for that is the capacity of this mode on producing droplets which are much smaller than the nozzle diameter and highly charged, i.e. approximately 70% of their Rayleigh limit. Among many other applications, the cone-jet mode is used in electrospray ionization for mass spectroscopy devices, to synthesize nanostructures and for the application of pesticides.

In this thesis we investigated the characteristics and possible applications of another mode, the simple-jet mode. The simple-jet mode is known as the mode which operates at the highest flow rate in electrohydrodynamic atomization. If this specific parameter is pushed to its limit, the benefits of using an electric field to atomize the liquid become questionable. On the other hand, if it can be used, one of the main drawbacks of operating in the cone-jet mode will be overcome, i.e. the low throughputs.

Atomization methods which can produce high throughputs and monodispersed (sub)millimeter droplets are necessary in many processes, e.g. spray drying and thermal desalination. In our work, the application of the simple-jet mode was focused on thermal desalination.

The current challenges faced on providing drinking water with enough quality and quantity in this world is briefly presented in chapter 1. In this same chapter desalination is presented as one of the most promising solutions to overcome these challenges and some current techniques are discussed.

In chapter 2 electrohydrodynamic atomization is generally presented and the simple-jet mode is introduced.

The investigations about the simple-jet mode start in chapter 3. In this chapter its intrinsic characteristics were analyzed for inviscid liquids. There it is possible to see that the influence of the electric field in this mode is still noticeable but highly depended on the flow rate and on the sparking limits of the chosen configuration. An important characteristic is the much larger electric potential and flow rate window, when compared to the cone-jet mode, within which the mode can happen. From the diagram shown in figure 3.7, it is possible to define theoretically the maximum flow rate at which the influences created by the application of an electric potential on the dispersion of the droplets practically disappear. Additionally, the droplets charge, dispersion and limits for off-axis instabilities (whipping breakup) are presented.

The relation between applied potential and droplet diameter is further explored in chapter 4. There it was concluded that the application of the electric potential could reduce the droplets average diameter up to 40%. Additionally monodisperse sprays with relative standard deviation (RSD) < 0.20 could be created.

A stable and efficient design for out-scaling is proposed in chapter 5. The combination of the high flow rates in the simple-jet mode with a multinozzle configuration allowed atomization with relatively high throughputs. The system was also designed to operate inside very humid chambers; therefore it can be used for evaporation.

Chapter 6 is an investigation about the application of the device in a single-effect evaporator. The stability of the multinozzle regarding the presence of electric current peaks and sparking was evaluated. With this system it was shown that electrohydrodynamic atomization in the simple jet mode can enhance evaporation levels up to 40%. For the atomization step the energy efficiency prove to be 2 times lower than for swirl atomizers.

Chapter 7 is an investigation about a phenomenon observed during the experimental work with another mode, the intermittent cone-jet mode. The use of high speed imaging during electro spraying in the intermittent cone-jet mode

allowed us to visualize some droplets which, after sprayed, were returning to collide with the charged meniscus. This returning behavior was unexpected regarding the fact that such droplet should be charged with the same charge as the meniscus, therefore should be repelled by it. Investigations have pointed out a possible polarization during the breakup process which explained the presence of negative droplets in positive electrosprays.

Exploring the EHDA simple-jet mode has been proven interesting. The challenges we have been facing to produce water to a thirsty planet are enough to justify the efforts invested on bringing new and reliable technologies to the market.

Appendix 8

Nozzles

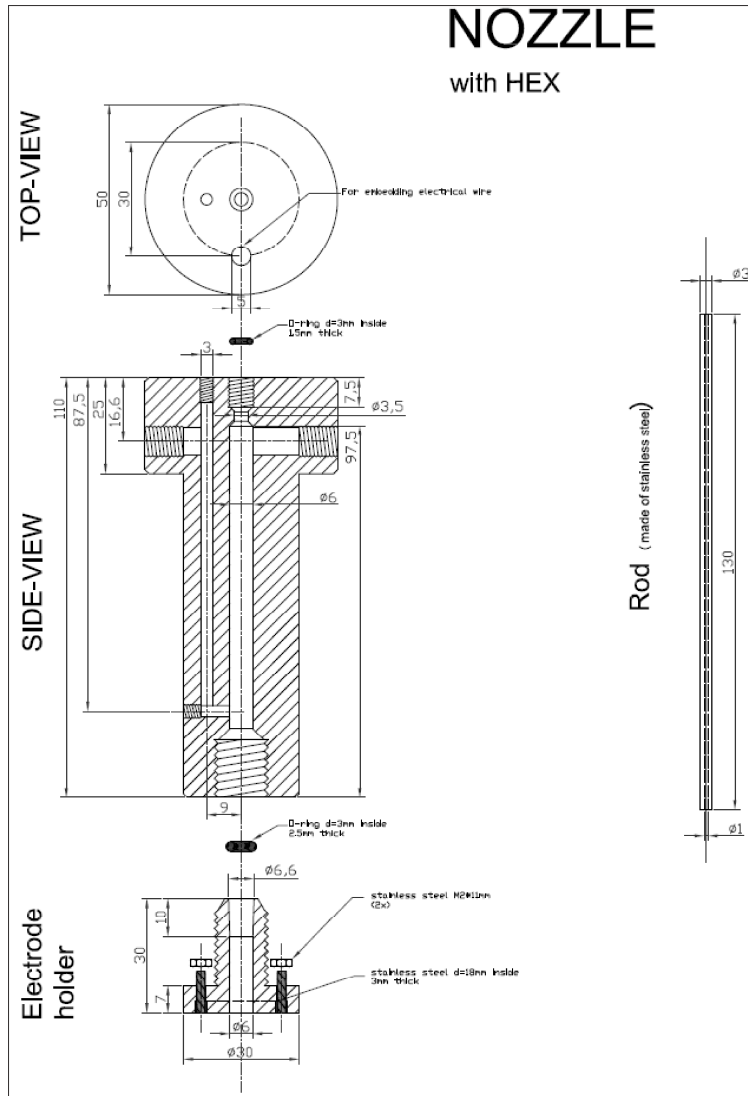


Figure 8A.1 - Nozzle with heat exchange for evaporation experiments.

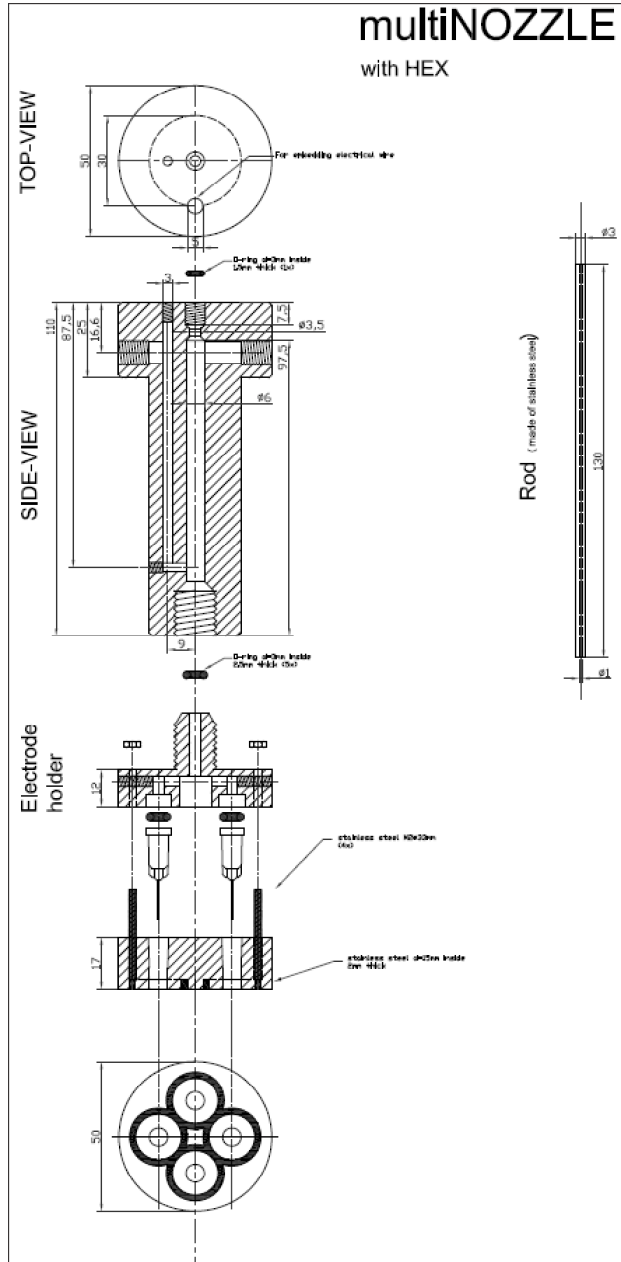


Figure 8A.2 - Multinozzle design with internal heat exchange.

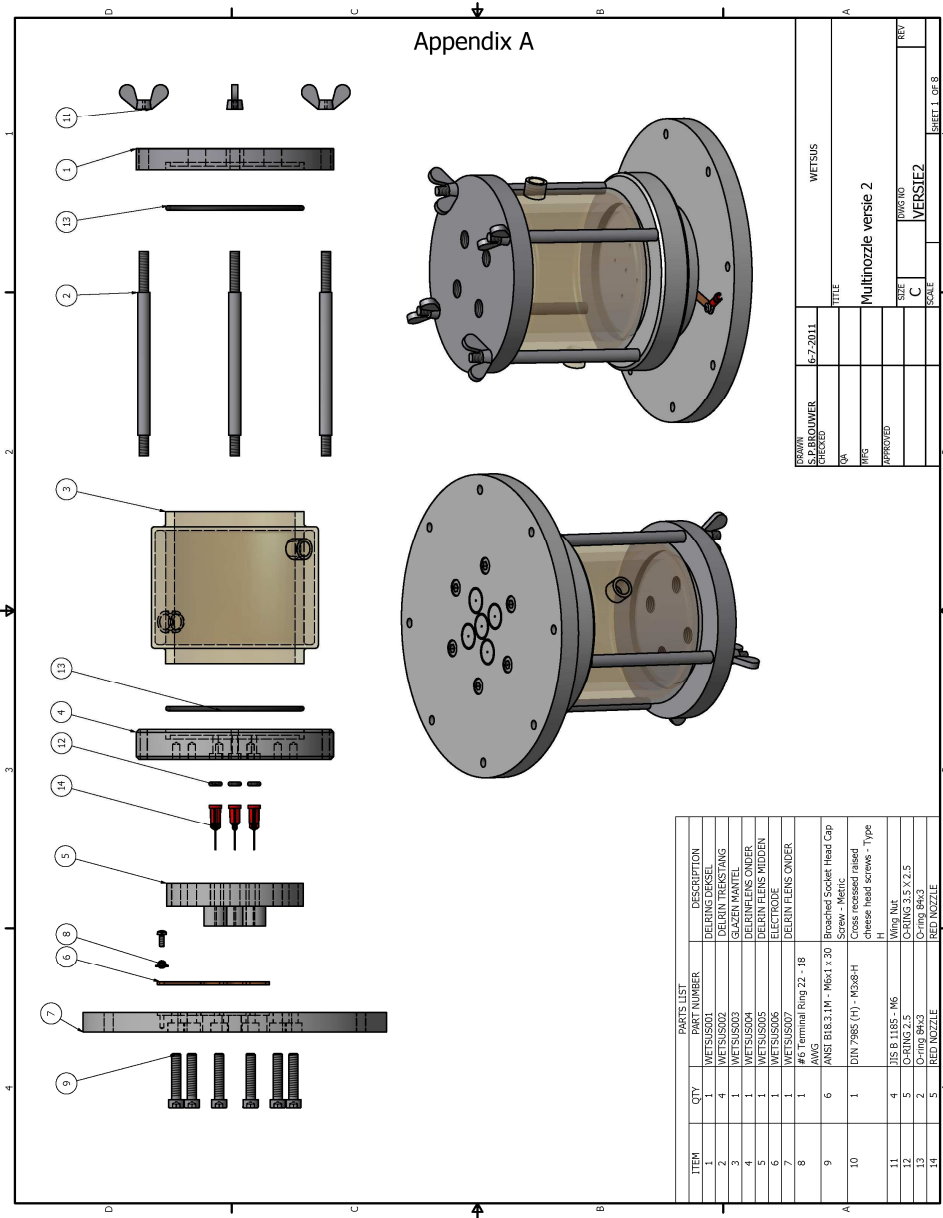


Figure 8A.3 – Multinozzle with heat exchange and insulation layer.



Figure 8A.4 – Electro spray inventory.

Acknowledgments

This thesis could not have been written without the contribution of other people.

I would first like to express my gratitude to my family and especially to my wife Silvia Leticia Abreu Agostinho. Without her love and support I could never overcome the challenges I faced during my doctoral education years. I would also like to thank my son, Caio Newton Abreu Agostinho for helping me with some illustrations used inside the thesis. And again to him and to Luiz Arthur Abreu Agostinho for being together the reason I want to become a better man everyday.

I also would like to thank my parents José Newton Agostinho and Luena Lemos Felício Agostinho and my brothers Cícero Newton Lemos Felício Agostinho, Luane Lemos Felício Agostinho, Newlena Lemos Felício Agostinho and Fabiano Lemos Felício for their support, examples and encouragements.

I owe my deepest gratitude to Dr. Jan Marijnissen and Dr. Caner Yurteri whose support and encouragement enabled me to develop a deep understanding of electrohydrodynamic atomization and many other subjects.

The same gratitude I would like to express to Dr. Elmar Christof Fuchs for being a supervisor, confident, mentor and a good friend.

Thank you to Mr. Gerrit Oudakker, without your enthusiasm and beliefs in the possibilities of electrospray desalination, this thesis would not have been written now.

I thank my promoter Prof. dr. ir. M.C.M. van Loosdrecht for his contributions and kind support.

I also would like to thank the Wetsus High Voltage team for the nice discussions, contributions and good evenings with some kilovolts of enthusiasm.

I also would like to thank my students Liandro Camelia, Francois Chague, Jouke Wartena, Siebren Brouwer, Peter de Baker and Anne Kamau for their contributions, hard work and nice inputs.

It is a pleasure to thank all my friends and colleagues from my group at Wetsus, especially to: Paula van den Brink, Maxime Remy, Claudia Dresser, Nadine Boelee, Philipp Kuntke, Martijn Wagterveld, Kamuran Yasadi, Astrid Paulitsch-Fuchs, Adam Wexler, Lucia Hernandez, Johannes Kuipers and Claudia Sousa for all the fun, nice dinners, concerts, sushi nights, conferences and for being present in different ways of our lives for the last 5 years.

A very special thank you to my paranymphs Bruno Bastos Sales and Kirsten Steinbusch for all the support and hard work helping me with the final steps of my defense.

A thank you to Prof. Dr. Jakob Woisetschlaeger for all the help with the images and optical measurements.

I cannot forget the Wetsus Technical team for all the analysis, help with the construction of many different parts and great support. A special thank you to Jan Tuisntra, Harm van der Kooi, Wim Borgonie and Jelmer Dijkstra.

It is also a pleasure to thank my friends and colleagues from TU Delft, Mario Valvo, Yongsuang Arnantigo, Urszula Stachewicz and Shaak Verdoold for all the help and for the pleasant time during the Aerosol Conferences.

For keeping me sober after some very stressful weeks and for the nice company I would like to express all my gratitude to my Brazilian/Dutch families; Milano de Valk, Glas-Bastos Sales, Carneiro, van Wieren, Ventura, etc.

Lastly I would like to apologize to all of those who were not mentioned here but certainly contributed for the accomplishment of my goals.

Curriculum Vitae

Luewton Lemos Felício Agostinho

July 31st, 1974	Born in São Luis, Maranhão, Brazil
1977 - 1993	Primary, Secondary and High school. Colégio Santa Teresa, São Luis, Maranhão, Brazil.
1993 - 1994	Physics – Universidade Federal do Ceará, Fortaleza, Brazil
2000 - 2005	Bachelor degree, Civil Engineering. Universidade Federal do Ceará. Fortaleza, Ceará, Brazil.
2005 - 2007	Master in Civil Engineering. Universidade Federal do Ceará. Fortaleza, Ceará, Brazil.
2008 - 2013	PhD Research. Delft University of Technology. Delft, The Netherlands.
2012 - 2013	Researcher at Wetsus Centre of Excellence for Sustainable Water Technology. Leeuwarden, The Netherlands.

List of Publications and Prize

Journal Publications

- **Agostinho, L.L.F.**, C.U. Yurteri, J.C.M. Marijnissen, S. Brouwer, and G. Taminga, *Morphology of Water Electrospays in the simple-jet mode*. Physics Review E, **86**, 066317 (2012).
- **Agostinho, L.L.F.**, C.U. Yurteri, E. C. Fuchs, and J.C.M. Marijnissen, *Monodisperse Water Microdroplets Generated by Electrohydrodynamic Atomization in the Simple-Jet mode*. Applied Physics Letters, 2012. **100**(24): p. 4.
- **Agostinho, L.L.F.**, S. Brouwer, C.U. Yurteri, E.C. Fuchs, and J.C.M. Marijnissen, *Insulated multinozzle system for electrohydrodynamic atomization in the simple-jet mode*. Submitted to Applied Physics Letters, 2012.
- **Agostinho, L.L.F.**, A. Kamau, S. Brouwer, C.U. Yurteri, E.C. Fuchs, and J.C.M. Marijnissen, Application of a multinozzle electrohydrodynamic atomizer to enhance evaporation in a single-effect evaporator. *Submitted to Desalination, 2012*.
- **Agostinho, L.L.F.**, E.C. Fuchs, S.J. Metz, C.U. Yurteri, and J.C.M. Marijnissen, *Reverse movement and coalescence of water microdroplets in electrohydrodynamic atomization*. Physical Review E, 2011. **84**(2): p. 026317.
- E.C. Fuchs, **L.L.F. Agostinho**, A. Wexler, R.M. Wagterveld, J. Tuinstra, J. Woisetschläger, The behavior of a floating water bridge under reduced gravity conditions, J. Phys. D: Appl. Phys **44** (2011) 025501 (8pp).
- E.C. Fuchs, **L.L.F. Agostinho**, M. Eisenhut, J. Woisetschläger, Mass and charge transfer within a floating water bridge, Proc. SPIE **7376** (2010) 73761E1-15
- E.C. Fuchs, A.D. Wexler, **L.L.F. Agostinho**, M. Ramek, J. Woisetschläger, *Methanol, Ethanol and Propanol in EHD liquid bridging*, J. Phys. Conf. Ser. **329** (2011) 012003
- E.C. Fuchs, **L.L.F. Agostinho**, A. D. Wexler, J. Woisetschläger. Investigation of the mid-infrared emission of a floating water bridge. J. Phys. D: Appl. Phys.
- S. Verdoold, **Agostinho, L.L.F.**, C.U. Yurteri, and J.C.M. Marijnissen, *A generic electro spray classification*. To be submitted to Journal of Aerosol Science.

International Conferences – Oral and poster presentations

- European Aerosol Conference, Karlsruhe, Germany, 2009 (oral presentation). [Agostinho, L.L.F., C.U. Yurteri, E. C. Fuchs, and J.C.M. Marijnissen], *“Phenomenology of Salt Water Electrosprays*
- European Aerosol Conference, Karlsruhe, Germany, 2009 (poster presentation). [Agostinho, L.L.F., C.U. Yurteri, E. C. Fuchs, and J.C.M. Marijnissen], *“Droplet Bouncing Effect in Electrohydrodynamic Atomization”*.
- Wetsus Conference, Leeuwarden, The Netherlands, 2009. [Agostinho, L.L.F., C.U. Yurteri, E. C. Fuchs, and J.C.M. Marijnissen]. *“Electrohydrodynamic Thermal Desalination”*
- International Aerosol Conference, Helsinki, Finland, 2010 (oral presentation). [Agostinho, L.L.F., C.U. Yurteri, E. C. Fuchs, and J.C.M. Marijnissen], *“Determination of a single droplet charge using high speed imaging in electrohydrodynamic atomization”*
- Fifth Annual Conference on the Physics, Chemistry and Biology of Water. 2010, Vermont, USA (poster presentation). [Agostinho, L.L.F., C.U. Yurteri, E. C. Fuchs, and J.C.M. Marijnissen]. *“Total and partial coalescence of bouncing water droplets in electrohydrodynamic atomization”*.
- European Aerosol Conference, Manchester, UK, 2011 (oral presentation). [Agostinho, L.L.F., C.U. Yurteri, E. C. Fuchs, and J.C.M. Marijnissen], *“Characterization of EHDA in the simple-jet mode (water)”*

Prize

- Gilbert Ling Poster Award (best poster) at the Fifth Annual Conference on the Physics, Chemistry and Biology of Water. 2010, Vermont, USA (poster presentation). [Agostinho, L.L.F., C.U. Yurteri, E. C. Fuchs, and J.C.M. Marijnissen]. *“Total and partial coalescence of bouncing water droplets in electrohydrodynamic atomization”*.